# Spatial Characterization and Estimation of Intracardiac Propagation Patterns During Atrial Fibrillation

Richter, Ulrike

2010

# Spatial Characterization and Estimation of Intracardiac Propagation Patterns During Atrial Fibrillation

Ulrike Richter

Lund 2010

Department of Electrical and Information Technology
Lund University
Box 118, SE-221 00 LUND
SWEDEN

This thesis is set in Computer Modern 10pt
with the LaTeX Documentation System

Series of licentiate and doctoral theses
No. 27
ISSN 1654-790X


Printed in Sweden by *Tryckeriet i E-huset*, Lund.
November 2010.

*In Gedenken an meine liebe Oma, Ruth Hoffmann.*

# Sammanfattning

Syftet med den aktuella forskningen är att ge en bättre förståelse av förmaksflimmer, den vanligaste rytmrubbningen i hjärtat som drabbar så många som var tionde över 70 år. Mekanismerna för förmaksflimmer är långt ifrån kartlagda, vilket bland annat leder till att behandlingen är standardiserad istället för att den beror på de mekanismer som styr varje enskild patients arytmi. Under lång tid har förmakens elektriska aktivitet betraktats som kaotisk, och först på senare tid har forskning kunnat visa att det går att urskilja vissa utbredningsmönster. I denna avhandling har flera nya metoder för att analysera utbredningen av den elektriska aktiviteten i hjärtat under förmaksflimmer tagits fram, vilka i framtiden kan möjliggöra mer effektiv behandling. Utöver dessa metoder, som kräver signaler registrerade inifrån hjärtat, har även en metod utvecklats för att analysera förmaksflimmer utifrån signaler registrerade på kroppsytan. Denna metod kan komma till användning vid diagnostik såväl som vid val av behandlingsform.

Förekomsten av förmaksflimmer skattas till 1–2 % av befolkningen, vilket motsvarar mer än 100 000 personer i Sverige. Förmaksflimmer leder till att hjärtats förmak slår snabbt och okontrollerat, vilket kan upplevas som en fladdrande känsla i bröstet och medför besvär som försämrar livskvalitén för den drabbade. Det är dock viktigt att framhålla att även om förmaksflimmer är en sjukdom som förknippas med högre risk för stroke, så kan de drabbade i stor utsträckning fortsätta leva som vanligt långt efter diagnosen. Beroende på andra sjukdomstillstånd i eller med påverkan på hjärtat utvecklas förmaksflimmer under olika lång tid från relativt korta attacker, som går över av sig själv, via längre attacker som inte längre bryts av sig själv, till ihållande förmaksflimmer så att den normala rytmen inte längre kan återskapas.

I takt med att arytmin fortskrider sätts behandling in som innefattar medicinering, elkonvertering, och i ett sent skede även kirurgiskt ingrepp, i fall detta tillåts av patientens allmänna tillstånd. Det vanligaste kirurgiska ingreppet är ablation under vilka katetrar förs in i förmaken för att med hjälp av värmeenergi elektriskt isolera de delar av förmaken som tros driva flimret.

I dagsläget genomförs ablationer oftast enligt en standardstrategi som går ut på att isolera det område där forskning har visat att de flesta flimmerattacker uppstår. Det har dock visat sig att en del patienter återfaller till förmaksflimmer efter ablation och därför kan upprepade ingrepp bli nödvändiga. Ett sätt att förbättra effektiviteten är att utveckla metoder som kan kvantifiera utbredningsmönstret och peka ut kritiska områden för ablation. I denna avhandling har en metod utvecklats för detta syfte som analyserar de tidpunkter då en elektrisk utbredningsvåg passerar vissa elektroder på katetrarna som spelar in signalerna i förmaken. Målet är att rekonstruera den elektriska utbredningen genom att knyta samman tidpunkterna från olika platser i förmaken till vågfronter. Att detektera tidpunkterna och framförallt att bestämma vilka tidpunkter som tillhör till samma vågfront är utmaningen i denna metod, vilket kan kompliceras ytterligare då utbredningen är mer oregelbunden. En mer avancerad strategi har därefter utvecklats som analyserar signalerna i sin helhet istället för att detektera tidpunkterna. Metoden är baserad på en princip som kallas Granger-kausalitet och som analyserar utbredningsmönstret genom att bestämma orsakssambanden mellan signalerna. I denna metod antas det finnas ett direkt samband mellan varje signal, ett antagande som dock inte är realistiskt under förmaksflimmer där utbredningen av den elektriska aktiviteten är mindre organiserad och där kopplingarna kan förmodas avta med stigande avstånd. Det har därför även utvecklats en förbättrad metod för analys av Granger-kausalitet där antagandet om glesa kopplingar införlivats, vilket har lett till en markant förbättring av resultaten.

För att minska riskerna för patienten samt att sänka kostnaderna är det också intressant att utforska hur mycket information om utbredningsmönstret som kan observeras i signaler inspelade på kroppsytan. Eftersom inspelningar på kroppsytan avspeglar hela hjärtats elektriska aktivitet, är det oftast nödvändigt att i ett första steg utvinna den elektriska aktiviteten som motsvarar förmaken. I ett nästa steg kan denna aktiviteten analyseras, t.ex. med hänsyn till sin spatiella komplexitet. I denna avhandling presenteras en metod för detta syfte, och resultaten antyder att det kan finnas ett samband mellan spatiell komplexitet observerad på kroppsytan och förmaksaktivitetens organisationsgrad.

# Abstract

This doctoral thesis is in the field of biomedical signal processing with focus on methods for the analysis of atrial fibrillation (AF). Paper I of the present thesis addresses the challenge of extracting spatial properties of AF from body surface signals. Different parameters are extracted to estimate the preferred direction of atrial activation and the complexity of the atrial activation pattern. In addition, the relation of the spatial properties to AF organization, which is quantified by AF frequency, is evaluated. While no significant correlation between the preferred direction of atrial activation and AF frequency could be observed, the complexity of the atrial activation pattern was found to increase with AF frequency.

The remaining three papers deal with the analysis of the propagation of the electrical activity in the atria during AF based on intracardiac signals. In Paper II, a time-domain method to quantify propagation patterns along a linear catheter based on the detected atrial activation times is developed. Taking aspects on intra-atrial signal organization into account, the detected activation times are combined into wavefronts, and parameters related to the consistency of the wavefronts over time and the activation order along the catheter are extracted. Furthermore, the potential relationship of the extracted parameters to established measures from body surface signals is investigated. While the degree of wavefront consistency was not reflected by the applied body surface measures, AF frequency could distinguish between recordings with different degrees of intra-atrial signal organization. This supports the role of AF frequency as an organization measure of AF.

In Paper III, a novel method to analyze intracardiac propagation patterns based on causality analysis in the frequency domain is introduced. In particular, the approach is based on the partial directed coherence (PDC), which evaluates directional coupling between multiple signals in the frequency domain. The potential of the method is illustrated with simulation scenarios based on a detailed ionic model of the human atrial cell as well as with real data recordings, selected to present typical propagation mechanisms and recording situations in

atrial tachyarrhythmias. For simulated data, the PDC is correctly reflecting the direction of coupling and thus the propagation between all recording sites. For real data, clear propagation patterns are identified which agree with previous clinical observations. Thus, the results illustrate the ability of the novel approach to identify propagation patterns from intracardiac signals during AF which can provide important information about the underlying AF mechanisms, potentially improving the planning and outcome of ablation. However, spurious couplings over long distances can be observed when analyzing real data comprised by a large number of simultaneously recorded signals, which gives room for further improvement of the method.

The derivation of the PDC is entirely based on the fit of a multivariate autoregressive (MVAR) model, commonly estimated by the least-squares (LS) method. In Paper IV, the adaptive group least absolute selection and shrinkage operator (LASSO) is introduced in order to avoid overfitting of the MVAR model and to incorporate prior information such as sparsity of the solution. The sparsity can be motivated by the observation that direct couplings over longer distances are likely to be zero during AF; an information which has been further incorporated by proposing distance-adaptive group LASSO. In simulations, adaptive and distance-adaptive group LASSO are found to be superior to LS estimation in terms of both detection and estimation accuracy. In addition, the results of both simulations and real data analysis indicate that further improvements can be achieved when the distance between the recording sites is known or can be estimated. This further promotes the PDC as a method for analysis of AF propagation patterns, which may contribute to a better understanding of AF mechanisms as well as improved AF treatment.

# Preface

This doctoral thesis comprises an introduction and four parts describing methods for characterizing atrial fibrillation both from the electrocardiogram (ECG) and from intracardiac recordings. The parts are based on the following papers:

[1] U. Richter, M. Stridh, A. Bollmann, D. Husser and L. Sörnmo, "Spatial Characteristics of Atrial Fibrillation Electrocardiograms", *Journal of Electrocardiology*, vol. 41, pp. 165–172, 2008.

[2] U. Richter, A. Bollmann, D. Husser and M. Stridh, "Right Atrial Organization and Wavefront Analysis in Atrial Fibrillation", *Medical & Biological Engineering & Computing*, vol. 47, pp. 1237–1246, 2009.

[3] U. Richter, L. Faes, A. Cristoforetti, M. Masè, F. Ravelli, M. Stridh and L. Sörnmo, "A Novel Approach to Propagation Pattern Analysis in Intracardiac Atrial Fibrillation Signals", *Annals of Biomedical Engineering*, 2010 (in press).

[4] U. Richter, L. Faes, F. Ravelli and L. Sörnmo, "Propagation Pattern Analysis in Intracardiac Atrial Fibrillation Signals Based on Sparse Modeling", 2010, Manuscript.

The development, implementation, and evaluation of the signal processing algorithms was in all presented papers conducted by the author of this thesis, except for the simulation scenarios included in [3]. Support for the clinical interpretation of the results was provided by experienced cardiologists. Parts of the work have also been presented at conferences but are not included in the thesis:

[5] U. Richter, M. Stridh, A. Bollmann, D. Husser and L. Sörnmo, "Spatial Characteristics of Atrial Fibrillation Using the Surface ECG," *Proc. Computers in Cardiology*, vol. 34, pp. 273–276, 2007.

[6] U. Richter, M. Stridh, D. Husser, D. S. Cannom, A. K. Bhandari, A. Bollmann and L. Sörnmo, "Wavefront Detection from Intra-Atrial Recordings," *Proc. Computers in Cardiology*, vol. 34, pp. 97–100, 2007.

[7] U. Richter, A. Bollmann, D. Husser and M. Stridh, "Right Atrial Organization and Wavefront Analysis in Atrial Fibrillation", *Electrocardiology 2009 - Proc. 36th International Congress on Electrocardiology*, pp. 271–278, 2009.

[8] U. Richter, L. Faes, A. Cristoforetti, M. Masè, F. Ravelli, M. Stridh and L. Sörnmo, "A Novel Approach to Investigating Propagation Patterns in Endocardial Atrial Fibrillation Signals", *The 37th International Congress on Electrocardiology*, 2010.

# Acknowledgments

It is a great pleasure to thank everyone who supported me on my way to become a PhD. While there are many that I would like to thank in specific, I am only able to mention a few, and hope that the rest of you know that I am ever grateful.

First of all, I want to express my gratitude to my supervisor Leif Sörnmo, who has inspired and supported me throughout my entire time as a PhD student. Thank you for always cheering me up with one of your great puns, I will be missing them. I am also grateful to Martin Stridh, who supervised me during parts of my thesis and introduced me to the interesting field of intracardiac signal processing. A warm thanks goes to Frida Sandberg, who I had the pleasure to share an office with during my time at the department. I think we had a great finish! I would also like to thank Danny Smith, Kristian Solem, and the rest of the signal processing group for interesting discussions and their support.

I am also thankful to my Italian colleagues in Trento which I visited in summer 2009, especially Flavia Ravelli, Giandomenico Nollo, Luca Faes, Michela Masè, and Alessandro Cristoforetti. Research-wise, our collaboration turned out to be a perfect match indeed. Research aside, I want to thank you for making me feel welcome not only as a colleague, but also as a friend from the very first moment. I really appreciated our trips to the mountains, the evenings with great Italian food, and all more there was. An additional thanks goes to Silvia Erla for the company at the office and to Francesco Tessarolo for being such a great guide to Venice and letting me be a guest at your parents' place – I'll never forget your mother's carpaccio.

I also want to show my gratitude to all colleagues at the EIT department, who I had the great pleasure to meet at some time on my way towards the PhD. The interesting mix of people, not the least due to our different nationalities, has made my time here most enjoyable. What I will certainly miss are the entertaining discussions about all and nothing during our coffee and lunch breaks, and I want to thank especially Johan Kåredal, Johan Löfgren, and

Frida Sandberg for keeping them at such a high level. I also want to send a warm thank you to Isael Diaz and Marco Munguía, who supported and cheered me up especially during my last weeks of writing, as well as Peter Hammarberg, Anders J Johansson, Palmi Thor Thorbergsson, Fredrik Tufvesson, and Meifang Zhu. Furthermore, I am certainly thankful to the administrative and technical staff for pulling the right strings in the background, making things work so smoothly.

I also want to thank all my friends, not the least those of you with which I share the passion for dancing – clearing my head with some swingouts after a working day has never failed me. Finally, I wish to thank my family, for all their love and support, and for always being there for me.

Ulrike Richter

# List of Acronyms

**ABS** average beat subtraction

**AF** atrial fibrillation

**AIC** Akaike information criterion

**AR** autoregressive

**AV** atrioventricular

**BIC** Bayesian information criterion

**BSPM** body surface potential mapping

**CFAE** complex fractionated atrial electrogram

**CNR** Courtemanche–Nattel–Ramirez

**CS** coronary sinus

**CWT** continuous wavelet transform

**DACL** dominant atrial cycle length

**DC** directed coherence

**dDTF** directed DTF

**DF** dominant frequency

**DTF** directed transfer function

**ECG** electrocardiogram

**EP** electrophysiological

**FA** false alarm

**FIR** finite impulse response

**FN** false negative

**FP** false positive

**FT** Fourier transform

**IIR** infinite impulse response

**LA** left atrium

**LARS** least angle regression selection

**LASSO** least absolute selection and shrinkage operator

**LS** least-squares

**MSC** magnitude-squared coherence

**MVAR** multivariate autoregressive

**PDC** partial directed coherence

**PV** pulmonary vein

**RA** right atrium

**SA** sinoatrial

**SD, std** standard deviation

**TN** true negative

**TP** true positive

**VCG** vectorcardiogram

# Contents

# Part I

# Overview of the Research Field

# Chapter 1

# Introduction

The present thesis deals with spatial characterization of the cardiac arrhythmia atrial fibrillation (AF) using intracardiac as well as body surface signals. AF is the most common sustained cardiac rhythm disturbance and has become an extremely costly public health problem [1]. The prevalence of AF increases with age, and besides a pronounced reduction of quality of life, AF is also associated with an increased long-term risk of stroke and all-cause mortality.

Although much has already been learnt about the mechanisms of AF, they still remain incompletely understood. In order to increase the success of therapy in a majority of patients, a better understanding of the mechanisms of AF initiation and perpetuation is of vital importance. In current clinical practice, surgical treatment of AF is mainly restricted to a standard procedure. During this procedure, a certain region of tissue, which has been observed to trigger AF, is destroyed in a controlled manner ("ablation therapy"). However, recognizing that the mechanisms of AF may vary from patient to patient, an individualized approach to ablation guidance is highly desirable. It has already become apparent that such a development will not be possible without further advancement of signal processing techniques, e.g., individualized ablation therapy has been based on frequency analysis of intracardiac signals. In the future, signal-guided approaches to ablation can be expected to gain further importance, requiring methods which can handle the strongly varying organization of AF signals, as well as the increasing number of simultaneously recorded signals.

In order to reduce the amount of invasive procedures, and consequently the cost of AF treatment, further research on the possibilities to assess the underlying mechanisms of AF by means of non-invasive methods is important to promote. Analysis of body surface signals during AF is particularly challenging, as the recordings are made distant from the actual signal source. As

a consequence, the spatial resolution which can be provided by body surface recordings is limited, and opposed to intracardiac signals, the global electrical activity of the heart is reflected. Furthermore, the validation of the results is non-trivial, especially as detailed information about the actual spatial organization and propagation within the atria, ideally extracted from simultaneously recorded intracardiac signals, is seldom available. It is not yet clear to what extent body surface signal analysis can provide information relevant to the complex mechanisms that underlie AF. However, successful signal processing contributions based on body surface signals have already been made to, e.g., the prediction of termination or recurrence of AF, and the monitoring of antiarrhythmic drug effects.

Paper I addresses the challenge of extracting spatial properties of AF from body surface signals by evaluating the potential relationship between the spatial properties and AF organization. The remaining three papers of this thesis deal with the problem of analyzing the propagation of the electrical activity in the atria during AF based on intracardiac signals. In Paper II, a time-domain method to quantify propagation patterns along a linear catheter is developed. Parameters related to the consistency of the wavefronts over time and the activation order along the catheter are extracted and their potential relationship to established measures from body surface signals is investigated. In Paper III, a novel method to analyze intracardiac propagation patterns based on causality analysis in the frequency domain is introduced. One of the advantages of the method is that it can quantify the directional coupling and identify the propagation pattern between the recording sites by employing a multivariate approach that simultaneously evaluates all signals. The potential of the method is further strengthened by several simulation scenarios of atrial activity propagation, based on a detailed ionic model of the human atrial cell. However, spurious couplings over long distances can be observed when analyzing real data comprised by a large number of simultaneously recorded signals. Thus, in Paper IV, an improvement of the method by incorporating prior information on sparsity as well as the distances between the recording sites is proposed.

The following chapters of this thesis give an overview over the research field, starting with a background on the heart and AF, as well as measurement and simulation of cardiac electrical activity, in Chapter 2. Signal processing techniques for AF analysis based on body surface and intracardiac signals are reviewed in Chapters 3 and 4, respectively. Finally, a summary of the included papers can be found in Chapter 5.

# Chapter 2

# Background on the Heart and Atrial Fibrillation

## 2.1 Anatomy of the heart

The heart is a muscle that continuously pumps oxygenated blood from the lungs to the tissue throughout the body, and transports the blood with carbon dioxide away from the tissue towards the lungs. Figure 2.1 shows the anatomy of the heart with the major blood vessels and the four chambers, of which two lie in the left, and another two in the right side of the heart. The two sides of the heart are divided by a muscular wall called septum. Each of the two sides are further divided into an atrium, which is the upper chamber that receives blood from the veins, and a ventricle, which is the lower chamber that pumps blood into the arteries.

## 2.2 The heart during normal sinus rhythm

The activity of the heart can either be described as a series of mechanical events, i.e., a sequence of muscle contractions and relaxations, or as a series of electrical events. In electrical terms, the contraction and relaxation phases are referred to as depolarization and repolarization, respectively. Each heartbeat is triggered by an electrical impulse that starts in the sinoatrial (SA) node, which is positioned in the right atrium (RA), see Fig. 2.1. The SA node sets the rhythm of the heart, which is why normal heart rhythm is also called sinus rhythm. The electrical activity spreads through the walls of the atria, causing them to contract. The atrioventricular (AV) node, situated at the

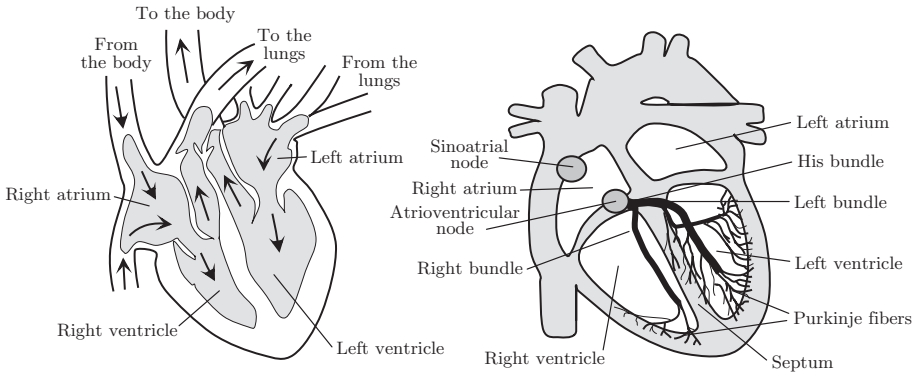


**Figure 2.1:** Anatomy of the heart. Reprinted with permission from [2].

center of the heart between the atria and ventricles, collects and slows the electrical signal before it enters the ventricles, giving the atria time to contract before the ventricles do. Surrounding the AV node there is insulation such that the electrical impulse can only propagate further over the His bundle to the rapidly conducting left and right bundle branches and from there to the Purkinje fibers. These fibers conduct the electrical impulse to the muscular walls of the ventricles, which contract and force the blood out of the heart to the lungs and body. This completes the electrical cycle of one heartbeat.

## 2.3 The heart during atrial fibrillation

Atrial fibrillation is a supraventricular arrhythmia, i.e., an arrhythmia that has its origin above the ventricles, such as in the atria. Instead of that every heartbeat starts by a single electrical impulse from the SA node, several impulses with varying origin spread throughout the atria and cause uncoordinated atrial contractions. Although not all electrical impulses from the atria propagate further through the AV node to the ventricles, the ventricular rhythm during AF becomes rapid, "disorganized", and irregular. These characteristics lead to increased risk for formation of blood clots in the atria, which in turn leads to increased long-term risk of stroke. The mortality rate of patients with AF is about twice that of patients in normal sinus rhythm, although AF itself is not generally considered life-threatening.

The underlying mechanisms of AF are still the subject of research, and so far, three main theories on AF mechanisms have evolved. Moe's multiple

wavelet hypothesis [3] states that multiple wavelets are propagating on varying routes throughout both atria, randomly activating the atrial tissue and thus leading to the complex electrical patterns observable during AF. The second theory emerged as Haissaguerre et al. observed that AF is often triggered by a focal source [4–6]. Most often, such focal triggers were observed in the left atrium (LA) close to the pulmonary veins (PVs), but other origins were also found, such as the superior vena cava. The role of the LA as a trigger of AF is further supported by studies revealing left-to-right atrial frequency gradients [7, 8]. The third mechanism is based on the presence of an appropriate heterogeneous AF substrate, which allows that a focal trigger can result in sustained high frequency reentrant AF drivers (rotors) [9]. This mechanism is more likely to occur when AF is maintained for relatively long time periods, which has been shown to result in a more complex arrhythmogenic substrate due to atrial remodeling, i.e., the shortening of action potential duration as well as refractory period [10].

## 2.4 Treatment of atrial fibrillation

Treatment of AF follows three main objectives [1]:

- heart rate control,
- prevention of thromboembolism, and
- correction of the rhythm disturbance.

Different factors influence the decision about which treatment to choose. Besides the age of the patient and other underlying heart diseases being typical for AF patients, the clinical type of AF must also be considered. Patients with acute AF, i.e., in their first AF episode, are usually treated with immediate cardioversion in order to restore sinus rhythm. In case AF terminates spontaneously in less than 7 days, AF is designated as paroxysmal. The treatment then focuses on the suppression of paroxysms, heart rate control during paroxysms, and long-term maintenance of sinus rhythm. AF that is not self-terminating and lasts longer than 7 days is referred to as persistent and is treated with cardioversion. AF that is non-terminating even after attempted cardioversion is referred to as permanent and is treated by heart rate control.

If pharmacological treatment for heart rate control fails, heart surgery may be considered. The first surgical procedure for AF was the Maze procedure, which required open heart surgery and was based on Moe's multiple wavelet hypothesis [11]. During this procedure a series of linear lesions was carried out both in the right and left atrium in order to confine the electrical impulses to

defined pathways towards the AV node. The Maze procedure was later replaced by the rapidly advancing technique of radiofrequency catheter ablation, which does not require open heart surgery. Following the findings of the LA as a driver of AF, ablation of the RA was abandoned, and ablation of the LA became more selective. As the majority of ectopic foci have been observed in the PVs, PV isolation has become the standard ablation procedure. During the ablation, the electrical signals from the PVs are under continuous observation, and a termination of electrical activity indicates that isolation has been achieved. The success rate of PV isolation in paroxysmal AF has been reported to be from 38 to 70% after a single procedure and from 65 to 90% after repeated procedures [10].

However, in the presence of persistent AF, PV isolation alone is less effective [10], as it is very likely that atrial remodeling has taken place. This process leads to a more complex arrhythmogenic substrate, which may promote sustained AF by augmenting the number of AF drivers and shifting their location away from the PVs. Thus, additional linear ablations or focal lesions may be necessary in order to prevent AF from recurring. While PV isolation is guided by the anatomy, these additional ablations are guided by the electrograms, which are employed in order to identify the arrhythmogenic substrate or the additional ectopic foci. In that context, areas with complex fractionated electrograms (CFAEs), i.e., electrograms with highly fractionated potentials or with a very short cycle length ($\leq$ 120 ms), have been reported to potentially represent AF substrate sites and become target sites for AF ablation [12]. Although this approach has gained much popularity and automatic CFAE mapping systems have been proposed [13,14], there are also studies questioning the efficiency of CFAE ablation [15,16], indicating the need for further research in this area.

## 2.5 Measuring cardiac electrical activity

Cardiac electrical activity can be measured on the body surface as well as from inside the heart. While body surface signals reflect the global cardiac electrical activity, i.e., the sum of the activity in the atria and ventricles, intracardiac recordings allow the measurement of local cardiac electrical activity. In the following, an overview of both types of measurements is given.

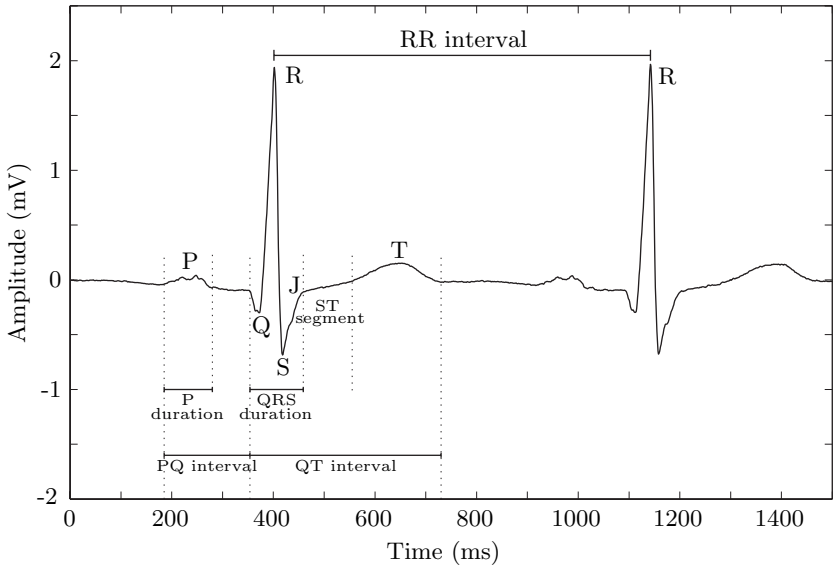


**Figure 2.2:** The cardiac cycle in sinus rhythm as observed in the ECG. Reprinted with permission from [2].

### 2.5.1 Body surface signals

#### The electrocardiogram

The cardiac cycle, as represented by the electrocardiogram (ECG), consists of several characteristic waves which are shown in Fig. 2.2. During sinus rhythm, the beginning of the cardiac cycle is denoted P wave, which reflects the depolarization of the atria. The subsequent depolarization of the ventricles is denoted QRS complex, which at the same time masks the atrial repolarization. At the end of the cardiac cycle the T wave occurs which reflects ventricular repolarization.

In AF, coordinated depolarization of the atria no longer takes place. This is reflected in the ECG by the replacement of the P waves by an undulating baseline, i.e., f waves. ECG examples of sinus rhythm, atrial flutter, and AF are displayed in Fig. 2.3. Similar to AF, atrial flutter is a supraventricular arrhythmia. It is typically caused by a reentrant activation circuit involving the entire RA. In the ECG, atrial flutter is characterized by so-called F waves, which in contrast to the f waves during AF exhibit a more regular, sawtooth-like appearance. The ventricular response is also regular, leading to that atrial

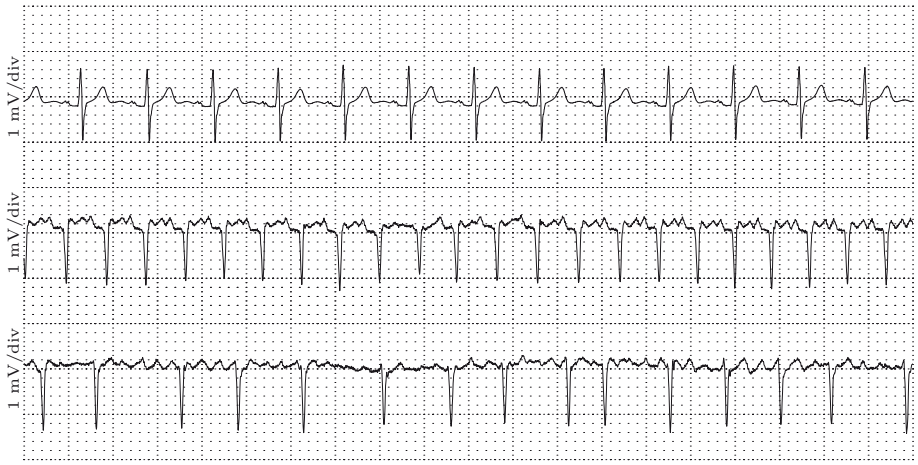


**Figure 2.3:** ECG signals with sinus rhythm (upper panel), atrial flutter (middle panel), and AF (lower panel). Reprinted with permission from [2].

flutter is often described as an arrhythmia being more organized than AF.

The standard 12-lead ECG is the most common lead system for recordings on the body surface and is defined by 10 electrode positions: one electrode on each of the left arm, right arm, and left leg, six electrodes on the chest, and one electrode which is used as ground, usually positioned on the right leg. From these electrodes, the three bipolar limb leads I, II, and III, the three augmented unipolar limb leads aVF, aVL, and aVR, as well as the six precordial leads V1,...,V6 are obtained. Because of its close proximity to the RA, lead V1 is often thought of as reflecting mostly right atrial activity, which has been confirmed by clinical studies that compared certain characteristics of the ECG with simultaneously recorded intracardiac signals from both atria [17,18]. In [18], the standard, but infrequently used, leads V7, V8, and V9 were also recorded, and a high correlation was found between lead V9 and activity from the LA.

In order to improve the analysis of atrial activity from the ECG, both body surface potential mapping (BSPM) with a large number of electrodes on the front as well as the back of the body [19, 20], and special lead systems such as the atriocardiogram [21] have been proposed. However, it is yet to be seen whether these systems will be used in clinical practice.

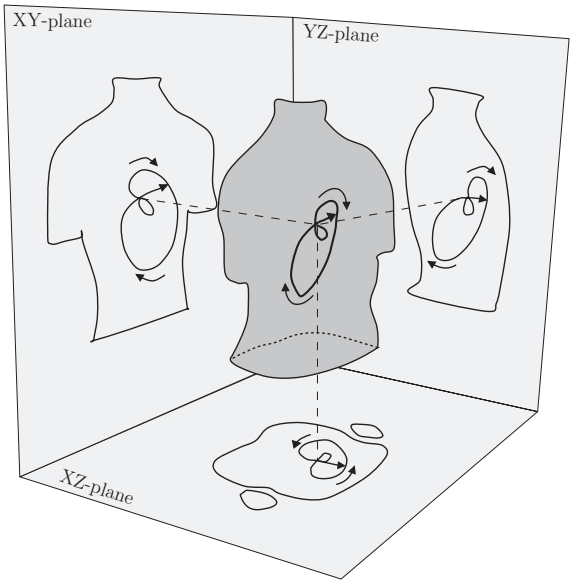


**Figure 2.4:** A vectorcardiographic loop, corresponding to one heart cycle, and its projection onto the three orthogonal planes. Reprinted with permission from [2].

### The vectorcardiogram

The basic idea behind the vectorcardiogram (VCG) is that the electrical activity of the heart at each time instant during the cardiac cycle can be summed to a vector, which describes the size and direction of the electrical activity in the three-dimensional (3-D) space. This vector is commonly referred to as the equivalent dipole $\mathbf{D}_E(t)$, which is composed by the three orthogonal components $D_{Ex}(t)$, $D_{Ey}(t)$, and $D_{Ez}(t)$. The VCG is a display of the equivalent dipole on the body surface, and ideally, the three orthogonal components of the VCG, i.e., the X, Y, and Z lead, are directly proportional to the corresponding component of $\mathbf{D}_E(t)$. When the X, Y, and Z leads are plotted at successive time instants, a vector loop is constructed in the 3-D space, see Fig. 2.4. The XY-, XZ-, and YZ-plane are also referred to as frontal, transverse, and sagittal plane, respectively.

The Frank lead system, named after its inventor, is probably the best-known system for orthogonal leads. It requires seven electrodes that are positioned on the chest, back, neck, and left foot. However, as the standard 12-lead ECG is more common in clinical practice, various approaches to synthesize the VCG

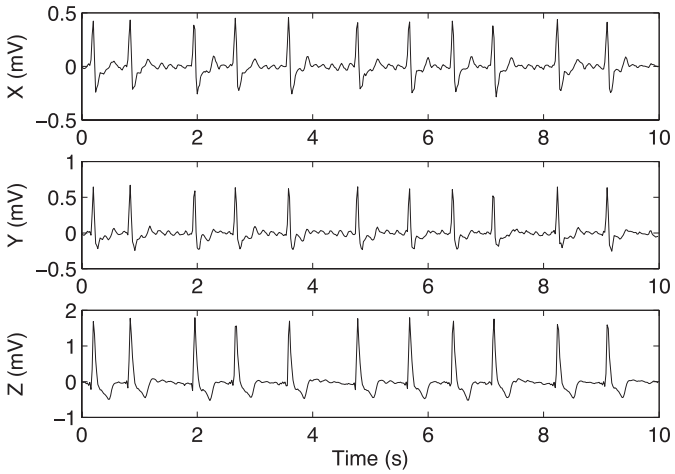


**Figure 2.5:** 10 seconds of synthesized VCG signals during AF.

from the 12-lead ECG have been investigated [22–24]. The synthesis of leads relies on the assumption that the voltage at any point of the body can be approximated as a linear combination of the recorded 12 leads.

An example showing one second of VCG signals during AF, synthesized with the inverse Dower matrix [25], is shown in Fig. 2.5. The inverse Dower matrix was originally developed with focus on the QRS complex. Recently, several studies have investigated the performance of the inverse Dower matrix for analysis of P waves [26, 27] and atrial activity during AF [28]. While the inverse Dower transform has been found useful for studying P wave morphology [26], a new atrial-based transform matrix [27] as well as a new transform matrix based on a new lead system [28] have been proposed.

### 2.5.2 Intracardiac signals

A complete intracardiac evaluation of supraventricular arrhythmias such as AF is performed during electrophysiological (EP) studies, involving the use of multiple catheters with several recording electrodes as well as a programmable stimulator [29]. The stimulator can be used for various purposes, e.g., to provoke arrhythmia in case the patient had sinus rhythm at the onset of the procedure. In order to navigate the catheter during the procedure, fluoroscopy equipment is needed. Fortunately, the exposure to radiation is decreasing thanks to the introduction of new 3-D mapping systems. One example is CARTO, which is a non-fluoroscopic electromagnetic mapping system. The usual procedure is to

insert several catheters into the heart through the vein in the patient's groin, which does not require anesthesia.

A variety of catheters are available, differing in the number of electrodes, electrode spacing, and curves. One category of catheters are the deflectable ones that facilitate positioning for mapping and can deliver radiofrequency energy through their tips for ablation. Another category are the deflectable catheters with multiple electrodes that allow simultaneous recording at multiple sites, covering larger areas of the atrium. Examples are the Halo catheter (Fig. 2.6(a) and (b)), which has its name from being formed like a "halo", and the basket catheter (Fig. 2.6(c)), which has up to 64 electrodes. The typical distance between two electrodes on a catheter is 2–5 mm [30], and the electrical potential measured between two electrodes is called a bipolar electrogram.

While the response to programmed stimulation can provide information on the mechanisms of initiation of AF, mapping studies can provide insight into the mechanisms of AF perpetuation. Mapping studies can be either epicardial or endocardial. Epicardial mapping is performed during open heart surgery by placing arrays which can contain several hundred electrodes on the outer surface of the heart. In contrast, endocardial mapping is done on the inside of the heart and can be further divided into contact and non-contact mapping. During contact mapping, the electrodes of the catheter have direct contact with the wall of the heart, while in non-contact mapping the electrodes of the catheter are placed in the center of the heart chamber and act as antennas. An example of a contact mapping catheter is the basket catheter. The large number of electrodes makes it possible to study spatiotemporal organization during AF as well as to evaluate the complexity or morphology of the signals at multiple sites in the atrium.

Recordings of several intracardiac signals are shown for two examples in Fig. 2.7. The time instant when an electrical impulse passes the tissue close to an electrode, the cardiac cells rapidly depolarize, causing steep deflections in the recording. Such a waveform is called an activation, and the time delay between two subsequent activations defines the cycle length. While the example in Fig. 2.7(a) exhibits distinct activations, e.g., in the catheter in the RA, it is difficult to distinguish between single activations in the RA recording displayed in Fig. 2.7(b).

## 2.6 Simulating atrial electrical activity

While simulation models for the atrial electrical activity originally were developed for healthy subjects, large efforts have recently been made to employ these models for simulation of atrial arrhythmias. Such simulations can not

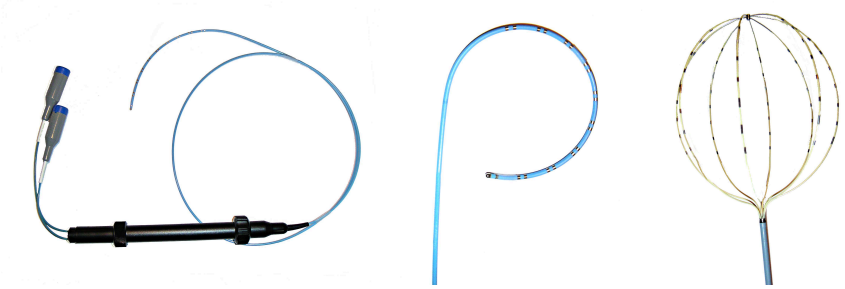

(a) (b) (c)

**Figure 2.6:** (a) Complete Halo catheter including the plugs for the measurement equipment and the steering handle. (b) Top of the Halo catheter when formed as a "halo", showing the electrode pairs. (c) Top of a basket catheter.

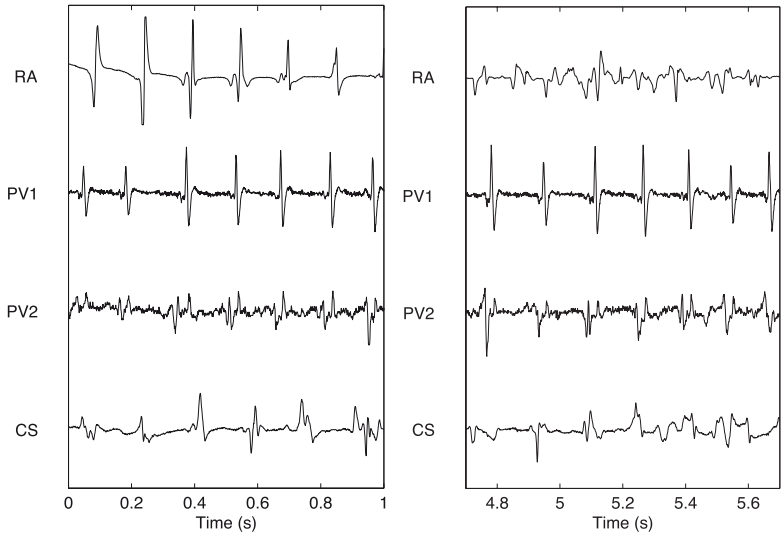


(a) (b)

**Figure 2.7:** Two examples of intracardiac signals recorded with a Halo catheter in the RA, a pulmonary vein catheter in the LA (PV1, PV2), as well as a coronary sinus (CS) catheter.

only contribute to better understanding of atrial arrhythmia mechanisms, but can also help to validate research methods, evaluate therapeutic approaches, or even aid diagnosis.

The simulation of atrial activity is a complex mathematical problem, which is usually based on a bottom-up approach. After formulating a model for a single atrial cell, the cells are coupled to form a tissue for which a propagation model is defined. Next, a geometric model is constructed to reproduce, e.g., cardiac anatomy. Finally, a simulation scenario is set up and measurement devices, such as catheter electrodes or ECG leads, are simulated.

### 2.6.1 Atrial cell models

The membrane of the cell is modeled as a capacitor connected in parallel with variable resistances and batteries which represent ionic channels and driving forces. The total ionic current $I_{ion}$, given per unit area of membrane, is responsible for the temporal variations of the membrane potential $V_m$ according to [31]

$$C_m \frac{\partial V_m}{\partial t} = -I_{ion} + I_{stim}, \tag{2.1}$$

where $C_m$ is the membrane capacitance per unit area of membrane, and $I_{stim}$ is an external stimulus used to trigger an action potential. For definition of $I_{ion}$ in the human atrial cell, the Courtemanche–Nattel–Ramirez (CNR) model [32] has received the most attention. It defines $I_{ion}$ as a sum of 12 separate contributions, which represent the ionic and pump currents known to contribute to the action potential in human atrial cells.

### 2.6.2 Propagation model

Cardiac tissue can be described as a collection of cells which are interconnected to their neighbors through gap junctions. In order to assume continuous homogenous propagation in the tissue, the intracellular medium, the cell membranes, and the extracellular medium are homogenized so that the three domains obtain the same continuous physical space $\Omega_{myo}$ (myocardium). Under the further assumption that the conductivity tensor fields of the intra- and extracellular media are identical apart from a constant factor, the propagation can be described by the so-called monodomain equation [31]

$$C_m \frac{\partial V_{tm}}{\partial t} = C_m \nabla \cdot \mathbf{D} \nabla V_{tm} - I_{ion} + I_{stim}, \tag{2.2}$$

where $V_{tm}$ is the transmembrane potential and $\mathbf{D}$ is the diffusion tensor.

The formulation of the monodomain equation is flexible enough to permit the incorporation of information about substrate properties and changes induced by therapy. For example, the diffusion tensor $\mathbf{D}$, which models the cell-to-cell coupling and thus determines the conductivity, is in most models set to uniform. However, it can be altered in order to incorporate regions of slow or high conduction, or to simulate ablation, where the tissue conductivity is set to zero at the ablation lines. Furthermore, the membrane kinetics as modeled by $I_{ion}$ can be altered to, e.g., simulate drug therapy, but also to create a substrate for arrhythmia [33]. The creation of such a substrate has shown to have large impact on the dynamics of depolarization waves and spirals, and on the occurrence of conduction blocks and reentry. Finally, device therapy such as pacing or defibrillation can be simulated by applying a stimulus current ($I_{stim}$).

### 2.6.3 Geometric models

Simulations can be done in the isolated cell, 1-D cable, 2-D tissue, as well as 3-D models. In the latter, variations in the wall thickness are sometimes omitted, and the 3-D model is implemented as a monolayer 2-D surface embedded in 3-D space. The simplest 3-D model is the approximation of the geometry of the atria as two spheres. In the next step, also landmarks of the topology, i.e., holes corresponding to the insertion of veins and valves, can be included. With the help of medical imaging modalities, e.g., magnetic resonance imaging, it is already possible to generate more realistic and even patient-specific geometries. Such realistic models can incorporate variations in wall thickness, fast-conducting bundles, and inter-atrial connections.

For the solution of the monodomain equation, see Eq. (2.2), a spatial discretization of the atrial geometry and structures must be performed, e.g., through standard finite volume or finite element methods. In the cardiac context, this has been described for triangular, cubic, and hexahedral meshes. A detail of a triangular mesh is shown in Fig. 2.8(a), which illustrates how a simulation of a reentry around an anatomical obstacle can be initiated on a monolayer sphere with a diameter of 6 cm. The triangular mesh comprises approximately 125.000 nodes, resulting in a spatial resolution of about 300 $\mu$m. In order to initiate the reentry, a point source and a temporary line of block are placed on the sphere in addition to the anatomical obstacle. The simulation is started by delivering a single electrical impulse from the point source, which is situated in proximity to the anatomical obstacle and the line of block, see Fig. 2.8 (b). The electrical activity is then propagating around the anatomical obstacle and along the line of block as can be seen in Figs. 2.8(c) and (d). The dimension of the sphere and the anatomical obstacle must be chosen such that

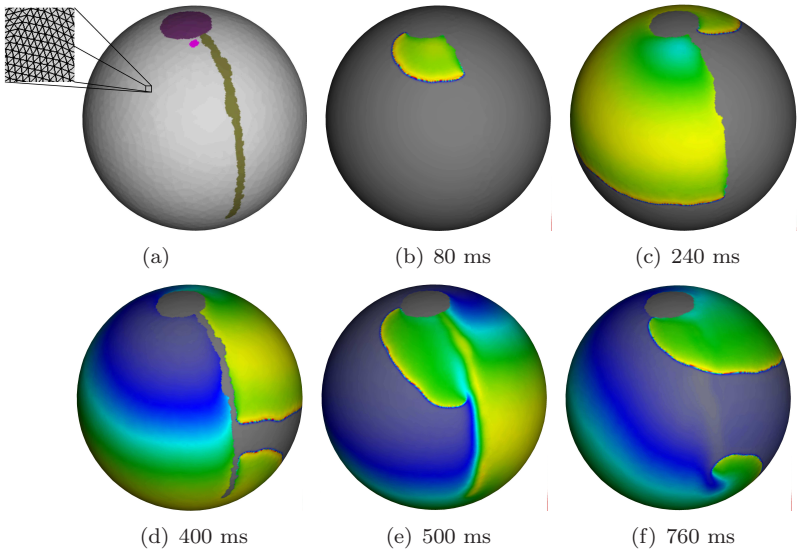

(a) (b) 80 ms (c) 240 ms

(d) 400 ms (e) 500 ms (f) 760 ms

**Figure 2.8:** Illustration of a simulation with a reentry initiated around an anatomical obstacle. (a) Sphere with the anatomical obstacle (large circle), a line of block, and a point source (small circle). An enlarged detail of the triangular mesh is also shown. (b)–(f) Snapshots of the membrane voltage at subsequent time instants, see text for details.

the tissue close to the point source, where the propagation is started, is in repolarization when the propagation has reached around the anatomical obstacle. The subsequent removal of the line of block then allows the establishment of a self-sustained activation of the tissue, see Figs. 2.8(e) and (f).

### 2.6.4 Measurement of the atrial electrical activity

The solution of the monodomain equation can be employed to compute the transmembrane current $I_{tm}$ (per unit area), which is needed to obtain the unipolar electrograms [31]

$$\phi(\mathbf{x},t) = \frac{1}{4\pi\sigma_e}\int_{\Omega_{myo}} \frac{I_{tm}(\mathbf{y},t)}{||\mathbf{x}-\mathbf{y}||} d\mathbf{y}, \tag{2.3}$$

where the vector $\mathbf{x}$ is the simulated location of the electrode close to the surface of the tissue, $t$ is the time, and $\sigma_e$ is the extracellular conductivity. Extensions

of Eq. (2.3) take the finite size of the torso as well as its inhomogenities due to lungs and blood cavity into account, so that also the ECG can be computed [31].

# Chapter 3

# Signal Processing of Atrial Fibrillation on the Body Surface

## 3.1 Preprocessing

Body surface signals can be disturbed by various noise sources, leading to, e.g., baseline wander, powerline interference, and muscle noise [2]. The first two disturbances can be handled by narrowband filters, while for the last, averaging of the time-aligned heartbeats can be applied. However, atrial and ventricular activity are not synchronized during AF, and therefore averaging of the time-aligned heartbeats would not only remove the muscle noise, but also the atrial activity. Thus, during the analysis of AF, ECG segments with excessive muscle noise are often only detected and excluded from further analysis.

In the analysis of AF, atrial activity extraction most often follows noise reduction. Linear filtering is an unsuitable approach for this problem, because the atrial and ventricular activity overlap spectrally. Instead, approaches such as average beat subtraction (ABS) [17], spatiotemporal QRST cancellation [34], and principal as well as independent component analysis [35, 36] have been employed for this purpose. A comparison of the performance of these methods for atrial activity extraction can be found in [37]. In the following, ABS and spatiotemporal QRST cancellation are shortly described in some more detail.

For both ABS and spatiotemporal QRST cancellation, information on the occurrence time of each heartbeat is required. This is handled by a QRS detector which must be able to adapt to sudden changes in QRS morphology and

heart rhythm. The detector is also required to handle ectopic beats, i.e., beats originating from other locations than the SA node. Usually, QRS detection is followed by beat classification, which sorts the detected heartbeats into groups, e.g., by clustering the beats according to their morphology.

During ABS, each ECG lead is processed separately. Following QRS detection and beat classification, the ventricular activity is cancelled by calculating the average beat for each group and subtracting it from the individual heartbeats in the corresponding group. When subtracting the average beat, it is crucial to assure accurate temporal alignment. An erroneous alignment of the average beat can lead to QRST residuals that complicate further analysis. Spatiotemporal QRST cancellation is an extended form of ABS that uses information from several leads for cancellation [34]. This accounts for variations in the orientation of the heart's electrical axis, that are mainly due to respiratory activity. The performance of spatiotemporal QRST cancellation was studied and shown to be superior to ABS, i.e., it results in smaller QRST-related residuals [37]. Figure 3.1 illustrates the performance of spatiotemporal QRST cancellation on two examples.

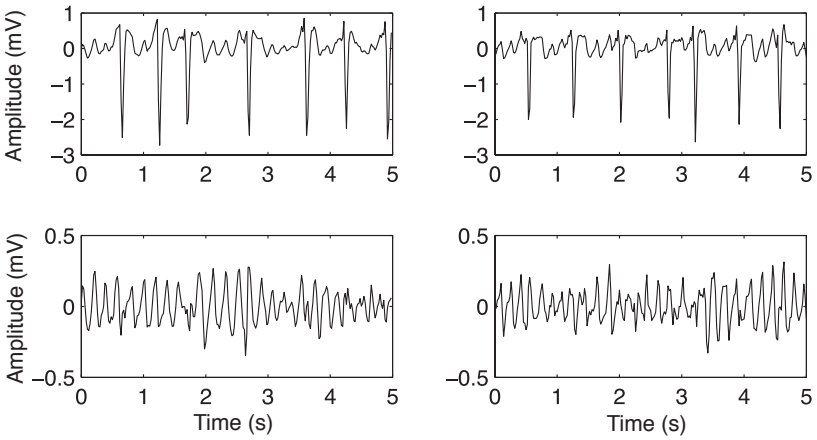


**Figure 3.1:** Two examples illustrating spatiotemporal QRST cancellation. Upper panel: ECG signals with AF. Lower panel: Corresponding extracted atrial activity (note that the amplitude scale is magnified).

## 3.2 Time–frequency analysis

On the body surface, time–frequency analysis is usually applied following atrial activity extraction. In order to track the frequency content of the atrial activity over time, linear or quadratic time-frequency distributions may be applied [38–40]. Typically, each spectrum of the distribution exhibits a distinct peak whose location determines the AF frequency of the corresponding time segment. The purpose of the method presented in [40] is to achieve a more robust estimation of the AF frequency, as well as of the harmonics of the spectrum, when compared to estimation based on the conventional power spectrum. This is achieved by computing local power spectra from successive time segments, which after frequency alignment are used to adaptively update a spectral profile. This profile is then employed to determine the final estimates of AF frequency as well as the exponential decay of the harmonics, which is a measure characterizing the morphology of the atrial waveforms.

There has been an increased interest in tracking of the frequency content of AF signals over time since the observation of atrial remodeling and its coupling to the shortening of the atrial refractory period, which in turn can lead to local differences in atrial cycle length. AF cycle lengths from the RA have been shown to be especially well-represented by the inverse of the AF frequency in lead V1 [17]. In another study, a similar observation was made for the less frequently used standard posterior lead V9 and the LA, and also a significant correlation between inter-atrial (LA to RA) and body surface (V9 to V1) frequency gradients was found [18]. In clinical studies, AF frequency has been used to identify suitable candidates for pharmacological cardioversion [41, 42]. Furthermore, AF frequency was found to predict AF recurrence after cardioversion [43] as well as spontaneous AF termination [44].

## 3.3 Spatial analysis

The potential of the ECG to reveal information about the propagation within the atria has been demonstrated, e.g., during sinus rhythm in patients with paroxysmal AF [45]. The morphology of the P wave in each lead of the synthesized VCG was categorized as either positive, negative, or biphasic. In the vast majority of the patients, the category of the P wave allowed to draw correct conclusions about the left atrial breakthrough site and the corresponding inter-atrial conduction route. Analysis of P wave morphology has also been proposed for localizing the source of atrial ectopic beats which can trigger the onset of paroxysmal AF [46, 47]. In both studies, the analysis was based on previously recorded pacemaps, which contained P waves obtained during pac-

ing at different sites within the LA and RA. However, during AF, the P wave is replaced by continuous f waves, which due to the variety and complexity of mechanisms that maintain AF can be strongly varying in morphology. Thus, more advanced signal processing techniques are needed to evaluate whether different AF mechanisms can be distinguished from the ECG.

Simulations have been proposed to assess the ability of the VCG to identify underlying AF mechanisms [48]. The atrial activity was simulated with the CNR model (see Sec. 2.6), using a thick-walled 3-D model of the atria based on magnetic resonance images and resulting in the membrane potential $V_m$. A compartmental torso model, which included atria, ventricles, and lungs, was also derived from magnetic resonance images and used to compute body surface potential maps of the atrial activity over the entire torso. The potentials at the locations of the nine ECG electrodes of the standard 12-lead system were then selected as simulated ECG signals.

The analysis was based on the equivalent dipole $\mathbf{D}_E(t)$, which was calculated by integrating the membrane potential $V_m$ over the atrial surface, as well as on the VCG, which served as an estimate of $\mathbf{D}_E(t)$ on the body surface. The VCG was synthesized from the simulated ECG signals with a transformation matrix presented in [28]. For further analysis, the three orthogonal components of the VCG were at each time instant projected onto a unit sphere, i.e., the vector magnitude was normalized to one. This resulted in a scatter plot of the vector directions on the sphere. It was hypothesized that the analysis of the spatial distribution of these scatter plots should locate stable and single AF sources such as micro-reentries, mother-rotors or ectopic foci, to the location of peaks in this distribution. In contrast, the absence of such peaks should indicate that the AF dynamic was complex, i.e., there were multiple AF sources or no identifiable source at all. The spatial distributions were analyzed by calculating the eigenvalues $\lambda_1 \geq \lambda_2 \geq \lambda_3$ of the covariance matrix of the VCG, where $\lambda_1 + \lambda_2 + \lambda_3 = 1$ due to the previous normalization. Three extreme distributions can be identified: a point distribution ($\lambda_1 = 1$, $\lambda_2 = \lambda_3 = 0$), a distribution along a circle around the unit sphere ($\lambda_1 = \lambda_2 = 1/2$, $\lambda_3 = 0$), and a uniform distribution ($\lambda_1 = \lambda_2 = \lambda_3 = 1/3$).

During simulation of sinus rhythm and atrial flutter, a coherence between the time course of the equivalent dipole $\mathbf{D}_E(t)$ and the VCG was observed. For AF, a number of simulations which were differing in the location of the substrate that initiated AF on the atria, as well as the procedures for initiating AF, were performed. It was found that the VCG during AF was much more complex than during sinus rhythm or atrial flutter, however, it was possible to employ the spatial distribution of the VCG for identifying the location of the atrial substrate in simulations where stable and single AF sources were used. In more complex simulations, such as multiple wavelet reentry, the spatial

distribution became uniformly distributed.

A similar approach to spatial analysis of the atrial activity employing the VCG, synthesized with the inverse Dower matrix, has been proposed and applied to both atrial flutter and AF data [49–51]. During atrial flutter, F waves were isolated from the TQ-interval and averaged, leading to one average F wave representing each recording. During AF, the atrial activity was also extracted from the TQ-intervals, which were artificially prolonged to at least 2 s with the help of pacing. In contrast to atrial flutter, AF analysis was applied separately to each f wave.

Similar to [28], the approach is based on the eigenanalysis of the covariance matrix of the VCG, which, however, was not normalized prior to the analysis. In contrast to mainly evaluating the extracted eigenvalues, the analysis focuses on the three eigenvectors $\mathbf{v}_1$, $\mathbf{v}_2$, and $\mathbf{v}_3$ associated with $\lambda_1 \geq \lambda_2 \geq \lambda_3$. In detail, the spatial analysis aims for obtaining the preferred direction of activation by calculating the plane of best fit, which was defined as the 2-D projection of the VCG that would produce a minimum mean-square error estimate when compared with the original data. This was achieved by letting the eigenvectors $\mathbf{v}_1$ and $\mathbf{v}_2$, which correspond to the directions in which the data exhibits the largest variance, span the plane of fit, resulting in that the perpendicular axis of the plane was defined by the third eigenvector $\mathbf{v}_3$. The orientation of the plane of best fit relative to the frontal plane can then be described in terms of the azimuth and elevation angles of $\mathbf{v}_3$. The azimuth angle ranged from $-180$ to 180 degrees, and was divided into 12 30-degree regions.

For isthmus-dependent atrial flutter, the majority of planes of best fit were found to be consistent with the expected anatomical orientation of the reentrant circuit parallel to the tricuspid valve [49]. For AF, it was found that 15 of 22 ECGs had at least 30% of the planes in a single 30-degree region of azimuth angles, and were thus considered organized [50]. Of these 15 ECGs, 12 had the largest number of planes with azimuth angles within 30 degrees of the sagittal plane. These findings suggested to the authors that there may be a spectrum of complexity of AF organization that can be extracted using vector analysis of AF. Similar results were obtained in a follow-up study with a slightly modified methodology [51], in which it was also found that the stability of the orientation of the vector loops over time was higher in patients without a significant left-to-right atrial frequency gradient.

Though the derived orientation of the planes of best fit gave physiologically reasonable results, especially for the isthmus-dependent atrial flutter, the spatial analysis of atrial loops on the basis of the inverse Dower transform has been questioned [52]. In that study, the Frank orthogonal leads have been used as gold standard, and another transform for synthesizing the VCG [27], especially developed for the P wave, was used for comparison. A difference in the

orientation of the planes of best fit was found between the VCG loops based on the Frank orthogonal leads and on the inverse Dower transform. However, no significant improvement of the estimation was found when using the VCG synthesized such that it was optimized for the analysis of atrial activity. Furthermore, it was noted that the actual fit of the atrial loops to the plane of best fit should be considered in the spatial analysis. This can be accomplished by considering not only the eigenvectors, but also the eigenvalues in the analysis, as proposed in [28, 53].

A different approach to quantifying the extent of intracardiac organization by means of spatial analysis of the ECG was proposed in [54]. In that analysis, the VCG was approximated by employing leads V5, aVF, and V1 as semi-orthogonal X, Y, and Z leads. The method starts by manually choosing the start and end time for a template, e.g., an F wave during atrial flutter, or an f wave during AF, from 10-s recordings. The correlation between the template and the remaining recording is then evaluated at successive time instants $n$ in each lead, resulting in three series of correlation values denoted $r_X(n)$, $r_Y(n)$, and $r_Z(n)$. Similar to the VCG, these correlation series can be plotted in the XY, YZ, and XZ plane, which will appear as more or less clear loops depending on the regularity of the correlation series. The intracardiac activity was considered spatially coherent when the maximum correlation values of $r_X(n)$, $r_Y(n)$, and $r_Z(n)$ simultaneously exceeded a certain threshold for the majority of loops. While isthmus-dependent atrial flutter was found to have a pronounced spatial coherence, nonisthmus-dependent flutter and AF were found to be spatially incoherent.

The authors claimed the analysis of atrial activity, employing the correlation series $r_X(n)$, $r_Y(n)$, and $r_Z(n)$, to be superior to the traditional VCG, as loops constructed directly from the X, Y, and Z leads are dominated by the large ventricular activity. In contrast, the correlation series can be expected to have small values during ventricular activity, due to the poor correlation with the atrial template, while larger correlation values are to be expected during the atrial activity. However, VCG analysis of atrial activity can be improved by, e.g., restricting the analysis to time segments with atrial activity only, or employing QRST cancellation prior to the analysis. This would have the advantage to indeed allow the evaluation of spatial coherence of the atrial activity over time, while strictly viewed, the proposed approach evaluates the spatial similarity to one certain time segment, i.e., the template. As a consequence, the analysis should be highly affected by the choice of the template, especially during AF, where signal morphology can be rather variable.

Besides spatial analysis of the atrial activity based on the VCG, BSPM has also been employed for this purpose. During, e.g., counterclockwise and clockwise typical atrial flutter, the spatial voltage distribution as captured by the

body surface signals has been found to be directly related to the underlying activation sequence, which could be assessed from simultaneously recorded intracardiac signals [19]. Also, during AF, different activation patterns [20] and a varying spatial complexity of the electrical activity recorded with BSPM [55] has been observed, however, in both studies the results could not be compared with the actual mechanisms of AF because of the lack of simultaneous intracardiac recordings. In another approach, high-density BSPM was used to estimate the electrograms on the surface of the heart by deriving the transfer matrix that relates body surface to epicardial potentials [56]. The method has been validated on a few cases of real data recordings, e.g., during atrial flutter.

# Chapter 4

# Signal Processing of Intracardiac Atrial Fibrillation Signals

Although the mechanisms of AF are not yet completely understood, recent progress indicates that future ablation treatment of AF will be tailored to the individual patient in order to achieve optimal success rate [57]. Therefore, methods are required which can improve the understanding of AF mechanisms and accurately guide the ablation catheter to the atrial sites at which the arrhythmia originates or which represent arrhythmia substrates. Methods for propagation pattern analysis are thus of interest as they have the potential to point out ectopic foci or identify reentrant activities.

Methodologically, the challenge of analyzing propagation patterns is to determine the interrelationship between a larger number of signals. In the following, multivariate approaches to propagation pattern analysis both in the time and frequency domain will be discussed. Prior to that, a background will be given on intracardiac AF signal processing as well as on bivariate measures, which quantify the coupling between intracardiac AF signals.

## 4.1 Preprocessing

Narrowband filters are usually employed to remove disturbances like baseline wander and powerline interference. In atrial recordings which are made close to the ventricles, e.g., in the coronary sinus, ventricular far-field effects may

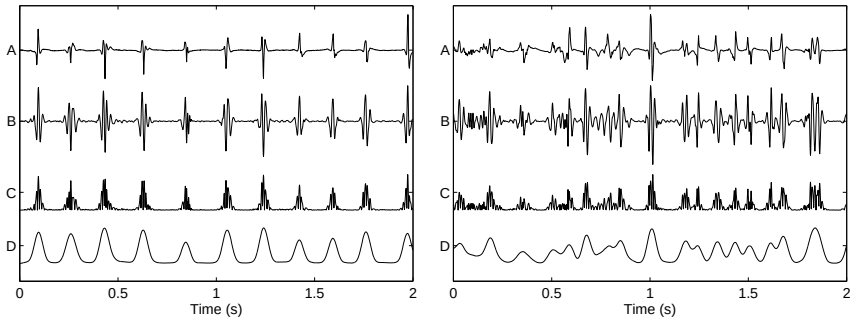


**Figure 4.1:** Illustration of intracardiac signal preprocessing on (a) a well and (b) a less organized electrogram. Both examples show the original electrogram (A), the electrogram after bandpass filtering (B), rectification (C), and lowpass filtering (D).

appear in addition to the local atrial activity. When such effects are detected, a rather simple strategy is to introduce a blanking period of about 90 ms. Another approach is similar to ABS, i.e., a template that reflects the average ventricular activity is subtracted.

## 4.2 Activation detection

The highly varying morphology of intracardiac signals complicates the detection of the atrial activation times, on which many methods for intracardiac signal analysis are based. Thus, a series of signal preprocessing steps, originally proposed for cross-correlation analysis [58], is usually employed prior to activation detection. After bandpass filtering with a bandpass of 40–250 Hz, the signal is rectified and lowpass filtered at 20 Hz. This process extracts a time-varying waveform proportional to the high-frequency components in the original electrogram, see Fig. 4.1. The exact values of the cut-off frequencies as well as the implementation of the filters can vary somewhat from study to study.

For activation detection, a threshold is commonly applied to the preprocessed electrogram $z(n)$. The threshold $\theta_i$ is set at the time instant of the last detected activation, $n_i$, and is held fixed until it is exceeded and a new activation is detected. It can be calculated based on the exponential average of the

peak amplitudes of the previously detected activations [2],

$$\theta_i = \alpha\mu_i, \tag{4.1}$$

$$\mu_i = \mu_{i-1} + \beta(z(n_i) - \mu_{i-1}), \quad i \geq 1, \tag{4.2}$$

where $\mu_i$ is the exponential average, and $z(n_i)$ represents the peak amplitude of the most recently detected activation. The parameter $\beta$ defines the rate with which the threshold can change, and should be chosen to a value between 0 and 1 such that stability is assured. The parameter $\alpha$ is typically chosen in the interval 0.5–0.7 and determines the fraction of $\mu_i$ to be used in the threshold computation. When the preprocessed signal exceeds $\theta_i$, a new activation is detected. The time instant of the first local maximum following the detection serves as an estimate of the activation time.

In another approach, these time instants serve as preliminary estimates of the activation times [59]. In order to arrive at the final estimates, the original electrogram $x(n)$ is processed by rectification and a moving average filter:

$$\tilde{x}(n) = \sum_{i=0}^{N/2-1} |x(n-i)| - \sum_{i=1}^{N/2} |x(n+i)|, \tag{4.3}$$

where $N$ is chosen as the number of samples in a 90-ms interval. The activation times are then estimated as the positive zero crossings in $\tilde{x}(n)$ that are closest to the preliminary activation times. This time instant may be interpreted as the barycenter of each activation waveform, i.e., the time instant that divides the activation waveform into two equal parts of local area. In order to avoid erroneous detection of activation times, zero crossings for which the slope of $\tilde{x}(n)$ does not exceed a fixed threshold are discarded.

In order to prevent multiple detections of a single activation, an eye-closing period in the range of 50 ms is usually introduced after each detected activation. Furthermore, a look-back detection mode based on the mean time difference between the detected activation times can be employed to find activations that have been missed because of a low amplitude [2]. Two examples illustrating activation detection are shown in Fig. 4.2.

Recently, a method based on wavelet decomposition has been proposed for activation detection, particularly in unipolar electrograms [60]. An initial set of activation times is obtained by matching the electrogram with a library of 128 templates. Then, wavelet decomposition is performed in order to decompose the electrogram into a number of "near- and far-field" electrograms, and false-positive detections caused by the far-field electrograms are removed. Following this, multiple detections due to fractionation are identified and removed, and finally, previously removed false-negative detections are added back to the activation time list when the time between two subsequent detected activations

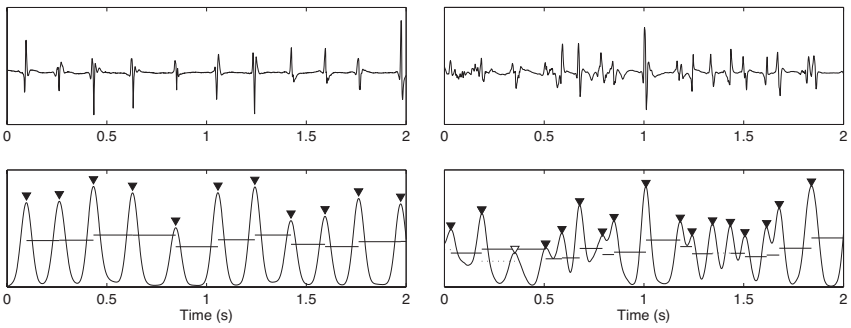


(a) (b)

**Figure 4.2:** Two examples illustrating activation detection. Upper panel: Intracardiac AF signals with (a) regular and (b) irregular activations. Lower panel: Corresponding preprocessed signals with regularly estimated activation times (filled triangle) and activations detected in look-back detection mode (empty triangle). The thresholds are marked with lines, where a dotted line marks a lowered threshold due to look-back detection mode. Activation detection is done according to Eq. (4.2), where $\alpha = 0.55$ in normal and $\alpha = 0.35$ in look-back detection mode, $\beta = 0.6$, and the eye-closing period was set to 50 ms.

is too long. While certain steps in this approach, such as the reliability of template matching, the division into near- and far-field electrograms, as well as the variety of rules to handle false-negative and false-positive detections, may be questionable, this study serves as a good illustration of the common problems faced during activation detection in AF signals. Reliable detection of activation times becomes increasingly difficult with decreasing signal organization, which comes with, e.g., strongly varying signal morphology, multiple deflections, or continuous electrical activity. In order to quantify the reliability of the detected activations, as well as further analysis based on the detected activations, simultaneous analysis of AF organization may be helpful.

## 4.3 Frequency analysis

In recent years, the interest in frequency analysis of intracardiac signals has increased especially since the identification of sites with high dominant frequency (DF) has been proposed for ablation guidance [61]. Though being termed “dominant” frequency, the DF is actually defined as the fundamental

frequency of the power spectrum and does not necessarily correspond to the largest frequency peak. In order to reduce the influence of signal morphology on the analysis and to prevent that, e.g., one of the harmonic frequencies is falsely detected as DF, preprocessing steps similar to those illustrated in Fig. 4.1 should be applied prior to frequency analysis. The effect of the different preprocessing steps on the power spectrum have been discussed in detail in, e.g., [62]. In the same study, it has been shown for simulated signals that the DF is well correlated to the mean atrial cycle length, however, certain deviations were observed when the amplitude and the cycle length of the atrial activations varied over time. However, in another study, the estimation of the the atrial cycle length was found to be more robust when it was based on frequency analysis instead of on atrial activation detection [63].

In clinical studies, frequency analysis has been employed to, e.g., determine the presence of left-to-right frequency gradients. Interestingly, it was found that patients with paroxysmal AF usually have a significant left-to-right frequency gradient, which no longer could be observed after PV ablation, whereas patients with persistent AF have no significant left-to-right frequency gradient neither before nor after PV ablation [64]. In another study, frequency analysis was employed to determine time instants for successful cardioversion [65].

## 4.4 Measures of coupling between intracardiac atrial fibrillation signals

The interest in quantifying AF organization has led to a diversity of measures both in the time and frequency domain. Bivariate measures are of special interest as they, to some extent, can provide information on the spatial organization during AF.

A linear method for measuring the spatial organization in the time domain was presented in [58]. A number of electrograms were simultaneously recorded at equally spaced locations in the RA. After preprocessing, the cross-correlation functions between all possible paired combinations of the signals were evaluated. The degree of linear coupling was estimated as the absolute peak of the cross-correlation function. It was found that the atrial activity remains well-correlated and is independent of the distance between the recording sites during sinus rhythm and atrial flutter. In contrast, the linear coupling was found to decay monotonically with distance during AF, which is most likely due to that the likelihood for two atrial sites to be activated by the same propagation wavefront during AF decreases with increasing distance.

In the frequency domain, the magnitude-squared coherence (MSC) has been employed to quantify the coupling between two signals $x_1(n)$ and $x_2(n)$ in terms

of their phase consistency [66, 67]. The MSC is defined to

$$|C_{12}(f)|^2 = \frac{|S_{12}(f)|^2}{S_1(f)S_2(f)}, \tag{4.4}$$

where $S_{12}(f)$ is the cross-power spectrum, and $S_1(f)$ and $S_2(f)$ are the power spectra of $x_1(n)$ and $x_2(n)$, respectively. In the absence of noise, two linearly related signals will have an MSC equal to one at all frequencies, while two random, uncorrelated signals will have an MSC equal to zero. Also, the presence of noise or non-linear coupling will reduce the MSC for similar signals.

An advantage of the MSC is that it allows to restrict the evaluation of the degree of coupling to that range of frequencies which is relevant for the analysis. In [67], the MSC was proposed for the analysis of the spatial organization during various rhythms, such as sinus rhythm, atrial flutter, and AF. In detail, a large electrode array was employed for epicardial recordings, and an electrode close to the center of the array was chosen as reference. Coherence maps were built by measuring the mean MSC in the 0–50 Hz range between every recording site relative to the reference. Similar to the time domain approach employing cross-correlation [58], strong coupling independent of the distance between the recording sites was found during sinus rhythm and atrial flutter, while for AF, a clear decay of the coupling with distance could be observed. It was also pointed out that, especially during AF, the coherence maps were strongly dependent on the choice of the reference. This reveals one of the disadvantages of the coherence measure, which results from the ability to consider only two signals at a time. Another disadvantage is that because of the symmetry of the cross-spectrum, i.e., $|S_{12}(f)| = |S_{21}(f)|$, the MSC also becomes symmetric, i.e., $|C_{12}(f)|^2 = |C_{21}(f)|^2$. Consequently, the MSC only allows analysis of the strength, but not of the direction of the coupling between $x_1(n)$ and $x_2(n)$.

AF organization has also been quantified by the mean-square error in the linear prediction between two electrograms, $x_1(n)$ and $x_2(n)$ [68]. The method relates the two signals with two linear filters, $H_{2\leftarrow 1}$ and $H_{1\leftarrow 2}$, the former filter linearly predicting $x_2(n)$ from $x_1(n)$ and the latter filter linearly predicting $x_1(n)$ from $x_2(n)$. For both filters, the mean-square prediction error was calculated, and the smaller value was chosen to represent the "overall amount of non-linearity" between the signals. However, while it is true that the presence of non-linear coupling would prevent the prediction error of becoming zero, a non-zero prediction error does not necessarily imply the actual presence of non-linear coupling. Similar to the previously discussed linear methods based on the cross-correlation function and the MSC, the usage of a linear prediction method should first and foremost be able to provide a measure of linearity, and thus conclusions about the degree of non-linearity must be drawn carefully. Nevertheless, the derived measure was found to distinguish between fibrillatory

and non-fibrillatory rhythms, as well as between different levels of organization during AF. Again, the strength of the coupling was seen to decrease with increasing distance between the recording sites. Potentially, the direction of the coupling could be estimated to the direction in which the smaller prediction error occurs. Furthermore, the estimated transfer function could be used for estimation of the time delay.

Measures which indeed quantify the degree of non-linear coupling between two atrial sites were developed based on a multivariate embedding procedure [69]. The approach assumes that the underlying non-linear dynamics of a system, both in time and space, can be reconstructed by taking $m$ measured points in a segment of the observed time series $x(t)$ as state variables. Starting by taking a sample $x(t_i)$ and then choosing another $m-1$ samples, each separated by a so-called embedding delay $\tau$, a delay vector can be constructed as

$$\mathbf{x}(t_i) = \{x(t_i - (m-1)\tau), \cdots, x(t_i - 2\tau), x(t_i - \tau), x(t_i)\}, \tag{4.5}$$

where $\tau$ is chosen as a multiple of the sampling period. This vector represents the state of the system at time $t_i$, and is also referred to as a point in the phase space with embedding dimension $m$. An illustration of the underlying dynamics of the time series can be achieved by plotting two delay vectors $\mathbf{x}(t_i - \tau)$ and $\mathbf{x}(t_i)$ against each other in a so-called phase plot. While trajectories of sinus rhythm show a cross-like structure in the phase plot, trajectories of AF show a more complex structure, referred to as chaotic dynamics [70]. In order to characterize such dynamics, the correlation integral has been introduced and can be estimated according to the Grassberger–Procaccia method,

$$C_m(\mathbf{x}, \epsilon) = \frac{1}{N} \sum_{i=1}^{N} \sum_{j=i+W}^{N} u(\epsilon - |\mathbf{x}(t_i) - \mathbf{x}(t_j)|), \tag{4.6}$$

where $N$ is the number of employed delay vectors and $u(\eta)$ is the unit step function defined as 0 for $\eta \leq 0$ and 1 for $\eta > 0$. The correlation integral can be interpreted as the average number of points $\mathbf{x}(t_j)$ in the phase space which are separated by a shorter distance than $\epsilon$ from a reference point $\mathbf{x}(t_i)$. The offset value $W$ is based on the autocorrelation of $x(t)$ chosen such that spurious correlation is avoided. The correlation integral can then be employed to define the correlation dimension,

$$C_{D,m}(\mathbf{x}, \epsilon) = \frac{\mathrm{d} \log C_m(\mathbf{x}, \epsilon)}{\mathrm{d} \log \epsilon}, \tag{4.7}$$

as well as the correlation entropy,

$$C_{E,m}(\mathbf{x}, \epsilon) = \frac{1}{\tau} \ln \frac{C_m(\mathbf{x}, \epsilon)}{C_{m+1}(\mathbf{x}, \epsilon)}. \tag{4.8}$$

The correlation dimension estimates the average number of similar points in the phase space when the maximally allowed distance $\epsilon$ for two points to be similar goes to zero. The correlation entropy can be interpreted as a measure of how fast the average number of similar points in the phase space for a certain distance $\epsilon$ decreases with increasing embedding dimension $m$. Thus, correlation dimension and correlation entropy can be interpreted as measures of geometrical and dynamical complexity, respectively.

In order to evaluate the non-linear coupling between two electrograms $x_1(t)$ and $x_2(t)$, the delay vectors $\mathbf{x}_1(t_i)$ and $\mathbf{x}_2(t_i)$ of the two separate systems as well as the delay vectors $\mathbf{q}(t_i)$ of the joint system were defined, where

$$\begin{aligned}\mathbf{q}(t_i) = \{&x_1(t_i-(m-1)\tau),\cdots,x_1(t_i-2\tau),x_1(t_i-\tau),x_1(t_i),\\ &x_2(t_i-(m-1)\tau),\cdots,x_2(t_i-2\tau),x_2(t_i-\tau),x_2(t_i)\},\end{aligned} \tag{4.9}$$

i.e., the joint system has the embedding dimension $2m$. The measures independence of complexity, $I_C$, and independence of predictability, $I_P$, were then estimated as

$$I_C = \frac{|C_{D,m}(\mathbf{q},\epsilon) - C_{D,m}(\mathbf{x}_1,\epsilon)| + |C_{D,m}(\mathbf{q},\epsilon) - C_{D,m}(\mathbf{x}_2,\epsilon)|}{C_{D,m}(\mathbf{x}_1,\epsilon) + C_{D,m}(\mathbf{x}_2,\epsilon)}, \tag{4.10}$$

and

$$I_P = \frac{|C_{E,m}(\mathbf{q},\epsilon) - C_{E,m}(\mathbf{x}_1,\epsilon)| + |C_{E,m}(\mathbf{q},\epsilon) - C_{E,m}(\mathbf{x}_2,\epsilon)|}{C_{E,m}(\mathbf{x}_1,\epsilon) + C_{E,m}(\mathbf{x}_2,\epsilon)}. \tag{4.11}$$

Both indices vary between 0 and 1, where 0 refers to completely coupled systems and 1 refers to independent systems. The degree of non-linear coupling was found to decrease with AF organization, and the results for the measures $I_C$ and $I_P$ were rather similar.

A similar non-linear coupling measure, based on the concept of Granger causality, has been proposed in [71]. Granger causality, originally employed in econometrics [72], is based on the simple idea that a cause cannot come after the effect. Thus, if $x_1(t)$ affects $x_2(t)$, knowledge about past and present values of $x_1(t)$ should improve the prediction of $x_2(t)$. In order to measure non-linear Granger causality from $x_1(t)$ to $x_2(t)$, the test statistic

$$Q = I(\mathbf{q}, x_2(t_{i+1})) - I(\mathbf{x}_2, x_2(t_{i+1})) \tag{4.12}$$

was employed, where $I(\mathbf{q}, x_2(t_{i+1}))$ is the generalized mutual information about $x_2(t_{i+1})$ contained in the delay vectors $\mathbf{x}_1(t_i)$ and $\mathbf{x}_2(t_i)$ jointly,

$$I(\mathbf{q}, x_2(t_{i+1})) = \ln C_m(\{\mathbf{q}, x_2(t_{i+1})\},\epsilon) - \ln C_m(\mathbf{q},\epsilon) - \ln C_m(x_2(t_{i+1}),\epsilon), \tag{4.13}$$

and $I(\mathbf{x}_2, x_2(t_{i+1}))$ is the generalized mutual information about $x_2(t_{i+1})$ contained in delay vector $\mathbf{x}_2(t_i)$ only,

$$I(\mathbf{x}_2, x_2(t_{i+1})) = \ln C_m(\{\mathbf{x}_2, x_2(t_{i+1})\}, \epsilon) - \ln C_m(\mathbf{x}_2, \epsilon) - \ln C_m(x_2(t_{i+1}), \epsilon). \tag{4.14}$$

With these definitions, the test statistic $Q$ becomes zero when $x_1(n)$ does not Granger cause $x_2(n)$, as then the past and present values of $x_1(n)$ do not contain extra information on the future values of $x_2(n)$ and thus

$$I(\mathbf{q}, x_2(t_{i+1})) = I(\mathbf{x}_2, x_2(t_{i+1})). \tag{4.15}$$

In contrast, when $x_1(n)$ does Granger cause $x_2(n)$, the test statistic $Q$ takes a value larger than zero. The method was illustrated by characterizing changes in the spatiotemporal activation pattern during pharmacological conversion of AF in goats.

Coupling in pairs of electrograms has also been quantified using methods based on the detected activation times. A measure of synchronization between pairs of closely spaced atrial sites was proposed in [73]. The electrograms were preprocessed and their activation times were detected as previously described. Each detected activation from the first atrial site was paired to the closest activation from the second atrial site within a $\pm 1$ s window. Two atrial sites were defined as synchronized if the delays between the detected activation pairs were lower than, or equal to, the maximum time required for a propagation wavefront to cover the distance between them, and if the temporal structure of the delays over a certain period was statistically different from a random phenomenon. The former requirement implies assumptions about both the conduction velocity of the electrical impulse in the atrial tissue and the distance between the two evaluated atrial sites, which may be a limitation of this method. The experimental results showed a gradual decrease in synchronization from sinus rhythm to atrial flutter and further to AF.

In a related approach, activation pairs from two adjacent atrial sites were detected in a similar fashion, and the absolute value of the time delay between each activation pair was calculated [74]. A histogram of the delays was constructed, and a measure of Shannon entropy was defined in order to quantitatively describe the distributions. The results showed a significant decrease of the synchronization with AF organization. By applying the method on recordings from a basket catheter in the RA, a spatial heterogeneity in the level of synchronization could be observed.

## 4.5 Propagation pattern analysis based on activation times

Early studies on the propagation of the electrical activity during AF have mostly been based on high-density epicardial mapping, in which large arrays of electrodes, placed regularly in rows and columns, have been used [75, 76]. A common strategy has been to detect the activations, manually group the detected activations into wavefronts, and analyze the corresponding propagation patterns based on the drawings of subsequent activation maps, in which the isochrone lines have been marked. In this way, qualitative conclusions about the propagation pattern and its changes over time can been drawn. In addition to the activation maps, Konings et al. proposed to compute a conduction velocity map from the local activation times of four neighboring electrodes [75], chosen such that the electrodes would be placed at the corners of a square. This idea was developed further by Holm et al. [76], who employed the local activation times of four neighboring electrodes to compute direction vectors. Besides using the direction vectors to improve the conduction velocity estimates, preferable activation patterns could be determined by time averaging of the direction vectors for each set of four neighboring electrodes.

Unfortunately, the above approaches are difficult to apply to endocardial recordings, as the number of electrodes on endocardial catheters is often limited. Also, the recording sites are seldom placed uniformly in rows and columns, which makes propagation pattern analysis even more challenging. One approach dealing with the latter difficulty is based on estimation of the direction and velocity of propagation using vector field analysis [77, 78]. The underlying idea can be compared to the approach by Holm et al. [76], however, by employing an interpolation procedure, the method becomes less dependent on catheter geometry, and has the additional advantage of being based on an analytical derivation of the velocity vector field and its divergence. In detail, the activations in each of the $N$ electrograms are detected, and all activations belonging to the same activation wavefront are grouped together. As each activation wavefront is analyzed separately, the activation times from the $N$ different recording sites are in the following denoted independently of the activation wavefront by $t_i$, $i = 1, \ldots, N$. Furthermore, the positions of the recording sites in the 2-D space are specified by the coordinates $(x_i, y_i)$, $i = 1, \ldots, N$. Now, a surface $T(x, y)$, describing activation time as a function of position $(x, y)$, can be fitted to the points $T(x_i, y_i) = t_i$ with, e.g., radial basis functions. On this surface, lines with identical activation times mark local isochrones. The

gradient vector

$$\nabla T = \begin{bmatrix} \frac{\partial T}{\partial x} \\ \frac{\partial T}{\partial y} \end{bmatrix} = \begin{bmatrix} T_x \\ T_y \end{bmatrix} \tag{4.16}$$

is always normal to the local isochrone and, thus, defines the direction of propagation. The velocity vector can then be found as

$$\mathbf{v} = \begin{bmatrix} v_x \\ v_y \end{bmatrix} = \begin{bmatrix} \frac{dx}{dT} \\ \frac{dy}{dT} \end{bmatrix} = \begin{bmatrix} \frac{T_x}{T_x^2 + T_y^2} \\ \frac{T_y}{T_x^2 + T_y^2} \end{bmatrix}. \tag{4.17}$$

For further analysis, the divergence of the vector field is calculated,

$$\nabla \cdot \mathbf{v} = \frac{\partial v_x}{\partial x} + \frac{\partial v_y}{\partial y}. \tag{4.18}$$

The divergence is a signed scalar, which attains positive values in presence of a source and negative values in presence of a sink in the vector field. In simulations, divergence analysis could correctly identify, e.g., ectopic foci as sources and wavefront collisions as sinks of the vector field [78].

Another approach to propagation pattern analysis has been proposed specifically for recordings from circular mapping catheters, which are sometimes used during EP studies and ablations [79]. As in the previous study, each activation wavefront is analyzed separately, and thus the activation times from the $N$ different recording sites are again denoted independently of the activation wavefront by $t_i$, $i = 1, \ldots, N$. Furthermore, due to the circular nature of the catheter, the positions of the recording sites are described by angles $\phi_i$ in the range $[0, 2\pi)$. Assuming that a plane activation wavefront travels across the catheter, a cosine function can be fitted to the activation pattern in the $N$ recorded electrograms,

$$t_i = t_o - A\cos(\phi_i - \phi_0), \quad i = 1, \ldots, N, \tag{4.19}$$

where $t_o$ is the time offset of the activation wavefront relative to the beginning of the recording, $A$ is a parameter related to how fast the activation wavefront crosses the catheter, and $\phi_0$ describes the angle at which the earliest activation occurs. From the estimate of $\phi_0$, it is possible to draw conclusions about the direction of the activation wavefront, and the cosine amplitude $A$ can be employed together with an estimate of the catheter radius $r$ to estimate the conduction velocity to $r/A$. The method correctly identified the direction of

activation wavefronts in simulations as well as in real data recordings during sinus rhythm and pacing. A disadvantage of the method is that it can only be employed when the propagation is organized, i.e., the recordings must first be scanned for complete and plane activation wavefronts passing the catheter.

## 4.6 Propagation pattern analysis based on the information flow in multivariate systems

The dependence on the detected activation times is a disadvantage since low AF organization and high complexity of the propagation patterns make it difficult to detect the activation times and decide which of these activations should be assigned to the same activation wavefront. Thus, it is of interest to also explore the propagation patterns during AF in the frequency domain.

One possibility is to employ frequency domain measures of Granger causality, which have been used to analyze the information flow in multivariate systems. In a linear framework, this concept is closely connected to multivariate autoregressive (MVAR) modeling. In the following, details on MVAR modeling, measuring causality in the time and frequency domain, as well as significance testing of the derived measures are provided.

### 4.6.1 MVAR modeling

Each set of $N$ simultaneous observations $\mathbf{x}(n) = \begin{bmatrix} x_1(n) & \cdots & x_N(n) \end{bmatrix}^T$, $n = 1, \ldots, T$, is assumed to be adequately represented by an MVAR model of order $m$

$$\mathbf{x}(n) = \sum_{k=1}^{m} \mathbf{A}_k \mathbf{x}(n-k) + \mathbf{w}(n), \tag{4.20}$$

where each $\mathbf{A}_k$ is an $N \times N$ matrix comprising the AR coefficients $a_{ij}(k)$, $i, j = 1, \ldots, N$, and $\mathbf{w}(n) = \begin{bmatrix} w_1(n) & \cdots & w_N(n) \end{bmatrix}^T$ is a multivariate Gaussian noise process $\sim \mathcal{N}(\mathbf{0}, \mathbf{\Sigma}_w)$.

In practice, the model order $m$ is typically unknown, and thus both the MVAR coefficients and the optimal model order must be estimated. In addition, it is also important to check the adequacy of the model assumptions.

#### MVAR model estimation

For the estimation of the MVAR coefficients, it is convenient to rewrite Eq. (4.20) in matrix form

$$\mathbf{X} = \mathbf{Y}\mathbf{B} + \mathbf{W}, \tag{4.21}$$

where

$$\begin{aligned}
\mathbf{X} &= \begin{bmatrix}\mathbf{x}(1) & \mathbf{x}(2) & \cdots & \mathbf{x}(T)\end{bmatrix}^T = \begin{bmatrix}\mathbf{x}_1 & \mathbf{x}_2 & \cdots & \mathbf{x}_N\end{bmatrix}, \\
\mathbf{W} &= \begin{bmatrix}\mathbf{w}(1) & \mathbf{w}(2) & \cdots & \mathbf{w}(T)\end{bmatrix}^T, \\
\mathbf{B} &= \begin{bmatrix}\mathbf{A}_1 & \mathbf{A}_2 & \cdots & \mathbf{A}_m\end{bmatrix}^T = \begin{bmatrix}\boldsymbol{\beta}_1 & \boldsymbol{\beta}_2 & \cdots & \boldsymbol{\beta}_N\end{bmatrix}, \\
\mathbf{y}(n) &= \begin{bmatrix}\mathbf{x}(n) \\ \mathbf{x}(n-1) \\ \vdots \\ \mathbf{x}(n-m+1)\end{bmatrix}, \\
\mathbf{Y} &= \begin{bmatrix}\mathbf{y}(1) & \mathbf{y}(2) & \cdots & \mathbf{y}(T)\end{bmatrix}^T.
\end{aligned}$$

The least-squares (LS) solution for the MVAR coefficients then becomes [80]

$$\tilde{\mathbf{B}} = \arg\min_{\mathbf{B}} ||\mathbf{X} - \mathbf{Y}\mathbf{B}||^2 \tag{4.22}$$

$$= (\mathbf{Y}^T\mathbf{Y})^{-1}\mathbf{Y}^T\mathbf{X}, \tag{4.23}$$

where $||\cdot||$ denotes the $L_2$ norm. The MVAR coefficients contained in column $\boldsymbol{\beta}_i$ of matrix $\mathbf{B}$, which are responsible for predicting $x_i(n)$, can also be estimated separately,

$$\tilde{\boldsymbol{\beta}}_i = \arg\min_{\boldsymbol{\beta}_i} ||\mathbf{x}_i - \mathbf{Y}\boldsymbol{\beta}_i||^2, \tag{4.24}$$

and thus index $i$ can in the following be omitted for simplicity.

A common problem in LS estimation is the overfitting of the solution, especially when the ratio of available time samples and unknown parameters, $T/mN$, becomes small. In order to avoid overfitting, constraints which restrict the space of possible solutions can be put on Eq. (4.24). In ridge regression, the constraint is defined to the $L_2$ norm of the coefficients, i.e., the optimization problem becomes

$$\hat{\boldsymbol{\beta}} = \arg\min_{\boldsymbol{\beta}} ||\mathbf{x} - \mathbf{Y}\boldsymbol{\beta}||^2 \quad \text{subject to} \quad ||\boldsymbol{\beta}||^2 \leq t, \tag{4.25}$$

where $t \geq 0$ is the upper bound of the constraint. Other constraints are based on the $L_1$ norm and typically variants of the least absolute selection and shrinkage operator (LASSO) [81], which is defined to

$$\hat{\boldsymbol{\beta}} = \arg\min_{\boldsymbol{\beta}} ||\mathbf{x} - \mathbf{Y}\boldsymbol{\beta}||^2 \quad \text{subject to} \quad ||\boldsymbol{\beta}||_1 \leq t. \tag{4.26}$$

In another LASSO variant, termed the adaptive group LASSO, the coefficients in $\boldsymbol{\beta}$ are divided into $L$ non-overlapping groups $\boldsymbol{\beta}_l$, $l = 1, \ldots, L$, [82], yielding

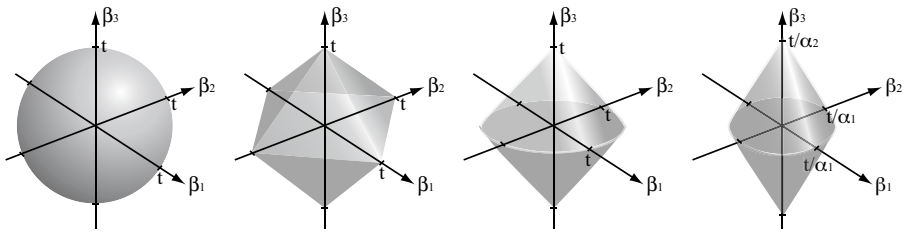


**Figure 4.3:** Space of possible solutions in a regression problem with $\boldsymbol{\beta} = \begin{bmatrix}\beta_1 & \beta_2 & \beta_3\end{bmatrix}$ for (a) ridge regression, (b) LASSO, (c) group LASSO, and (d) adaptive group LASSO, both with the two groups $[\beta_1, \beta_2]$ and $\beta_3$.

the optimization problem

$$\hat{\boldsymbol{\beta}} = \arg\min_{\boldsymbol{\beta}} ||\mathbf{x} - \sum_{l=1}^{L} \mathbf{Y}_l \boldsymbol{\beta}_l||^2 \quad \text{subject to} \quad \sum_{l=1}^{L} \alpha_l ||\boldsymbol{\beta}_l|| \leq t, \tag{4.27}$$

where $\mathbf{Y}_l$ consists of those columns of matrix $\mathbf{Y}$ that correspond to the coefficients contained in $\boldsymbol{\beta}_l$, and $\alpha_l$ are positive weighting factors. The adaptive group LASSO is in fact the most general LASSO variant, which simplifies to the ordinary group LASSO [83] when all weighting factors are identical, and further to the ordinary LASSO when each unknown parameter is assigned to a group of its own. Also the adaptive LASSO [84], with each unknown parameter in a group of its own but with different weighting factors, can be derived from Eq. (4.27).

Variants of the LASSO have become specifically popular, since they in addition to avoid overfitting also yield sparse solutions. This is illustrated in Fig. 4.3, where the space of possible solutions for different constraints is shown for an example regression problem with three unknowns, i.e., $\boldsymbol{\beta} = \begin{bmatrix}\beta_1 & \beta_2 & \beta_3\end{bmatrix}$. From Fig. 4.3(a) it becomes clear how the $L_2$ norm in ridge regression avoids overfitting, while it does not encourage sparse solutions in which at least one parameter in $\boldsymbol{\beta}$ is estimated to exactly zero. This is in contrast to regression with the LASSO, where sparse solutions are encouraged by the singularities in the constraint, see Fig. 4.3(b). Similarly, when building the two groups $[\beta_1, \beta_2]$ and $\beta_3$, the singularities in the constraint of the group LASSO will encourage sparsity between the groups, as illustrated in Fig. 4.3(c). Finally, when choosing differently large weighting factors $\alpha_1$ and $\alpha_2$ for the two groups in the adaptive group LASSO, different amounts of shrinkage can be put onto different groups, see Fig. 4.3(d).

While a closed form solution can be derived for ridge regression, this is

not possible for the LASSO because of the constraint's singularities. A large number of algorithms, such as least angle regression selection (LARS) [85], have been derived to solve the optimization problem for the LASSO variants. When applying the (adaptive) group LASSO to the estimation of MVAR coefficients, preferably all coefficients modeling the coupling from one recording site to another should be grouped together, such that they can only be pruned jointly.

### Model order selection

Model order selection is a bias versus variance trade-off, i.e., models with too few parameters can be biased, while models with too many parameters can lead to the identification of spurious effects [86]. There are different approaches to model order selection, e.g., information-theoretic selection and Bayesian model selection, represented by the Akaike information criterion (AIC) [87] and the Bayesian information criterion (BIC) [88], respectively,

$$AIC(m) = \ln(|\mathbf{\Sigma}_w|) + 2\frac{mN^2}{T} \tag{4.28}$$

$$BIC(m) = \ln(|\mathbf{\Sigma}_w|) + \ln(T)\frac{mN^2}{T}. \tag{4.29}$$

The optimal model order is the one for which the chosen criterion reaches its minimum.

However, in real applications it may happen that these criteria do not reach a distinct minimum, but have a steep decrease up to some model order $\tilde{m}$, above which the decrease flattens markedly. In that case, model order $\tilde{m}$ is likely to be a better choice than the higher model orders, but as the selection criterion does not reach a minimum, some additional criteria may have to be specified.

### Model checking

A range of diagnostic tests are available in order to check whether an MVAR model adequately represents the observations $\mathbf{x}(n)$. The whiteness of the residuals up to lag $h$ can be checked with the Portmanteau test for autocorrelation [80], which is designed for testing the null hypothesis

$$\mathcal{H}_0 : E(\hat{\mathbf{w}}(n)\hat{\mathbf{w}}(n-i)^T) = 0 \quad i = 1, \ldots, h > m \tag{4.30}$$

against the alternative that at least one autocovariance and, hence, one autocorrelation is nonzero. The Portmanteau test statistic has the form

$$Q_h = T\sum_{i=1}^{h} \mathrm{tr}(\hat{\mathbf{C}}_i^T \hat{\mathbf{C}}_0^{-1} \hat{\mathbf{C}}_i \hat{\mathbf{C}}_0^{-1}), \tag{4.31}$$

where the covariance matrices of the residuals, $\hat{\mathbf{C}}_i$, are defined as

$$\hat{\mathbf{C}}_i = \frac{1}{T} \sum_{t=i+1}^{T} \hat{\mathbf{w}}(t)\hat{\mathbf{w}}(t-i)^T. \tag{4.32}$$

For large samples $T$ and for large $h$, $\bar{Q}_h$ has under $\mathcal{H}_0$ an approximate asymptotic $\chi^2$-distribution. In order to compensate for smaller sample sizes, a modified Portmanteau test statistic has been proposed,

$$\tilde{Q}_h = T^2 \sum_{i=1}^{h} \frac{1}{T-i} \mathrm{tr}(\hat{C}_i^T \hat{C}_0^{-1} \hat{C}_i \hat{C}_0^{-1}). \tag{4.33}$$

Other model checking procedures include tests for nonnormality and structural changes, as well as instantaneous effects [80].

### 4.6.2 Measuring causality in the time domain

Granger defined the observation $x_1(n)$ to be causal for observation $x_2(n)$ if the former helps to improve the prediction of the latter [72], or, equivalently, $x_1(n)$ is not causal for $x_2(n)$ if removing the past samples of $x_1(n)$ from the set of prediction variables for $x_2(n)$ does not change the prediction. For a bivariate MVAR model, i.e.,

$$\begin{bmatrix} x_1(n) \\ x_2(n) \end{bmatrix} = \sum_{k=1}^{m} \begin{bmatrix} a_{11}(k) & a_{12}(k) \\ a_{21}(k) & a_{22}(k) \end{bmatrix} \begin{bmatrix} x_1(n-k) \\ x_2(n-k) \end{bmatrix} + \begin{bmatrix} w_1(n) \\ w_2(n) \end{bmatrix}, \tag{4.34}$$

it can easily be shown that $x_1(n)$ does not Granger-cause $x_2(n)$ if and only if

$$a_{21}(k) = 0, \quad k = 1, \ldots, m. \tag{4.35}$$

As many problems consist of more than two observations, extensions of the definition of Granger causality to the multivariate case are desirable. One possibility is to directly apply the definition for the bivariate case from Eq. (4.35) to the multivariate case, i.e., $x_j(n)$ does not Granger cause $x_i(n)$ if and only if

$$a_{ij}(k) = 0, \quad k = 1, \ldots, m. \tag{4.36}$$

However, in the multivariate case, past samples of $x_j(n)$ may still be helpful to predict $x_i(n)$ more than two steps ahead, as $x_j(n)$ may have an impact on a third observations $x_l(n)$, which in turn may affect $x_i(n)$. Because of the possibility of such indirect causal paths, Eq. (4.36) defines only the absence of direct Granger causality from $x_j(n)$ to $x_i(n)$. Tests for the absence of both

direct and indirect Granger causality result in more complicated non-linear restrictions for the MVAR coefficients [89].

Another concept related to Granger causality is that of instantaneous causality, which can be defined such that $x_1(n)$ instantaneously causes $x_2(n)$ if knowledge about $x_1(n)$ on the time instant which is to be predicted helps to improve the prediction of $x_2(n)$ [89]. For a bivariate MVAR model, it can be shown that instantaneous causality results in a correlation between the residuals, i.e., $x_1(n)$ is not instantaneously causing $x_2(n)$ if and only if $w_1(n)$ and $w_2(n)$ are uncorrelated. However, because of the symmetry of correlation, additional information is needed to draw conclusions about the direction of the instantaneous causality when a correlation between $w_1(n)$ and $w_2(n)$ is present. Also in the multivariate case, instantaneous causality between two observations will be indicated through a correlation between the corresponding residuals.

### 4.6.3 Measuring causality in the frequency domain

While it is possible to test for Granger causality in the time domain by applying statistical tests directly on the MVAR coefficients, many biomedical signals are characterized in terms of their frequency properties. In brain signal analysis, for example, the frequency bands of the alpha, beta, and gamma rhythm are of special interest. During AF, information on the rhythm can be found in the range of the DF. Thus, a frequency domain description of Granger causality is desirable. The Fourier transform (FT) of Eq. (4.20) leads to

$$\mathbf{X}(f) = \sum_{k=1}^{m} \mathbf{A}_k \mathbf{X}(f) e^{-j2\pi fk} + \mathbf{W}(f) \tag{4.37}$$

$$= \left( \mathbf{I}_{N\times N} - \sum_{k=1}^{m} \mathbf{A}_k e^{-j2\pi fk} \right)^{-1} \mathbf{W}(f). \tag{4.38}$$

Defining

$$\bar{\mathbf{A}}(f) = \mathbf{I}_{N\times N} - \mathbf{A}(f) \tag{4.39}$$

with

$$\mathbf{A}(f) = \sum_{k=1}^{m} \mathbf{A}_k e^{-j2\pi fk}, \tag{4.40}$$

Eq. (4.38) becomes

$$\mathbf{X}(f) = \bar{\mathbf{A}}^{-1}(f)\mathbf{W}(f) = \mathbf{H}(f)\mathbf{W}(f), \tag{4.41}$$

where $\mathbf{H}(f)$ is the transfer matrix with elements $H_{ij}(f)$ and $\bar{\mathbf{A}}(f)$ consists of the elements $\bar{A}_{ij}(f)$. These two matrices play a central role in the definition of causality measures in the frequency domain, as is shown in the following.

**Directed transfer function (DTF) and directed coherence (DC)**

The power spectral density matrix becomes

$$\mathbf{S}(f) = |\mathbf{X}(f)|^2 = \mathbf{H}(f)\mathbf{\Sigma}_w\mathbf{H}^H(f), \tag{4.42}$$

where the superscript $H$ stands for the Hermitian transpose. The autospectra can be found on the diagonal and are defined as

$$S_{ii}(f) = \sum_{j=1}^{N} H_{ij}(f) \left( \sigma_{jj}^2 H_{ij}^*(f) + \sum_{\substack{k=1 \\ k\neq i}}^{N} \sigma_{jk} H_{ik}^*(f) \right). \tag{4.43}$$

Assuming that $\mathbf{w}(n)$ is a multivariate white noise process, i.e., $\mathbf{\Sigma}_w$ is diagonal ($\sigma_{jk} = 0$ for $j \neq k$), Eq. (4.43) simplifies to

$$S_{ii}(f) = \sum_{j=1}^{N} \sigma_{jj}^2 |H_{ij}(f)|^2, \quad \text{i.e.,} \tag{4.44}$$

$$1 = \sum_{j=1}^{N} \frac{\sigma_{jj}^2 |H_{ij}(f)|^2}{S_{ii}(f)} = \sum_{j=1}^{N} |\gamma_{i\leftarrow j}(f)|^2 \tag{4.45}$$

with

$$\gamma_{i\leftarrow j}(f) = \frac{\sigma_{jj} H_{ij}(f)}{\sqrt{S_{ii}(f)}} = \frac{\sigma_{jj} H_{ij}(f)}{\sqrt{\sum_{k=1}^{N} \sigma_{kk}^2 |H_{ik}(f)|^2}} \tag{4.46}$$

being the definition of the DC from $x_j(n)$ to $x_i(n)$ [90]. As can be seen from Eqs. (4.44) and (4.45), the DC is derived from a decomposition of the power spectrum $S_{ii}(f)$, and is normalized such that the magnitude-squared DC $|\gamma_{i\leftarrow j}(f)|^2$ expresses the fraction of $S_{ii}(f)$ due to $x_j(n)$, i.e., the normalization is with respect to the destination.

Interestingly, it has been shown that the ordinary coherence $C_{ij}(f)$, see Eq. (4.4), can be expressed as

$$C_{ij}(f) = \boldsymbol{\gamma}_i^H(f)\boldsymbol{\gamma}_j(f), \tag{4.47}$$

where $\boldsymbol{\gamma}_i(f) = \begin{bmatrix} \gamma_{i\leftarrow 1}(f) & \dots & \gamma_{i\leftarrow N}(f) \end{bmatrix}^T$, i.e., the DC can also be derived as a decomposition of the ordinary coherence into a "feedforward" and a "feedback-

ward" part [91]. As with the ordinary coherence, most often the magnitude-square of the DC is of interest for interpretation, i.e.,

$$|\gamma_{i\leftarrow j}(f)|^2 = \frac{\sigma_{jj}^2 |H_{ij}(f)|^2}{\sum_{k=1}^{N} \sigma_{kk}^2 |H_{ik}(f)|^2}. \tag{4.48}$$

By adding the additional restriction that all $\sigma_{jj}^2$ are set to 1, i.e., that $\mathbf{\Sigma}_w$ becomes the identity matrix, Eq. (4.46) leads to the definition of the DTF from $x_j(n)$ to $x_i(n)$ [92]:

$$\tilde{\gamma}_{i\leftarrow j}(f) = \frac{H_{ij}(f)}{\sqrt{\sum_{k=1}^{N} |H_{ik}(f)|^2}}. \tag{4.49}$$

which is normalized similar to the DC,

$$\sum_{j=1}^{N} |\tilde{\gamma}_{i\leftarrow j}(f)|^2 = 1. \tag{4.50}$$

As the DTF can be seen as a simplification of the DC, all the following comments are valid for both measures, although the DTF may not be mentioned explicitly.

The exact relationship between Granger causality and the DC is still a subject for discussion. Only in the bivariate case it can be shown that, e.g., the DC $\gamma_{2\leftarrow 1}(f)$ vanishes for all frequencies if and only if $x_1(n)$ does not Granger cause $x_2(n)$, as

$$\mathbf{H}(f) = \frac{1}{\det \bar{\mathbf{A}}(f)} \begin{bmatrix} \bar{A}_{22}(f) & -\bar{A}_{12}(f) \\ -\bar{A}_{21}(f) & \bar{A}_{11}(f) \end{bmatrix} \tag{4.51}$$

and $\bar{A}_{21}(f) = 0$ for all $f$ if and only if $a_{21}(k) = 0$ for all $k$. However, in the multivariate case ($N > 2$), it is not possible to draw similar conclusions. For illustration purposes, consider the case $N = 4$ with the simple propagation S1 $\rightarrow$ S2 $\rightarrow$ S3 $\rightarrow$ S4, see Fig. 4.4(a). In that case, $\bar{\mathbf{A}}(f)$ takes the form of a bidiagonal matrix

$$\bar{\mathbf{A}}(f) = \begin{bmatrix} \bar{A}_{11} & 0 & 0 & 0 \\ \bar{A}_{21} & \bar{A}_{22} & 0 & 0 \\ 0 & \bar{A}_{32} & \bar{A}_{33} & 0 \\ 0 & 0 & \bar{A}_{43} & \bar{A}_{44} \end{bmatrix} (f), \tag{4.52}$$

which can be shown to have the following lower triangular matrix as inverse

$$\bar{\mathbf{H}}(f) = \begin{bmatrix} \bar{A}_{11} & 0 & 0 & 0 \\ -\bar{A}_{21} & \bar{A}_{22} & 0 & 0 \\ \bar{A}_{21}\bar{A}_{32} & -\bar{A}_{32} & \bar{A}_{22} & 0 \\ -\bar{A}_{21}\bar{A}_{32}\bar{A}_{43} & \bar{A}_{32}\bar{A}_{43} & -\bar{A}_{43} & \bar{A}_{44} \end{bmatrix} (f). \tag{4.53}$$

Obviously, the presence and strength of direct Granger causality from S1 → S2, S2 → S3, and S3 → S4 is correctly reflected by the transfer matrix, as $|H_{21}(f)| = |\bar{A}_{21}(f)|$, $|H_{32}(f)| = |\bar{A}_{32}(f)|$, and $|H_{43}(f)| = |\bar{A}_{43}(f)|$. However, the absence of direct Granger causality from, e.g., S1 → S4, does not show in the transfer matrix, where $|H_{41}(f)|$ becomes a multiplication of the elements of $\bar{\mathbf{A}}(f)$ on the causal path S1 → S2 → S3 → S4. Similar observations can be made for $|H_{31}(f)|$ as well as $|H_{42}(f)|$. Because of the multiplications of elements of $\bar{\mathbf{A}}(f)$ along the causal paths, the indirect couplings will in fact dominate the couplings as detected by the DC. This is in the following illustrated in an example with an MVAR model of dimension $N = 4$ and order $m = 2$, and with causal coupling S1 → S2 → S3 → S4, adapted from [91],

$$\begin{aligned} x_1(n) &= 0.95\sqrt{2}x_1(n-1) - 0.9025x_1(n-2) + w_1(n) \\ x_2(n) &= -0.5x_1(n-1) + w_2(n) \\ x_3(n) &= 0.4x_2(n-2) + w_3(n) \\ x_4(n) &= -0.5x_3(n-1) + 0.25\sqrt{2}x_4(n-1) + w_4(n). \end{aligned} \tag{4.54}$$

The magnitude-squared DCs between all signals are shown in Fig. 4.4(b), and the magnitude-squared coherence is shown for comparison in Fig. 4.4(c). Obviously, the magnitude-squared coherence does neither allow conclusions about the direction of the causal coupling, nor about whether the causal coupling is direct or indirect. While the former problem is solved by the DC, the latter problem still remains. However, Fig. 4.4(a) illustrates that this problem may as well become an advantage when the aim is to identify the source of a process, as a strong causal coupling from S1 to all other sites can easily be identified. In fact, the DC has been employed for source identification in several studies with EEG data, e.g., [93–95].

### Partial directed coherence (PDC) and generalized PDC

The power spectral density from Eq. (4.42) can also be written as

$$\mathbf{S}(f) = \bar{\mathbf{A}}^{-1}(f)\mathbf{\Sigma}_w(\bar{\mathbf{A}}^H(f))^{-1}. \tag{4.55}$$

The inverse of $\mathbf{S}(f)$ then becomes

$$\mathbf{S}^{-1}(f) = \bar{\mathbf{A}}^H(f)\mathbf{\Sigma}_w^{-1}\bar{\mathbf{A}}(f). \tag{4.56}$$

Similar to the derivation of the DC from Eq. (4.42), two other measures of causality can be derived with Eq. (4.56) serving as a starting point. These two

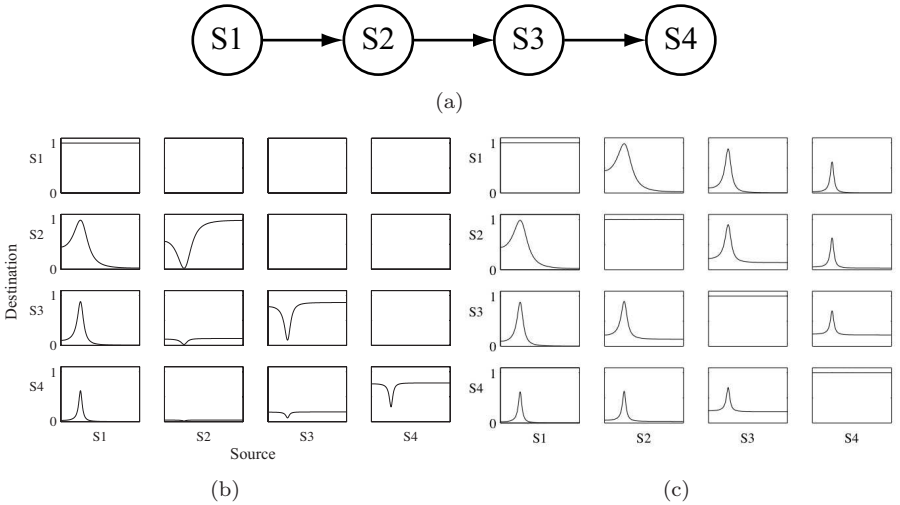


**Figure 4.4:** Illustration of (a) the causal path, (b) the magnitude-squared DC, and (c) the magnitude-squared coherence for the MVAR model from Eq. (4.54).

measures are the generalized PDC

$$\pi_{i \leftarrow j}(f) = \frac{\frac{1}{\sigma_{ii}} \bar{A}_{ij}(f)}{\sqrt{\sum_{l=1}^{N} \frac{1}{\sigma_{ll}^2} |\bar{A}_{lj}(f)|^2}} \tag{4.57}$$

and the PDC [91, 96]

$$\tilde{\pi}_{i \leftarrow j}(f) = \frac{\bar{A}_{ij}(f)}{\sqrt{\sum_{l=1}^{N} |\bar{A}_{lj}(f)|^2}}. \tag{4.58}$$

Both measures are normalized with respect to the source, i.e.,

$$\sum_{i=1}^{N} |\pi_{i \leftarrow j}(f)|^2 = 1 \tag{4.59}$$

and

$$\sum_{i=1}^{N} |\tilde{\pi}_{i \leftarrow j}(f)|^2 = 1. \tag{4.60}$$

As the PDC can be seen as a simplication of the generalized PDC, the following comments are valid for both measures, although the PDC may not be mentioned explicitly.

Unfortunately, the inverse power spectral density matrix $\mathbf{S}^{-1}(f)$ from Eq. (4.56) lacks a relevant physical interpretation, and thus the interpretation of the derived measures is less straightforward than for the DC. Similar to the DC, it has been shown that the generalized PDC can be derived as a decomposition of another frequency domain measure. This measure is the partial coherence $\kappa_{ij}(f)$, which describes the interaction between $x_i(n)$ and $x_j(n)$ when the influence due to all other $N-2$ observations is discarded. By defining $\boldsymbol{\pi}_i(f) = \begin{bmatrix}\pi_{1\leftarrow i}(f) & \dots & \pi_{N\leftarrow i}(f)\end{bmatrix}^T$ the partial coherence can be expressed as [91]

$$\kappa_{ij}(f) = \boldsymbol{\pi}_i^H(f)\boldsymbol{\pi}_j(f). \tag{4.61}$$

However, the partial coherence is a measure not quite as frequently used as the ordinary coherence when analyzing multivariate systems.

The simplest way to approach the generalized PDC is probably the fact that $|\pi_{i\leftarrow j}(f)|^2 = 0$ for all frequencies if and only if there is no direct Granger causality from $x_j(n)$ to $x_i(n)$, as the absence of direct Granger causality is equal to $a_{ij}(k) = 0$ for all $k$ and thus also $\bar{A}_{ij}(f) = 0$ for all $f$. Hence, the generalized PDC can indeed be seen to reflect Granger causality in the frequency domain. This is illustrated with the previously employed MVAR model from Eq. (4.54), for which the magnitude-squared generalized PDC as well as the magnitude-squared partial coherence are shown in Fig. 4.5. While the partial coherence can be seen to reflect the direct causal couplings only, but not their direction, the latter is overcome by the generalized PDC. However, a potential disadvantage of the generalized PDC is that it is normalized with respect to the source, and not with respect to the destination as the DC, compare Eqs. (4.45) and (4.59). This normalization is less intuitive, as the strength of the coupling should not depend on the number of other signals influenced by the same source. Consequently, also the difference in the magnitude-squared generalized PDC from two different sources to the same destination should be interpreted with caution. Nevertheless, several publications underline the practical usefulness of the generalized PDC and the PDC for analyzing propagation paths in experimental data, e.g., [97–99].

**Related measures**

For DC and DTF, it is often regarded as a disadvantage that the measures reflect total causality instead of direct causality only. In order to highlight the direct couplings, a directed DTF (dDTF) has been proposed, which is defined

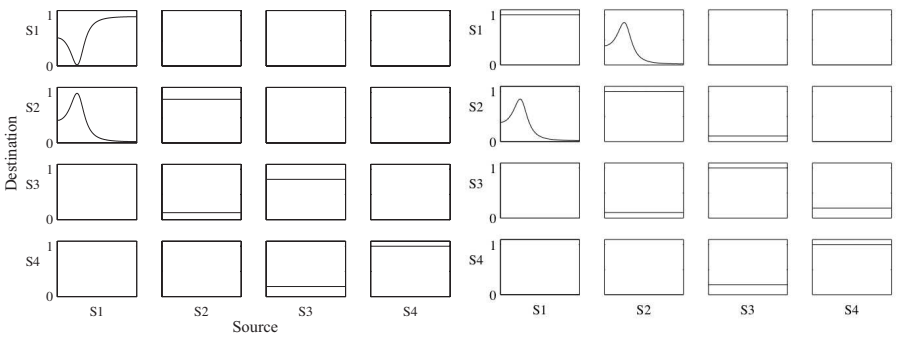


**Figure 4.5:** Illustration of (a) the magnitude-squared generalized PDC and (b) the magnitude-squared partial coherence for the MVAR model from Eq. (4.54).

as the product of the DTF and the partial coherence [100],

$$\check{\gamma}_{i\leftarrow j}(f) = \kappa_{ij}(f)\tilde{\gamma}_{i\leftarrow j}(f). \tag{4.62}$$

As both the DTF and the partial coherence are measures ranging from zero to one, also the dDTF will have values in that range. However, because of the product with $\kappa_{ij}(f)$, the dDTF from recording site $j$ to recording site $i$ can in contrast to the DTF no longer be interpreted as a fraction of the power spectrum of $x_i(n)$. Consequently, a comparison of the magnitude-squared values of the dDTF from different sources to the same destination should be less straightforward.

In order to overcome the disadvantages of the PDC regarding the normalization with respect to the source, a renormalized PDC has been proposed [101]. Its derivation is based on dividing $\bar{A}_{ij}(f)$ into its real and imaginary part,

$$\mathbf{V}_{ij}(f) = \begin{bmatrix} \mathrm{Re}(\bar{A}_{ij}(f)) \\ \mathrm{Im}(\bar{A}_{ij}(f)) \end{bmatrix}. \tag{4.63}$$

When employing LS estimation to obtain the MVAR coefficients, it can be shown that the corresponding estimate of $V_{ij}(f)$ is asymptotically normally distributed with mean $V_{ij}(f)$ and covariance matrix $\mathbf{\Sigma}_{V_{ij}}(f)/T$. This suggested to the authors to define the renormalized PDC

$$\check{\pi}_{i\leftarrow j}(f) = \mathbf{V}_{ij}^T(f)\mathbf{\Sigma}_{V_{ij}}^{-1}(f)\mathbf{V}_{ij}(f), \tag{4.64}$$

which adapts to the varying uncertainties in the estimates of $V_{ij}(f)$. However, though this renormalization may have certain statistical advantages, it does not solve the underlying problem of how to compare the values of the PDC for different sources. In fact, the renormalized PDC is normalized to neither the source nor the destination.

The MVAR model, described by Eq. (4.20) is a strictly causal model, as only time lags $k > 0$ are considered. In case instantaneous effects are present, these can not be described by the MVAR coefficients. Instead, the instantaneous effects will be explained by correlations among the residuals $\mathbf{w}(n)$, and consequently, the covariance matrix $\mathbf{\Sigma}_w$ will not be diagonal. This is, however, assumed when deriving both the DC and the generalized PDC. In order to overcome this issue, an extended definition of the PDC that also considers instantaneous effects has been proposed [102].

### 4.6.4 Significance testing

Significance testing can be described as a statistical hypothesis test with, e.g, the null hypothesis

$$\mathcal{H}_0\text{:} \quad x_j(n) \text{ is not Granger-causing } x_i(n). \tag{4.65}$$

In order to decide whether or not to reject $\mathcal{H}_0$, a discriminating statistic, e.g., the generalized PDC $\pi_{i \leftarrow j}(f)$, is calculated from the observations $\mathbf{x}(n)$ and compared to its distribution under $\mathcal{H}_0$. In some approaches, such as bootstrapping or surrogate data, the distribution of the discriminant statistic under $\mathcal{H}_0$ is estimated by direct Monte Carlo simulation [103]. For that purpose, an ensemble of bootstrap or surrogate data sets is generated such that each data set shares given properties of $\mathbf{x}(n)$, e.g., the power spectrum, but is otherwise random as specified by $\mathcal{H}_0$. The discriminant statistic is then calculated for each dataset, and, e.g., the 95th percentile of the resulting distribution is chosen to serve as the critical value based on which $\mathcal{H}_0$ can be rejected.

Recently, it has also been shown that asymptotic distributions of the DTF and the PDC for $\mathcal{H}_0$ being $\tilde{\gamma}_{i \leftarrow j}(f) = 0$ and $\tilde{\pi}_{i \leftarrow j}(f) = 0$, respectively, can be derived analytically, and thus an analytical significance threshold can be defined for these measures [104, 105].

#### Surrogate data

Surrogate data can be computed by a non-parametric procedure employing phase randomization, which originally was proposed to test non-linearity [103]. This procedure results in that, under $\mathcal{H}_0$, there will be a total absence of causal coupling between all surrogates, however, the surrogates will still have

the same power spectral density as $\mathbf{x}(n)$. In detail, each observation $x_i(n)$ is Fourier transformed, resulting in

$$X_i(f) = |X_i(f)|e^{\angle X_i(f)}. \tag{4.66}$$

The phases $\angle X_i(f)$ are then substituted by white noise $\phi_i(f)$, which is independently chosen for each $f$ from the interval $[0, 2\pi]$ and made anti-symmetric such that $\phi(f) = -\phi(-f)$. The inverse FT, denoted $\mathcal{F}^{-1}$, then gives the surrogates,

$$y_i(n) = \mathcal{F}^{-1}\left\{|X_i(f)|e^{\jmath\phi_i(f)}\right\}, \quad i = 1, \ldots, N. \tag{4.67}$$

As with bootstrapping, the repetition of this procedure generates an ensemble of surrogate data sets.

The construction of the surrogate data such that causal coupling is absent between all surrogates under $\mathcal{H}_0$ may lead to misleading significance thresholds, especially when testing for the significance of one specific direct causal coupling only. For this reason, a semi-parametric procedure for constructing causal surrogate data has been proposed [106]. This procedure results in that only one specific direct causal coupling is set to zero under $\mathcal{H}_0$, while the surrogates will still have the same power spectral density as $\mathbf{x}(n)$. In detail, it is assumed that an MVAR model has been fitted to $\mathbf{x}(n)$, resulting in estimates of the MVAR coefficients $\mathbf{A}_k$ and the covariance matrix $\mathbf{\Sigma}_w$. To test the significance of the direct causal coupling from, e.g., $x_j(n)$ to $x_i(n)$, a new set of signals $\check{\mathbf{x}}(n)$ is first computed,

$$\check{\mathbf{x}}(n) = \sum_{k=1}^{m} \check{\mathbf{A}}_k \mathbf{x}(n-k) + \check{\mathbf{w}}(n), \tag{4.68}$$

where $\check{\mathbf{w}}(n) \sim \mathcal{N}(\mathbf{0}, \mathbf{\Sigma}_w)$. The modified MVAR coefficients $\check{\mathbf{A}}_k$ are identical to $\mathbf{A}_k$ except for $\check{a}_{ij}(k) = 0$ for all $k$, implying that there is no direct causal coupling from $\check{x}_j(n)$ to $\check{x}_i(n)$. The surrogates are then defined to

$$y_i(n) = \mathcal{F}^{-1}\left\{|X_i(f)|e^{\jmath\angle\check{X}_i(f)}\right\}, \quad i = 1, \ldots, N, \tag{4.69}$$

where $\check{X}_i(f)$ is the FT of $\check{x}_i(n)$. As the generalized PDC $\pi_{i\leftarrow j}(f)$ reflects the direct causal coupling from $x_j(n)$ to $x_i(n)$, these surrogates are particularly suitable when the generalized PDC is the discriminating statistic. Appropriate causal surrogates for the DC $\gamma_{i\leftarrow j}(f)$, which reflects direct as well as indirect causal coupling from $x_j(n)$ to $x_i(n)$, have been proposed to be derived in a similar fashion by defining $\check{\mathbf{A}}_k$ to be identical to $\mathbf{A}_k$ except for $\check{a}_{il}(k) = 0$ for all $k$ and for all $l$, $l \neq i$, as well as $\check{a}_{lj}(k) = 0$ for all $k$ and for all $l$, $l \neq j$ [106]. As previously, the repetition of these procedures can be used to generate an ensemble of surrogate data sets.

**Theoretical significance thresholds**

An analytical significance threshold for the PDC has been derived in [104]. Under $\mathcal{H}_0$, it is assumed that $\tilde{\pi}_{i \leftarrow j}(f) = 0$, i.e., $|\bar{A}_{ij}(f)|^2 = 0$, see Eq. (4.57). It can be found that the asymptotic distribution of

$$\frac{T}{C_{ij}(f)} |A_{ij}(f)|^2 \tag{4.70}$$

is that of a weighted average of two independent $\chi^2$-distributed random variables each with one degree of freedom, where

$$C_{ij}(f) = \sigma_{ii}^2 \sum_{k,l=1}^{m} H_{jj}(k,l)(\cos(k\omega)\cos(l\omega) + \sin(k\omega)\sin(l\omega)), \tag{4.71}$$

with $H_{jj}(k,l)$ being an element of the inverse $\mathbf{H} = \mathbf{R}^{-1}$ of the covariance matrix $\mathbf{R}$ of $\mathbf{x}(n)$. Thus, $\mathcal{H}_0$ can be rejected at an $\alpha$-significance level if

$$|A_{ij}(f)|^2 > \frac{C_{ij}(f)}{T} \chi^2_{1,1-\alpha}, \tag{4.72}$$

or equivalently,

$$|\tilde{\pi}_{i \leftarrow j}(f)|^2 > \frac{C_{ij}(f)}{T \sum_l |A_{lj}(f)|^2} \chi^2_{1,1-\alpha}. \tag{4.73}$$

A similar derivation for an analytical significance threshold for the DTF can be found in [105].

From a computational point of view, it is clearly an advantage to be able to calculate theoretical significance thresholds, as the procedure of calculating bootstrap or surrogate data sets and the discriminating statistic must be repeated a certain number of times which can be computationally demanding. However, theoretical significance thresholds have the disadvantage of being based on an asymptotic distribution, and a comparison between the performance of theoretical versus bootstrap- or surrogate-based significance thresholds, especially for sample sizes $T \ll \infty$, has so far not been presented.

# Chapter 5

# Summary of Papers

## Paper I: Spatial Characteristics of Atrial Fibrillation Electrocardiograms

The purpose of this work is to improve the knowledge about spatial properties of AF extracted from the ECG, as well as to investigate their relation to AF organization, which is evaluated in terms of AF frequency. Spatial analysis of the ECG may provide means for non-invasive assessment of the mechanisms underlying AF. In the present study, spatial analysis is done employing the VCG, which is synthesized from the 12-lead ECG. A number of parameters are extracted from the VCG data to quantify the spatial orientation and the spatial extent, approximating the preferred direction of activation and the complexity of the activation pattern, respectively.

This study uses a database containing 26 standard 12-lead ECG recordings from patients with chronic AF. The ECGs were recorded during 5 min of which 60 s free of ectopic beats were selected for analysis. The orthogonal leads X, Y, and Z were synthesized from the ECG using the inverse Dower transform. The atrial activity is extracted using spatiotemporal QRST cancellation, thus making continuous f wave analysis possible.

The 3-D vector loops, which can be constructed from VCG data, are often displayed in the frontal (XY), transverse (XZ), or sagittal plane (YZ), see Fig. 2.4. When evaluating the spatial orientation, a new plane called the plane of best fit is calculated as the 2-D projection of the loops of the f waves that produces the minimum mean square error with respect to their original 3-D representation. This plane is determined from eigenanalysis of the covariance matrix that results from the $3 \times N$ data matrix containing the $N$ samples of

the three synthesized leads. Eigenanalysis is resulting in the three eigenvectors $\mathbf{v}_1$, $\mathbf{v}_2$, and $\mathbf{v}_3$, which are associated with the eigenvalues $\lambda_1 \geq \lambda_2 \geq \lambda_3$. The eigenvector $\mathbf{v}_1$ defines the principal axis, i.e., the axis with the largest variance among the data. The second eigenvector $\mathbf{v}_2$ spans the plane of best fit together with the principal axis. The third eigenvector $\mathbf{v}_3 = \begin{bmatrix} v_{3x} & v_{3y} & v_{3z} \end{bmatrix}^T$ is the perpendicular axis and defines the orientation of the plane of best fit, which is expressed in terms of the azimuth and elevation angles

$$\phi_{AZ} = \arctan\left(\frac{v_{3z}}{v_{3x}}\right), \tag{5.1}$$

$$\phi_{EL} = \left|\arctan\left(\frac{v_{3y}}{\sqrt{v_{3x}^2 + v_{3z}^2}}\right)\right|, \tag{5.2}$$

where $-90° < \phi_{AZ} < 90°$ and $0 < \phi_{EL} < 90°$. The azimuth angles $-30° < \phi_{AZ} < 30°$ correspond to the sagittal plane, and $60° < \phi_{AZ} < 90°$ and $-90° < \phi_{AZ} < -60°$ correspond to the frontal plane.

The parameters planarity $\phi_{PL}$ and planar geometry $\phi_{PG}$ are introduced to quantify the spatial extent of AF, and are calculated as

$$\phi_{PL} = 1 - \frac{\lambda_3}{\lambda_1 + \lambda_2 + \lambda_3}, \tag{5.3}$$

$$\phi_{PG} = \frac{\lambda_2}{\lambda_1}. \tag{5.4}$$

Planarity is close to 1 when $\lambda_3$ is much smaller than $\lambda_1$ and $\lambda_2$, i.e., when the loops are essentially planar. Planar geometry is close to 1 when the loops are essentially circular.

These spatial properties are, in each patient, obtained by applying the calculation to the entire 60-s recordings and are referred to as "global" properties. In addition, the temporal variability of the spatial parameters is calculated from successive 1-s segments, which results in mean and standard deviation (SD) values. Figure 5.1 illustrates the data of a single 1-s segment over time in the frontal, transverse, and sagittal plane as well as in the resulting plane of best fit, which is situated in the sagittal plane ($\phi_{AZ} = -23.3°$). The loops have a planar and elliptic character ($\psi_{PL} = 0.95$, $\psi_{PG} = 0.35$).

For each recording, AF frequency is obtained from the location of the dominant peak in the power spectrum of lead V1. The relation of the spatial parameters to the AF frequency is expressed in their correlation $r$ (Pearson correlation coefficient) and the related $p$-value, where $p < 0.05$ was considered statistically significant.

An overview over the global parameter values and their correlation to AF frequency is shown in Table 5.1. The results of temporal variability analysis

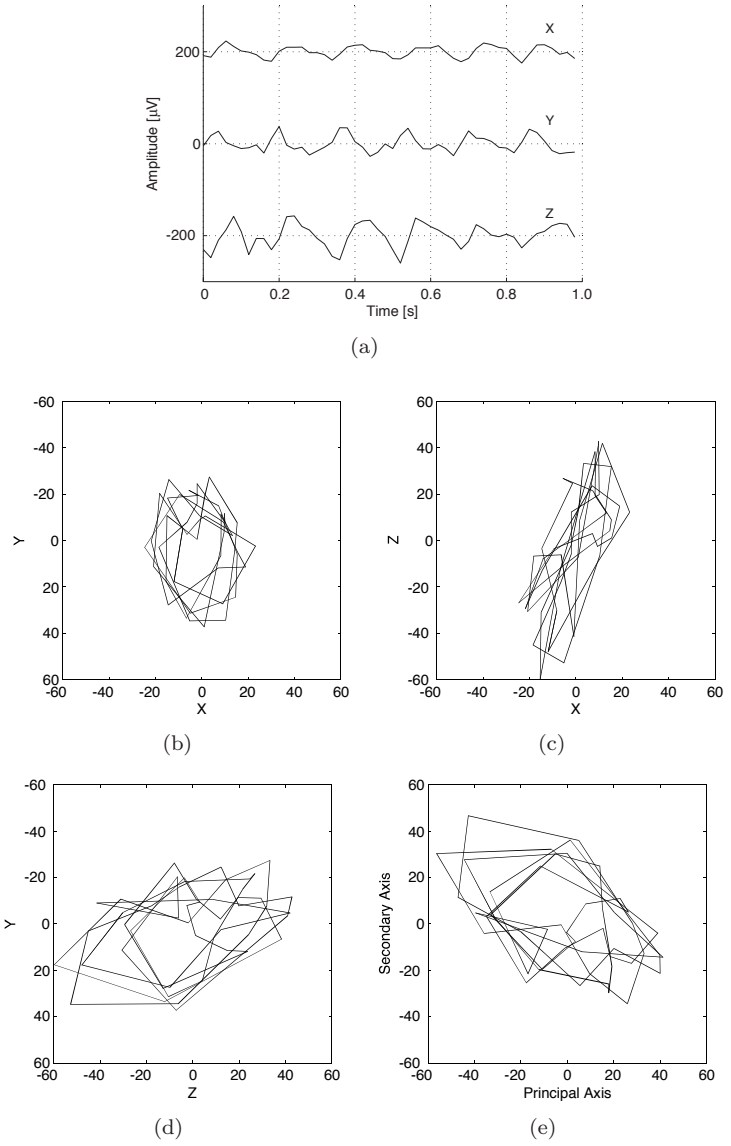


**Figure 5.1:** Example of a 1-s segment, containing approximately six f waves. (a) The orthogonal leads X, Y, and Z after QRST cancellation. (b) Frontal plane. (c) Transverse plane. (d) Sagittal plane. (e) Plane of best fit.

**Table 5.1:** Mean and standard deviation of the global parameters, and their correlation $r$ to AF frequency with the respective $p$-value.

| | mean | ± | SD | $r$ | $p$ |
|---|---|---|---|---|---|
| $\phi_{AZ}$ | $-12.6°$ | ± | $8.6°$ | 0.021 | 0.92 |
| $\phi_{EL}$ | $36.4°$ | ± | $9.8°$ | 0.239 | 0.24 |
| $\psi_{PL}$ | 0.90 | ± | 0.04 | −0.466 | 0.016 |
| $\psi_{PG}$ | 0.60 | ± | 0.18 | 0.518 | 0.0068 |

**Table 5.2:** Mean and standard deviation of the parameters for the 1-s temporal variability analysis, and their correlation $r$ to AF frequency with the respective $p$-value.

| | | mean | ± | SD | $r$ | $p$ |
|---|---|---|---|---|---|---|
| mean | $\phi_{AZ}$ | $-11.2°$ | ± | $8.0°$ | −0.024 | 0.91 |
| | $\phi_{EL}$ | $35.6°$ | ± | $8.7°$ | 0.342 | 0.09 |
| | $\psi_{PL}$ | 0.92 | ± | 0.03 | −0.510 | 0.0024 |
| | $\psi_{PG}$ | 0.46 | ± | 0.09 | 0.520 | 0.0065 |
| SD | $\phi_{AZ}$ | $17.7°$ | ± | $8.6°$ | 0.300 | 0.14 |
| | $\phi_{EL}$ | $10.3°$ | ± | $4.2°$ | 0.383 | 0.053 |
| | $\psi_{PL}$ | 0.03 | ± | 0.01 | 0.608 | 0.00099 |
| | $\psi_{PG}$ | 0.16 | ± | 0.03 | 0.543 | 0.0042 |

and the correlation of the parameter means and SDs to AF frequency are shown in Table 5.2. The results show a concentration of the azimuth angles to the sagittal view. The values of the global parameters are rather similar to the mean values from temporal variability analysis. There is no significant correlation between the global, mean, or SD values of azimuth and elevation and the AF frequency. In contrast, both the global and the mean values of planarity and planar geometry indicate a weak trend of the data to become less planar and more circular with increasing AF frequency. The temporal variability in planarity and planar geometry shows a weak trend indicating an increase with AF frequency.

## Paper II: Right Atrial Organization and Wavefront Analysis in Atrial Fibrillation

This study addresses techniques to quantify propagation patterns in intracardiac AF signals based on the detected activation times. Knowledge about the

propagation patterns during AF may help to better understand AF mechanisms and be of use during ablation procedures. The approach is developed for signals recorded with commonly used linear catheters, for which the detected activations from adjacent electrograms are combined into wavefronts. Parameters related to the consistency of the wavefronts over time and the activation order along the catheter are extracted and their potential relationships to established measures from body surface signals are investigated.

The method was evaluated using a database of 26 recordings from patients with AF who underwent catheter ablation. A Halo catheter was placed in the RA, and the five adjacent bipolar electrograms showing the strongest atrial activity were chosen for analysis. In addition, the 12-lead ECG was recorded simultaneously. All recordings were of 10-s duration and sampled with 1 kHz.

Prior to wavefront analysis, intra-atrial signal organization and the frequency dispersion between the electrograms are investigated based on time-frequency analysis. The former aspect is important to guarantee reliable activation detection, while the latter aspect is related to the observation that large dispersion of the fibrillatory frequency may indicate that the recording sites are influenced by different wavelets. Recordings with too low a degree of intra-atrial signal organization or too large frequency dispersion between the electrograms are not accepted for further analysis.

Wavefront detection is based on the assumption that two activations from two recordings sites that are closely spaced in time, are likely to belong to the same activation wavefront [73]. For activation detection, the intracardiac signals are preprocessed using bandpass filtering, rectification, and lowpass filtering, see Sec. 4.2. Threshold detection including a look-back detection mode is applied, and the detected activations are combined into wavefronts by successively processing the activations of two adjacent electrograms at a time. For each recording, the time window during which two activations are considered to belong to the same activation wavefront is chosen individually and depends on the average fibrillatory frequency in the RA, $f_{RA}$.

Wavefront characterization is based on statistics calculated from the distribution of the time-aligned complete wavefronts, where complete wavefronts are defined as wavefronts that contain one detected activation from each recording site. In order to assure reliable statistics, the minimum number of complete wavefronts required for wavefront characterization is set to half the number of the expected wavefronts, which is approximated to the product between $f_{RA}$ and the length of the recording. In recordings with consistent wavefronts, the wavefront distribution will be narrow, while the opposite is true for recordings with inconsistent wavefronts. This aspect is captured in the consistency parameter $C_{\bar{Q}}$, which is a measure that is defined based on the interquartile range of the wavefront distribution. Furthermore, the median of the distribution of

wavefronts can be interpreted as the propagation profile or the median wavefront of the recording. It allows analysis of which recording site that in the median has been activated first, and how the electrical activity propagated to the other recording sites. The linearity of the propagation profile $L$ is defined as the quality of the fit of a line to the propagation profile, and is evaluated by calculating $r^2$ that can take values between 0 and 1.

The performance of wavefront detection, as well as the proceeding wavefront characterization, is illustrated in the following by a representative example, for which the electrograms and the detected wavefronts are shown in Fig. 5.2(a). The time-aligned complete wavefronts and the corresponding statistics in form of boxplots are shown in Figs. 5.2(b) and (c), respectively. The boxplots illustrate all measures that the parameters $C_{\bar{Q}}$ and $L$ are based on, as the width of the boxes correspond to the interquartile ranges $\bar{Q}_i$ for each electrogram, and the vertical line inside of each box corresponds to the median. In this example, the wavefronts are highly consistent, as the boxes are narrow, and no outliers exist. Furthermore, the first activation occurs consistently at the recording site of H13. The activation wavefront then propagates in both directions along the catheter. For this recording, $C_{\bar{Q}}$ yields the low value of 10 ms, indicating the consistency of the wavefronts, and $L = 0.19$, indicating a non-linear propagation profile.

In addition to the analysis of the intracardiac signals, time-frequency analysis was used to calculate the AF frequency $f_1$ and the exponential decay of the harmonic magnitudes $\gamma_1$ from lead V1. AF frequency is a measure related to AF organization, while the exponential decay is a coarse measure of waveform morphology, e.g., large harmonics reflect a signal with sharp edges and result in a small exponential decay and vice versa.

Intra-atrial signal organization divided the database into one group of nine recordings, which had a too low degree of intra-atrial signal organization for wavefront analysis, and a group of 17 recordings with a sufficient degree of intra-atrial signal organization. For the latter group, wavefront detection was performed for 7.9±1.5 s and resulted in 34±13 complete wavefronts per recording. In 2 of these 17 recordings, the number of complete wavefronts did not exceed $M_{min}$, and thus wavefront characterization was performed in 15 recordings. Wavefront consistency $C_{\bar{Q}}$ yielded 15.1±5.6 ms and showed no significant correlation to the body surface parameters $f_1$ and $\gamma_1$, which yielded 6.1±0.8 Hz and 1.4±0.3, respectively, for the entire database. The linearity of the propagation profile $L$ yielded 0.74±0.31.

For AF frequency, a significant difference was found between the two groups of recordings with a too low/sufficient degree of intra-atrial signal organization ($f_1 = 6.6\pm1.0$ Hz/$5.8\pm0.5$ Hz, $p = 0.008$). The significant difference remained when the two recordings for which $M_{min}$ was not exceeded were removed from

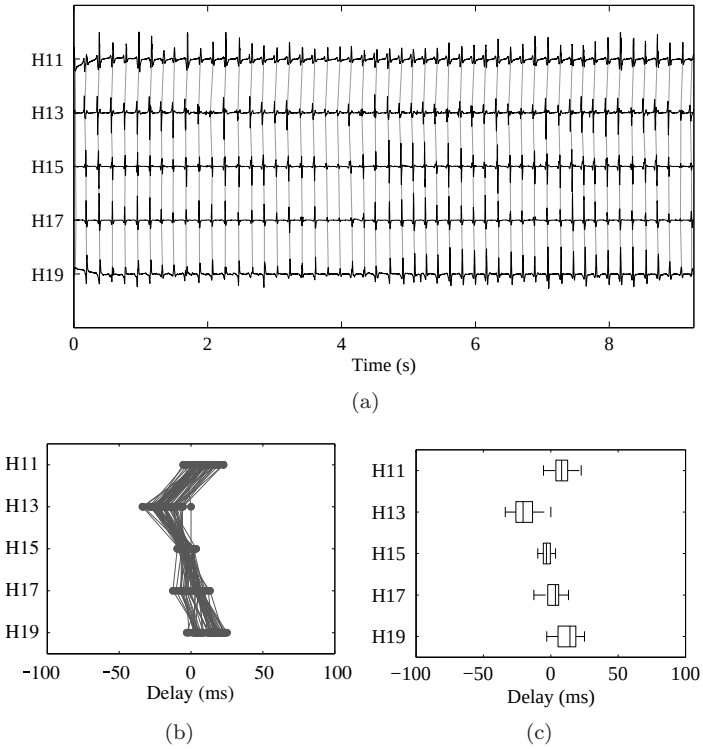


**Figure 5.2:** Example of a recording with consistent wavefronts and a non-linear propagation profile. (a) The original electrograms with the detected wavefronts. (b) The time-aligned complete wavefronts. (c) Boxplots illustrating the statistics of the distribution of the time-aligned complete wavefronts.

the group of recordings with a sufficient degree of intra-atrial signal organization ($f_1 = 6.6\pm1.0$ Hz/$5.8\pm0.5$ Hz, $p = 0.014$). For the exponential decay, a significant difference between the groups could only be found in the latter case ($\gamma_1 = 1.5\pm0.3/1.4\pm0.3$, $p = 0.082$ and $\gamma_1 = 1.5\pm0.3/1.3\pm0.3$, $p = 0.026$, respectively).

The present study showed that it is possible to detect wavefronts, reflecting the propagation pattern of the electrical activity during AF along a one-dimensional catheter when intra-atrial signal organization aspects are taken into account. While the degree of wavefront consistency was not reflected by the applied body surface measures, AF frequency calculated from lead V1 could

distinguish between recordings with different degrees of intra-atrial signal organization.

## Paper III: A Novel Approach to Propagation Pattern Analysis in Intracardiac Atrial Fibrillation Signals

Similar to Paper II, the purpose of this study is to investigate propagation patterns in intracardiac signals recorded during AF. In order to avoid certain difficulties that come with atrial activation detection, an approach in the frequency domain is employed. In particular, the approach is based on the generalized PDC which evaluates directional coupling between multiple signals in the frequency domain. The generalized PDC is evaluated at the dominant frequency of AF signals and tested for significance using a surrogate data procedure specifically designed to assess direct causality. Besides avoiding the need for atrial activation detection, there are several other advantages compared to existing methods: The approach quantifies the directional coupling and identifies the propagation pattern between the recording sites by employing a multivariate approach that simultaneously evaluates all signals. Furthermore, the method can handle an increasing number of recorded signals and does not require any knowledge on the relative positioning of the recording sites. Yet another advantage of the method is that the time delays between different recording sites can be estimated.

The method's potential is illustrated with two simulation scenarios based on a detailed ionic model of the human atrial myocyte as well as with three real data recordings, selected to present typical propagation mechanisms and recording situations in atrial tachyarrhythmias. All recordings are of 5 s duration and sampled with 1 kHz. The preprocessing consists of bandpass filtering, rectification, and lowpass filtering [58], as well as decimation of the sampling rate to 100 Hz.

In order to obtain the generalized PDC, each set of $N$ simultaneous observations $\mathbf{x}(n) = \begin{bmatrix} x_1(n) & \cdots & x_N(n) \end{bmatrix}^T$ is assumed to be represented by an MVAR model of order $m$, for which the AR coefficient matrices $\mathbf{A}_k$, $k = 1, \ldots, m$, are estimated using the LS method, and the optimal model order $m$ is determined by the BIC. For reasons of convenience, the magnitude-squared generalized PDC $|\pi_{i \leftarrow j}(f)|^2$ is referred to as PDC in the following. Details on the methodology can be found in Sec. 4.6.

During AF, the PDC is of special interest in an interval centered around the DF of the source $x_j(n)$, here assumed to represent the mean atrial fibrillatory

cycle length at the corresponding recording site. Thus, the integrated PDC is defined by [107]

$$\Pi_{ij}^2 = \frac{1}{2\Delta f} \int_{f_0-\Delta f}^{f_0+\Delta f} |\pi_{i \leftarrow j}(f)|^2 df, \tag{5.5}$$

where $f_0$ is the DF, corresponding to the highest peak in the 3–12 Hz range of the auto-spectrum of $x_j(n)$, denoted $S_{jj}(f)$, and $\Delta f$ is set to 0.5 Hz. The integral is normalized such that it, similar to the PDC, ranges from 0 to 1, and thus represents the average coupling strength from $x_j(n)$ to $x_i(n)$ in the frequency range of interest. The auto-spectra $S_{jj}(f)$ are the diagonal elements in the power spectral density matrix $\mathbf{S}(f)$ of the MVAR process, see Eq. (4.55).

The time delay from $x_j(n)$ to $x_i(n)$, denoted $\Delta_{ij}$, can be estimated from the phase spectrum $\phi_{ij}(f)$ of the corresponding cross-spectral density $S_{ij}(f)$ [108] to

$$\Delta_{ij} = \arg\max_{\delta} \int_{f_0-\Delta f}^{f_0+\Delta f} \frac{C_{ij}(f)}{1 - C_{ij}(f)} \cos\left[\phi_{ij}(f) - 2\pi f \delta\right] df, \tag{5.6}$$

where $C_{ij}(f)$ is the magnitude-squared coherence spectrum, see Eq. (4.4). The estimator in Eq. (5.6) evaluates the weighted goodness-of-fit of a line with slope $\delta$ to the phase spectrum over the frequency range of interest. The delay estimation is only computed when the corresponding integrated PDC is significant, which is assessed by means of a statistical approach based on surrogate data testing [106].

One of the simulation scenarios is mimicking AF with a multiple wavelet propagation and an ectopic focus, which is firing regularly with a period of 275 ms. As shown in Fig. 5.3(a), the result is a regular propagation in proximity to the focus (site S1), which progressively deteriorates when entering the area dominated by the multiple wavelet behavior (lower part of the sphere). The simulated signals were obtained after the point source became active and are displayed in Fig. 5.3(b). The corresponding results of the MVAR analysis ($p = 5$) are shown in Fig. 5.4. The estimated auto-spectra of the signals are displayed on the diagonal, while the PDCs are shown together with their corresponding significance thresholds on the off-diagonal. The direct coupling of, e.g., the signal recorded at site S1 towards the other signals is reflected by $|\pi_{i \leftarrow 1}(f)|^2$, $i > 1$, displayed in the first column. A significant direct coupling from S1 is only identified towards S2, as only $|\pi_{2 \leftarrow 1}(f)|^2$ exceeds its significance threshold. Further evaluation of the PDCs shows that a significant direct coupling can be observed from S1 $\rightarrow$ S2 $\rightarrow$ S3 $\rightarrow$ S4, while towards recording site S5, no significant direct coupling is present. It can thus be concluded that there is an activation wavefront which is passing S1, S2, S3, and S4, but which is not propagating further towards S5. This well reflects the propagation of the activation wavefront starting at the point source as well as the more chaotic

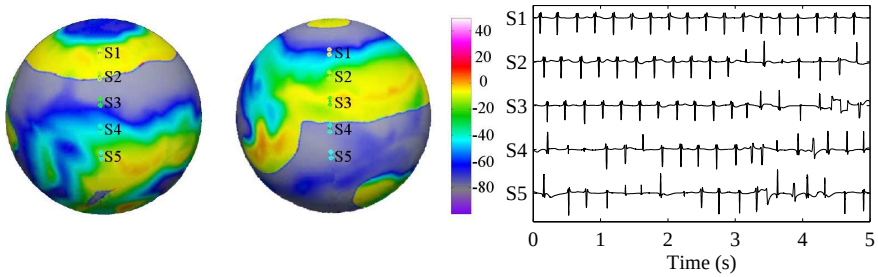


(a) (b)

**Figure 5.3:** Illustration of the AF simulation scenario: (a) Snapshots of the membrane voltage with the electrode positions indicated (snapshots are 120 ms apart). (b) The simulated electrograms.

propagation on the lower half of the sphere. The decreasing values of $\Pi^2_{21}$, $\Pi^2_{32}$, and $\Pi^2_{43}$, being equal to 0.59, 0.31, and 0.15, respectively, indicate the decreasing relevance of the activation wavefront for the atrial activity at S1 to S4. The delays $\Delta_{21}$, $\Delta_{32}$, and $\Delta_{43}$ are estimated to 51 ms, 48 ms, and 56 ms, respectively.

The method was evaluated on both atrial flutter and fibrillation electrograms, recorded with different mapping modalities. The evaluation of the propagation pattern during atrial flutter ($N = 4$ signals) evidenced the typical sequential activation found during reentrant activity. The resulting propagation patterns during AF ($N = 5/26$ signals) provided more detailed information about the underlying mechanisms of the arrhythmia. In both cases, the site of earliest activation within the recording area was found to be in the high septal RA, suggesting atrial impulses entering the RA from the LA through the Bachmans bundle region. This agrees with the role of the LA as a driver of AF as well as with previous findings about RA breakthrough sites.

In conclusion, a novel approach has been introduced to the characterization of atrial propagation patterns during atrial tachyarrhythmias. The method's potential has been illustrated by deriving plausible propagation patterns for both simulated and real data recordings, and thus the method may serve as a support for the electrophysiologist when locating ablation sites. Moreover, the possibility of quantifying the propagation pattern in terms of direction and strength of the coupling as well as the propagation delay can be applied to efficiently evaluate such patterns in existing databases.

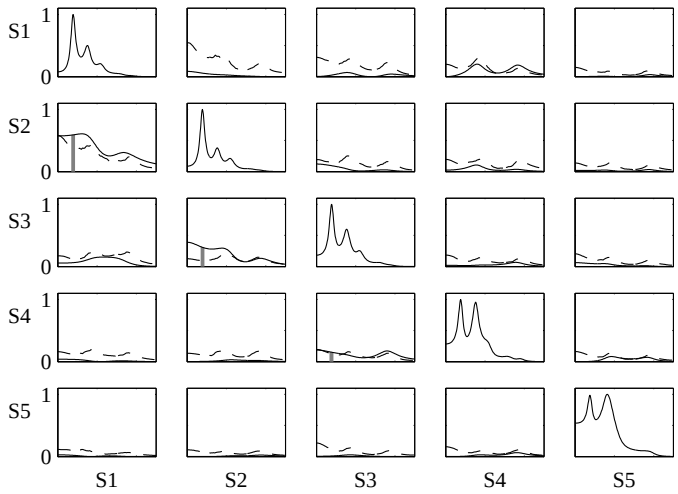


**Figure 5.4:** MVAR analysis applied to simulated AF signals. On the diagonal: The auto-spectra of the signals for $f \in [0, 25]$ Hz. Off-diagonal: The PDCs $|\pi_{i \leftarrow j}(f)|^2$ (solid line) and the corresponding significance thresholds $|\tilde{\pi}_{i \leftarrow j}(f)|^2$ (dashed line) for $f \in [0, 25]$ Hz. The area beneath $|\pi_{i \leftarrow j}(f)|^2$, $f \in [f_0 - \Delta f, f_0 + \Delta f]$, has been highlighted when $\Pi_{ij}^2$ is significant.

## Paper IV: Propagation Pattern Analysis in Intracardiac Atrial Fibrillation Signals Based on Sparse Modeling

In Paper III, the PDC was introduced for estimating propagation patterns in intracardiac AF signals. The derivation of the PDC is entirely based on the coefficients of the MVAR model, which is commonly fitted to the multichannel recordings employing LS estimation. The estimation of the MVAR coefficients can be improved, e.g., with respect to overfitting, by considering methods that put constraints onto the LS solution. Further improvements may be achieved with constraints yielding sparse solutions, which stands in contrast to the assumption of "full" connectivity during LS estimation, i.e., coupling between all recording sites. The usage of sparse estimation methods in the context of AF can be motivated by the observation that connectivity during AF may be viewed as *a priori* sparse, as it is well-known that the coupling between the recording sites during AF decreases with increasing distance.

In order to improve the LS-based estimation of the MVAR coefficients, and thus the PDC, sparse modeling employing the adaptive group LASSO is proposed in Paper IV. Besides being superior to LS estimation regarding overfitting of the solution, the adaptive group LASSO is designed such that it yields a sparse solution and allows functional grouping of the unknown parameters which can only be pruned jointly. Thus, by grouping together those MVAR coefficients which model the coupling from one signal to another, a solution which is sparse with respect to both the MVAR coefficients and the causal coupling can be achieved. Furthermore, in the adaptive group LASSO different amounts of shrinkage can be applied to different groups of parameters by choosing appropriate weighting factors. This is taken advantage of by defining weighting factors depending on the distances between the recording sites, which is an information that is particularly relevant when analyzing AF recordings.

In more detail, the weighting factors $\alpha_l$ which are employed in the adaptive group LASSO constraint, see Eq. (4.27), are usually chosen to adapt to the data by employing the LS solution $\tilde{\boldsymbol{\beta}}_l$ of the MVAR coefficients in the corresponding group,

$$\alpha_l = ||\tilde{\boldsymbol{\beta}}_l||^{-\gamma_1}, \tag{5.7}$$

where $\gamma_1 > 0$. In the proposed distance-adaptive group LASSO, additional prior knowledge is included in the estimation procedure by letting the weighting factors also adapt to the distance, i.e.,

$$\alpha_l = \alpha(d_l)||\tilde{\boldsymbol{\beta}}_l||^{-\gamma_1}, \tag{5.8}$$

where $d_l$ is a measure of distance between the recording sites of the direct coupling under evaluation, and $\alpha(d_l)$ is here defined to be the Gaussian kernel function,

$$\alpha(d_l) = \exp\left(\frac{1}{2}\frac{d_l^2}{\gamma_2^2}\right) \tag{5.9}$$

where $\gamma_2 > 0$. This choice of weights is such that the solution is more likely to become sparse with respect to those groups of MVAR coefficients which model direct couplings over longer distances.

In order to evaluate the impact of the different estimation methods for the MVAR coefficients on the PDC, a number of simulations are carried out for different samples sizes. The evaluation of the simulations is done with respect to the accuracy in detecting the direct couplings as well as accuracy in estimating the MVAR coefficients and derived measures. The adaptive and distance-adaptive group LASSO both offer major improvements with respect to detection and estimation accuracy when compared to LS estimation. While these accuracies are rather similar for adaptive and distance-adaptive group

LASSO when more samples are analyzed, improvements can be observed with the distance-adaptive group LASSO for smaller sample sizes.

The method has also been evaluated on two 5-s segments of a recording of paroxysmal AF, acquired with a basket catheter in the RA. A schematic representation of the positions of the recording sites and the electrograms of the first 5-s segment are shown in Fig. 5.5(a) and (b), respectively. The corresponding propagation pattern obtained from MVAR coefficients estimated with LS estimation as well as adaptive and distance-adaptive LASSO can be found in Fig. 5.6. For LS estimation, a large number of significant direct couplings are present also over longer distances, leading to difficulties in the identification of the propagation pattern, see Fig. 5.6(a). The identification of the propagation pattern is substantially simplified by the sparsity achieved with adaptive group LASSO, see Fig. 5.6(b). It can be observed that this sparsity is mostly present for direct couplings over longer distances, which is interesting as the adaptive group LASSO does not make use of the distances between the recording sites. When employing these distances in the distance-adaptive group LASSO, a further increase in sparsity among the direct couplings over long distances can be observed, see Fig. 5.6(c).

The directed graphs of both adaptive and distance-adaptive group LASSO suggest a propagation originating from the low septal RA close by recording sites EF3 and EF4. From there, the electrical activity propagates caudocranially in the septal RA as well as transversely towards the anterior and posterior RA. In the posterior/postero-lateral wall, craniocaudal propagation is indicated, and finally, the propagation spreads towards the lateral RA from both anterior and postero-lateral regions. This propagation pattern agrees with previous clinical observations, and an RA breakthrough site close to the coronary sinus ostium, usually superior or posterior to the orifice as also observed in the present example, has been associated to AF originating in the inferior LA or the inferior PV [109].

In conclusion, sparse modeling has been introduced for the estimation of propagation patterns during AF. In simulations, it was indicated that additional prior information on the underlying topology in form of the distances between the recording sites can, to some extent, compensate for the decrease in performance which otherwise comes with decreasing sample size. Similar to the simulations, large improvements are achieved for the real data recordings by employing adaptive group LASSO instead of LS estimation. The results also indicate that further improvements in the estimation of the propagation pattern are possible when the distance between the recording sites is known or can be estimated. This further promotes the PDC as a method for analysis of AF propagation patterns, which may contribute to a better understanding of AF mechanisms as well as improved AF treatment.

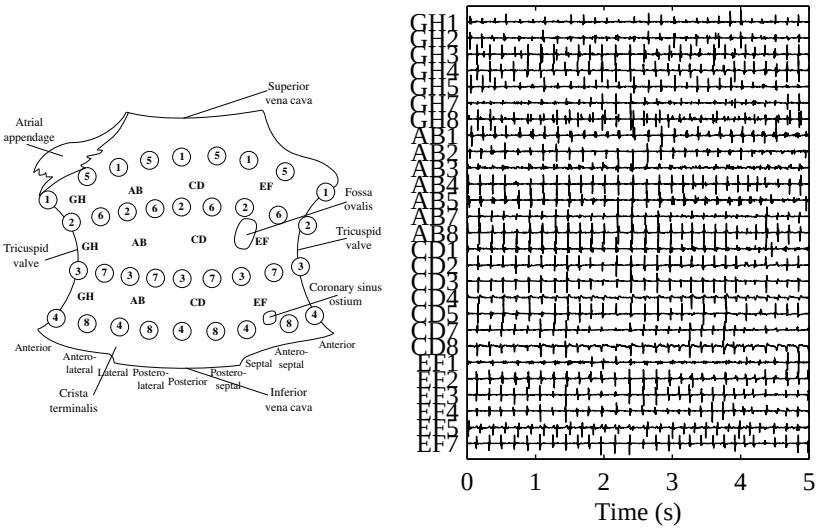


**Figure 5.5:** (a) Schematic representation of the open RA with the position of the bipolar recording sites on the intracardiac wall. The eight splines of the basket catheter were positioned on the anterior, lateral, posterior, and septal walls, as well as on intermediate positions. (b) Original electrograms.

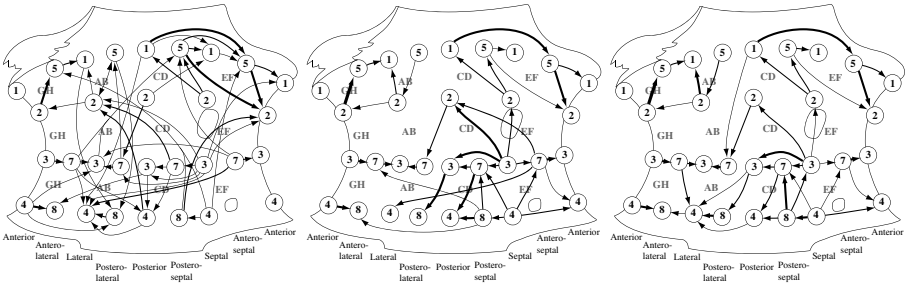


**Figure 5.6:** Directed graphs illustrating the propagation pattern during a 5-s segments of an AF recording based on (a) LS estimation, (b) adaptive group LASSO, and (c) distance-adaptive group LASSO. In order to simplify the interpretation, the directed graphs are restricted to significant $\Pi_{ij}^2 \geq 0.05$. The width of each arrow is proportional to the size of the corresponding $\Pi_{ij}^2$.

# References


[1] V. Fuster, L. E. Rydén, D. S. Cannom, H. J. G. Crijns, A. B. Curtis, K. A. Ellenbogen, *et al.*, "ACC/AHA/ESC 2006 guidelines for the management of patients with atrial fibrillation: a report of the American College of Cardiology/American Heart Association Task Force on practice guidelines and the European Society of Cardiology Committee for practice guidelines developed in collaboration with the European Heart Rhythm Association and the Heart Rhythm Society," *Europace*, vol. 8, pp. 651–745, 2006.

[2] L. Sörnmo and P. Laguna, *Bioelectrical Signal Processing in Cardiac and Neurological Applications*. Amsterdam: Elsevier (Academic Press), 2005.

[3] G. Moe, "On the multiple wavelet hypothesis of atrial fibrillation," *Arch. Int. Pharmacodyn. Ther.*, vol. 140, pp. 183–188, 1962.

[4] M. Haïssaguerre, F. I. Marcus, B. Fischer, and J. Clémenty, "Radiofrequency catheter ablation in unusual mechanisms of atrial fibrillation: report of three cases," *J. Cardiovasc. Electrophysiol.*, vol. 5, pp. 743–751, 1994.

[5] P. Jaïs, M. Haïssaguerre, D. C. Shah, S. Chouairi, L. Gencel, M. Hocini, and J. Clémenty, "A focal source of atrial fibrillation treated by discrete radiofrequency ablation," *Circulation*, vol. 95, pp. 572–576, 1997.

[6] M. Haïssaguerre, P. Jaïs, D. Shah, A. Takahashi, M. Hocini, G. Quiniou, S. Garrigue, A. L. Mouroux, P. L. Métayer, and J. Clémenty, "Spontaneous initiation of atrial fibrillation by ectopic beats originating in the pulmonary veins," *N. Engl. J. Med.*, vol. 339, pp. 659–666, 1998.

[7] M. Mansour, R. Mandapati, O. Berenfeld, J. Chen, F. Samie, and J. Jalife, "Left-to-right gradient of atrial frequencies during acute atrial fibrillation in the isolated sheep heart," *Circulation*, vol. 103, pp. 2631–36, 2001.

[8] S. Lazar, S. Dixit, F. Marchlinski, D. Callans, and E. Gerstenfeld, "Presence of left-to-right atrial frequency gradient in paroxysmal but not persistent atrial fibrillation in humans," *Circulation*, vol. 110, pp. 3181–86, 2004.

[9] J. Jalife, O. Berenfeld, and M. Mansour, "Mother rotors and fibrillatory conduction: a mechanism of atrial fibrillation," *Cardiovasc. Res.*, vol. 54, pp. 204–216, 2002.

[10] H. Calkins, J. Brugada, D. L. Packer, R. Cappato, S.-A. Chen, H. J. G. Crijns, *et al.*, "HRS/EHRA/ECAS expert consensus statement on catheter and surgical ablation of atrial fibrillation: recommendations for personnel, policy, procedures and follow-up," *Heart Rhythm*, vol. 4, pp. 816–861, 2007.

[11] K. Nademanee, E. Lockwood, N. Oketani, and B. Gidney, "Catheter ablation of atrial fibrillation guided by complex fractionated atrial electrogram mapping of atrial fibrillation substrate," *J. Cardiology*, vol. 55, pp. 1–12, 2010.

[12] K. Nademanee, J. McKenzie, E. Kosar, M. Schwab, B. Sunsaneewitayakul, T. Vasavakul, C. Khunnawat, and T. Ngarmukos, "A new approach for catheter ablation of atrial fibrillation: mapping of the electrophysiologic substrate," *J. Am. Coll. Cardiol.*, vol. 43, pp. 2044–53, 2004.

[13] L. Calò, E. de Ruvo, L. Sciarra, R. Gricia, G. Navone, L. de Luca, F. Nuccio, A. Sette, C. Pristipino, A. Dulio, F. Gaita, and E. Lioy, "Diagnostic accuracy of a new software for complex fractionated electrograms identification in patients with persistent and permanent atrial fibrillation," *J. Cardiovasc. Electrophysiol.*, vol. 19, pp. 1024–30, 2008.

[14] J. Wu, H. Estner, A. Luik, E. Ucer, T. Reents, A. Pflaumer, B. Zrenner, G. Hessling, and I. Deisenhofer, "Automatic 3D mapping of complex fractionated atrial electrograms (CFAE) in patients with paroxysmal and persistent atrial fibrillation," *J. Cardiovasc. Electrophysiol.*, vol. 19, pp. 897–903, 2008.

[15] I. Deisenhofer, H. Estner, T. Reents, S. Fichtner, A. Bauer, J. Wu, C. Kolb, B. Zrenner, C. Schmitt, and G. Hessling, "Does electrogram guided substrate ablation add to the success of pulmonary vein isolation in patients with paroxysmal atrial fibrillation? A prospective, randomized study," *J. Cardiovasc. Electrophysiol.*, vol. 20, pp. 514–521, 2009.

[16] H. Oral, A. Chugh, E. Good, A. Wimmer, S. Dey, N. Gadeela, *et al.*, "Radiofrequency catheter ablation of chronic atrial fibrillation guided by complex electrograms," *Circulation*, vol. 115, pp. 2606–12, 2007.

[17] M. Holm, S. Pehrson, M. Ingemansson, L. Sörnmo, R. Johansson, L. Sandhall, M. Sunemark, B. Smideberg, C. Olsson, and S. B. Olsson, "Non-invasive assessment of the atrial cycle length during atrial fibrillation in man: introducing, validating and illustrating a new ECG method," *Cardiovasc. Res.*, vol. 38, pp. 69–81, 1998.

[18] S. Petrutiu, A. V. Sahakian, W. Fisher, and S. Swiryn, "Manifestation of left atrial events and interatrial frequency gradients in the surface electrocardiogram during atrial fibrillation: contributions from posterior leads," *J. Cardiovasc. Electrophysiol.*, vol. 20, pp. 1231–36, 2009.

[19] A. SippensGroenewegen, M. Lesh, F. Roithinger, W. Ellis, P. Steiner, L. Saxon, R. Lee, and M. Scheinman, "Body surface mapping of counterclockwise and clockwise typical atrial flutter: a comparative analysis with endocardial activation sequence mapping," *J. Am. Coll. Cardiol.*, vol. 35, pp. 1276–87, 2000.

[20] M. S. Guillem, A. M. Climent, F. Castells, D. Husser, J. Millet, A. Arya, C. Piorkowski, and A. Bollmann, "Noninvasive mapping of human atrial fibrillation," *J. Cardiovasc. Electrophysiol.*, vol. 20, pp. 507–513, 2009.

[21] Z. Ihara, A. van Oosterom, V. Jacquemet, and R. Hoekema, "Adaptation of the 12-lead electrocardiogram system dedicated to the analysis of atrial fibrillation," *J. Electrocardiol.*, vol. 40, pp. 68 e1–8, 2007.

[22] J. A. Kors, G. van Herpen, A. C. Sittig, and J. H. van Bemmel, "Reconstruction of the Frank vectorcardiogram from standard electrocardiographic leads: diagnostic comparison of different methods," *Eur. Heart J.*, vol. 11, pp. 1083–92, 1990.

[23] P. Rubel, I. Benhadid, and J. Fayn, "Quantitative assessment of eight different methods for synthesizing Frank VCGs from simultaneously recorded standard ECG leads," *J. Electrocardiol.*, vol. 24 (Suppl.), pp. 197–202, 1991.

[24] P. W. Macfarlane, L. Edenbrandt, and O. Pahlm, *12-Lead Vectorcardiography.* Butterworth-Heinemann, 1995.

[25] G. E. Dower, H. B. Machado, and J. A. Osborne, "On deriving the electrocardiogram from vectorcardiographic leads," *Clin. Cardiol.*, vol. 3, pp. 87–95, 1980.

[26] J. Carlson, R. Havmöller, A. Herreros, P. Platonov, R. Johansson, and S. B. Olsson, "Can orthogonal lead indicators of propensity to atrial fibrillation be accurately assessed from the 12-lead ECG?," *Europace*, vol. 7 (Suppl.), pp. 39–48, 2005.

[27] M. S. Guillem, A. V. Sahakian, and S. Swiryn, "Derivation of orthogonal leads from the 12-lead electrocardiogram. Performance of an atrial-based transform for the derivation of P loops," *J. Electrocardiol.*, vol. 41, pp. 19–25, 2008.

[28] A. van Oosterom, Z. Ihara, V. Jacquemet, and R. Hoekema, "Vectorcardiographic lead systems for the characterization of atrial fibrillation," *J. Electrocardiol.*, vol. 40, pp. 343 e1–e11, 2007.

[29] M. E. Josephson, *Clinical Cardiac Electrophysiology: Techniques and Interpretations*. Lippincott Williams & Wilkins, 3rd ed., 2002.

[30] O. Pahlm and L. Sörnmo, *Elektrokardiologi - Klinik och teknik*. Studentlitteratur, 2006.

[31] V. Jacquemet, L. Kappenberger, and C. S. Henriquez, "Modeling atrial arrhythmias: impact on clinical diagnosis and therapies," *IEEE Rev. Biomed. Eng.*, vol. 1, pp. 94–114, 2009.

[32] M. Courtemanche, R. J. Ramirez, and S. Nattel, "Ionic mechanisms underlying human atrial action potential properties: insights from a mathematical model.," *Am. J. Physiol.*, vol. 275, pp. H301–321, 1998.

[33] V. Jacquemet, N. Virag, Z. Ihara, L. Dang, O. Blanc, S. Zozor, J.-M. Vesin, L. Kappenberger, and C. Henriquez, "Study of unipolar electrogram morphology in a computer model of atrial fibrillation," *J. Cardiovasc. Electrophysiol.*, vol. 14 (Suppl.), pp. 172–179, 2003.

[34] M. Stridh and L. Sörnmo, "Spatiotemporal QRST cancellation techniques for analysis of atrial fibrillation," *IEEE Trans. Biomed. Eng.*, vol. 48, pp. 105–111, 2001.

[35] D. Raine, P. Langley, A. Murray, A. Dunuwille, and J. Bourke, "Surface atrial frequency analysis in patients with atrial fibrillation: a tool for evaluating the effects of intervention," *J. Cardiovasc. Electrophysiol.*, vol. 15, pp. 1021–26, 2004.

[36] J. J. Rieta, F. Castells, C. Sanchez, V. Zarzoso, and J. Millet, "Atrial activity extraction for atrial fibrillation analysis using blind source separation," *IEEE Trans. Biomed. Eng.*, vol. 51, pp. 1176–86, 2004.

[37] P. Langley, J. J. Rieta, M. Stridh, J. Millet, L. Sörnmo, and A. Murray, "Comparison of atrial signal extraction algorithms in 12-lead ECGs with atrial fibrillation," *IEEE Trans. Biomed. Eng.*, vol. 53, pp. 343–346, 2006.

[38] M. Stridh, L. Sörnmo, C. J. Meurling, and S. B. Olsson, "Characterization of atrial fibrillation using the surface ECG: time-dependent spectral properties," *IEEE Trans. Biomed. Eng.*, vol. 48, pp. 19–27, 2001.

[39] C. Mora, D. Husser, O. Husser, F. Castells, J. Millet, and A. Bollmann, "Systematic evaluation of time–frequency parameters from surface electrocardiograms for monitoring amiodarone effects in atrial fibrillation," in *Proc. Computers in Cardiology*, pp. 949–952, IEEE Press, 2005.

[40] M. Stridh, L. Sörnmo, C. J. Meurling, and S. B. Olsson, "Sequential characterization of atrial tachyarrhythmias based on ECG time-frequency analysis," *IEEE Trans. Biomed. Eng.*, vol. 51, pp. 100–114, 2004.

[41] A. Bollmann, N. Kanuru, K. McTeague, P. Walter, D. B. DeLurgio, and J. Langberg, "Frequency analysis of human atrial fibrillation using the surface electrocardiogram and its response to ibutilide," *Am. J. Cardiol.*, vol. 81, pp. 1439–45, 1998.

[42] A. Bollmann, K. Binias, I. Toepffer, J. Molling, C. Geller, and H. Klein, "Importance of left atrial diameter and atrial fibrillatory frequency for conversion of persistent atrial fibrillation with oral flecainide," *Am. J. Cardiol.*, vol. 90, pp. 1011–14, 2002.

[43] J. J. Langberg, J. C. Burnette, and K. K. McTeague, "Spectral analysis of the electrocardiogram predicts recurrence of atrial fibrillation after cardioversion," *J. Electrocardiol.*, vol. 31, pp. 80–84, 1998.

[44] F. Nilsson, M. Stridh, A. Bollmann, and L. Sörnmo, "Predicting spontaneous termination of atrial fibrillation using the surface ECG," *Med. Eng. & Physics*, vol. 28, pp. 802–806, 2006.

[45] F. Holmqvist, D. Husser, J. M. Tapanainen, J. Carlson, R. Jurkko, Y. Xia, R. Havmoller, O. Kongstad, L. Toivonen, S. B. Olsson, and P. Platonov, "Interatrial conduction can be accurately determined using standard 12-lead electrocardiography: validation of P-wave morphology using electroanatomic mapping in man," *Heart Rhythm*, vol. 5, pp. 413–418, 2008.

[46] K.-J. Choi, D. C. Shah, P. Jaïs, M. Hocini, L. Macle, C. Scavee, R. Weerasooriya, F. Raybaud, J. Clémenty, and M. Haïssaguerre, "QRST subtraction combined with a pacemap catalogue for the prediction of ectopy

source by surface electrocardiogram in patients with paroxysmal atrial fibrillation," *J. Am. Coll. Cardiol.*, vol. 40, pp. 2013–21, 2002.

[47] A. SippensGroenewegen, A. Natale, N. F. Marrouche, D. Bash, and J. Cheng, "Potential role of body surface ECG mapping for localization of atrial fibrillation trigger sites," *J. Electrocardiol.*, vol. 37 (Suppl.), pp. 47–52, 2004.

[48] M. Lemay, J. M. Vesin, V. Jacquemet, A. Forclaz, L. Kappenberger, and A. van Oosterom, "Spatial dynamics of atrial activity assessed by the vectorcardiogram: from sinus rhythm to atrial fibrillation," *Europace*, vol. 9 (Suppl.), pp. 109–118, 2007.

[49] J. Ng, A. Sahakian, W. Fisher, and S. Swiryn, "Atrial flutter vector loops derived from the surface ECG: does the plane of the loop correspond anatomically to the macroreentrant circuit?," *J. Electrocardiol.*, vol. 36, pp. 181–186, 2003.

[50] J. Ng, A. Sahakian, W. Fisher, and S. Swiryn, "Surface ECG vector characteristics of organized and disorganized atrial activity during atrial fibrillation," *J. Electrocardiol.*, vol. 37, pp. 91–97, 2004.

[51] S. R. Dibs, J. Ng, R. Arora, R. S. Passman, A. H. Kadish, and J. J. Goldberger, "Spatiotemporal characterization of atrial activation in persistent human atrial fibrillation: multisite electrogram analysis and surface electrocardiographic correlations – a pilot study," *Heart Rhythm*, vol. 5, pp. 686–693, 2008.

[52] M. S. Guillem, A. M. Climent, A. Bollmann, D. Husser, J. Millet, and F. Castells, "Limitations of Dower's inverse transform for the study of atrial loops during atrial fibrillation," *PACE*, vol. 32, pp. 972–980, 2009.

[53] U. Richter, M. Stridh, A. Bollmann, D. Husser, and L. Sörnmo, "Spatial characteristics of atrial fibrillation electrocardiograms," *J. Electrocardiol.*, vol. 41, pp. 165–172, 2008.

[54] S. M. Narayan and V. Bhargava, "Temporal and spatial phase analyses of the electrocardiogram stratify intra-atrial and intra-ventricular organization," *IEEE Trans. Biomed. Eng.*, vol. 51, pp. 1749–64, 2004.

[55] P. Bonizzi, M. Guillem, A. M. Climent, J. Millet, V. Zarzoso, F. Castells, and O. Meste, "Noninvasive assessment of the complexity and stationarity of the atrial wavefront patterns during atrial fibrillation," *IEEE Trans. Biomed. Eng.*, vol. 57, pp. 2147–57, 2010.

[56] C. Ramanathan, R. N. Ghanem, P. Jia, K. Ryu, and Y. Rudy, "Non-invasive electrocardiographic imaging for cardiac electrophysiology and arrhythmia," *Nature Medicine*, vol. 10, pp. 422–428, 2004.

[57] H. Oral, A. Chugh, E. Good, S. Sankaran, S. S. Reich, P. Igic, D. Elmouchi, D. Tschopp, T. Crawford, S. Dey, A. Wimmer, K. Lemola, K. Jongnarangsin, F. Bogun, F. Pelosi, and F. Morady, "A tailored approach to catheter ablation of paroxysmal atrial fibrillation," *Circulation*, vol. 113, pp. 1824–31, 2006.

[58] D. Botteron and J. Smith, "A technique for measurement of the extent of spatial organization of atrial activation during atrial fibrillation in the intact human heart," *IEEE Trans. Biomed. Eng.*, vol. 42, pp. 579–586, 1995.

[59] L. Faes, G. Nollo, R. Antolini, F. Gaita, and F. Ravelli, "A method for quantifying atrial fibrillation organization based on wave-morphology similarity," *IEEE Trans. Biomed. Eng.*, vol. 49, pp. 1504–13, 2002.

[60] R. P. M. Houben, N. M. S. de Groot, and M. A. Allessie, "Analysis of fractionated atrial fibrillation electrograms by wavelet decomposition," *IEEE Trans. Biomed. Eng.*, vol. 57, pp. 1388–98, 2010.

[61] P. Sanders, O. Berenfeld, M. Hocini, P. Jaïs, R. Vaidyanathan, L.-F. Hsu, S. Garrigue, Y. Takahashi, M. Rotter, F. Sacher, C. Scavée, R. Ploutz-Snyder, J. Jalife, and M. Haïssaguerre, "Spectral analysis identifies sites of high-frequency activity maintaining atrial fibrillation in humans," *Circulation*, vol. 112, pp. 789–797, 2005.

[62] J. Ng, A. H. Kadish, and J. J. Goldberger, "Effect of electrogram characteristics on the relationship of dominant frequency to atrial activation rate in atrial fibrillation," *Heart Rhythm*, vol. 3, pp. 1295–1305, 2006.

[63] K. R. Grzeda, S. F. Noujaim, O. Berenfeld, and J. Jalife, "Complex fractionated atrial electrograms: properties of time-domain versus frequency-domain methods," *Heart Rhythm*, vol. 6, pp. 1475–82, 2009.

[64] S. Lazar, S. Dixit, D. Callans, D. Lin, F. Marchlinski, and E. Gerstenfeld, "Effect of pulmonary vein isolation on the left-to-right atrial dominant frequency gradient in human atrial fibrillation," *Heart Rhythm*, vol. 3, pp. 889–895, 2006.

[65] T. Everett, L. Kok, R. Vaughn, R. Moorman, and D. Haines, "Frequency domain algorithm for quantifying atrial fibrillation organization

to increase defibrillation efficiency," *IEEE Trans. Biomed. Eng.*, vol. 48, pp. 969–978, 2001.

[66] K. Ropella, A. V. Sahakian, J. M. Baerman, and S. Swiryn, "The coherence spectrum. A quantitative discriminator of fibrillatory and nonfibrillatory cardiac rhythms," *Circulation*, vol. 80, pp. 112–119, 1989.

[67] H. J. Sih, A. V. Sahakian, C. E. Arentzen, and S. Swiryn, "A frequency domain analysis of spatial organization of epicardial maps," *IEEE Trans. Biomed. Eng.*, vol. 42, pp. 718–727, 1995.

[68] H. J. Sih, D. P. Zipes, E. J. Berbari, and J. E. Olgin, "A high-temporal resolution algorithm for quantifying organization during atrial fibrillation," *IEEE Trans. Biomed. Eng.*, vol. 46, pp. 440–450, 1999.

[69] F. Censi, V. Barbaro, P. Bartolini, G. Calcagnini, A. Michelucci, and S. Cerutti, "Non-linear coupling of atrial activation processes during atrial fibrillation in humans," *Biol. Cybern.*, vol. 85, pp. 195–201, 2001.

[70] B. P. T. Hoekstra, C. G. H. Diks, M. A. Allessie, and J. DeGoede, "Nonlinear analysis of epicardial atrial electrograms of electrically induced atrial fibrillation in man," *J. Cardiovasc. Electrophysiol.*, vol. 6, pp. 419–440, 1995.

[71] B. P. T. Hoekstra, C. G. H. Diks, M. A. Allessie, and J. DeGoede, "Nonlinear time series analysis: methods and applications to atrial fibrillation," *Ann. Ist. Super. Sanità*, vol. 37, pp. 325–333, 2001.

[72] C. W. J. Granger, "Investigating causal relations by econometric models and cross-spectral methods," *Econometrica*, vol. 37, pp. 424–443, 1969.

[73] V. Barbaro, P. Bartolini, G. Calcagnini, F. Censi, and A. Michelucci, "Measure of synchronisation of right atrial depolarisation wavefronts during atrial fibrillation," *Med. Biol. Eng. Comp.*, vol. 40, pp. 56–62, 2002.

[74] M. Masè, L. Faes, R. Antolini, M. Scaglione, and F. Ravelli, "Quantification of synchronization during atrial fibrillation by shannon entropy: validation in patients and computer model of atrial arrhythmias," *Physiol. Meas.*, vol. 26, pp. 911–923, 2005.

[75] K. Konings, C. Kirchhof, J. Smeets, H. Wellens, O. Penn, and M. A. Allessie, "High–density mapping of electrically induced atrial fibrillation in humans," *Circulation*, vol. 89, pp. 1665–80, 1994.

[76] M. Holm, R. Johansson, S. B. Olsson, J. Brandt, and C. Lührs, "A new method for analysis of atrial activation during chronic atrial fibrillation in man," *IEEE Trans. Biomed. Eng.*, vol. 43, pp. 198–210, 1996.

[77] P. V. Bayly, B. H. KenKnight, J. M. Rogers, R. E. Hillsley, and R. E. Ideker, "Estimation of conduction velocity vector fields from epicardial mapping data," *IEEE Trans. Biomed. Eng.*, vol. 45, pp. 563–571, 1998.

[78] M. Masè, M. Del Greco, M. Marini, and F. Ravelli, "Velocity field analysis of activation maps in atrial fibrillation a simulation study," in *IFMBE Proc.*, vol. 25, pp. 1014–17, Springer Berlin Heidelberg, 2009.

[79] F. Weber, G. Seemann, and O. Dössel, "Wave direction and conduction velocity analysis from intracardiac electrograms – a single-shot technique," *IEEE Trans. Biomed. Eng.*, vol. 57, pp. 2394–2401, 2010.

[80] H. Lütkepohl, *New Introduction to Multiple Time Series Analysis.* Springer-Verlag Berlin Heidelberg, 2005.

[81] R. Tibshirani, "Regression shrinkage and selection via the lasso," *J. Roy. Statist. Soc. Ser. B*, vol. 58, pp. 267–288, 1996.

[82] H. Wang and C. Leng, "A note on adaptive group lasso," *Comp. Stat. Data Analysis*, vol. 52, pp. 5277–86, 2008.

[83] M. Yuan and Y. Lin, "Model selection and estimation in regression with grouped variables," *J. Roy. Statist. Soc. Ser. B*, vol. 68, pp. 49–67, 2006.

[84] H. Zou, "The adaptive lasso and its oracle properties," *J. Am. Stat. Assoc.*, vol. 101, pp. 1418–29, 2006.

[85] B. Efron, T. Hastie, I. Johnstone, and R. Tibshirani, "Least angle regression," *Ann. Stat.*, vol. 32, pp. 407–451, 2004.

[86] K. P. Burnham and D. R. Anderson, "Multimodel inference: understanding AIC and BIC in model selection," *Sociol. Meth. & Res.*, vol. 33, pp. 261–304, 2004.

[87] H. Akaike, "A new look at statistical model identification," *IEEE Trans. Autom. Control*, vol. 19, pp. 716–723, 1974.

[88] G. Schwarz, "Estimating the dimension of a model," *Ann. Stat.*, vol. 6, pp. 461–464, 1978.

[89] H. Lütkepohl, *Applied Time Series Econometrics.* Cambridge University Press, 2004.

[90] L. A. Baccalá, K. Sameshima, G. Ballester, A. C. D. Valle, and C. Timo-Iaria, "Studying the interaction between brain structures via directed coherence and Granger causality," *Appl. Signal Proc.*, vol. 5, pp. 40–48, 1998.

[91] L. A. Baccalá and K. Sameshima, "Partial directed coherence: a new concept in neural structure determination," *Biol. Cybern.*, vol. 84, pp. 463–474, 2001.

[92] M. J. Kaminski and K. J. Blinowska, "A new method of the description of the information flow in the brain structures," *Biol. Cybern.*, vol. 65, pp. 203–210, 1991.

[93] M. J. Kaminski, K. J. Blinowska, and W. Szelenberger, "Topographic analysis of coherence and propagation of EEG activity during sleep and wakefulness," *Electroencephal. Clin. Neurophysiol.*, vol. 102, pp. 216–227, 1997.

[94] P. J. Franaszczuk and G. K. Bergey, "Application of the directed transfer function method to mesial and lateral onset temporal lobe seizures," *Brain Topography*, vol. 11, pp. 13–21, 1998.

[95] L. Ding, G. A. Worrell, T. D. Lagerlund, and B. He, "Ictal source analysis: localization and imaging of causal interactions in humans," *NeuroImage*, vol. 34, pp. 575–586, 2007.

[96] L. A. Baccalá, K. Sameshima, and D. Y. Takahashi, "Generalized partial directed coherence," in *Proc. 15th Intern. Conf. on Digital Signal Processing*, pp. 162–166, IEEE Press, 2007.

[97] L. A. Baccalá, M. Y. Alvarenga, and K. Sameshima, "Graph theoretical characterization and tracking of the effective neural connectivity during episodes of mesial temporal epileptic seizure," *J. Integr. Neurosci.*, vol. 3, pp. 379–396, 2004.

[98] G. G. Supp, A. Schlögl, C. J. Fiebach, T. C. Gunter, G. Vigliocco, G. Pfister, and H. Petsche, "Semantic memory retrieval: cortical couplings in object recognition in the N400 window," *Eur. J. Neurosci.*, vol. 21, pp. 1139–43, 2005.

[99] G. G. Supp, A. Schlögl, N. Trujillo-Barreto, M. M. Müller, and T. Gruber, "Directed cortical information flow during human object recognition: analyzing induced EEG gamma-band responses in brain's source space," *PLoS ONE*, vol. 2, p. e684, 2007.

[100] A. Korzeniewska, M. Manczak, M. J. Kaminski, K. J. Blinowska, and S. Kasicki, "Determination of information flow direction among brain structures by a modified directed transfer function (dDTF) method," *J. Neurosci. Meth.*, vol. 125, pp. 195–207, 2003.

[101] B. Schelter, J. Timmer, and M. Eichler, "Assessing the strength of directed influences among neural signals using renormalized partial directed coherence," *J. Neurosci. Meth.*, vol. 179, pp. 121–130, 2009.

[102] S. Erla, L. Faes, E. Tranquillini, D. Orrico, and G. Nollo, "Multivariate autoregressive model with instantaneous effects to improve brain connectivity estimation," *Int. J. Bioelectromagn.*, vol. 11, pp. 74–79, 2009.

[103] J. Theiler, S. Eubank, A. Longtin, B. Galdrikian, and J. D. Farmer, "Testing for nonlinearity in time series: the method of surrogate data," *Physica D: Nonlinear Phenomena*, vol. 58, pp. 77–94, 1992.

[104] B. Schelter, M. Winterhalder, M. Eichler, M. Peifer, B. Hellwig, B. Guschlbauer, C. Lucking, R. Dahlhaus, and J. Timmer, "Testing for directed influences among neural signals using partial directed coherence," *J. Neurosci. Meth.*, vol. 152, pp. 210–219, 2005.

[105] M. Eichler, "On the evaluation of information flow in multivariate systems by the directed transfer function," *Biol. Cybern.*, vol. 94, pp. 469–483, 2006.

[106] L. Faes, A. Porta, and G. Nollo, "Testing frequency domain causality in multivariate time series," *IEEE Trans. Biomed. Eng.*, vol. 57, pp. 1897–1906, 2010.

[107] C. Wilke, L. Ding, and B. He, "Estimation of time-varying connectivity patterns through the use of an adaptive directed transfer function," *IEEE Trans. Biomed. Eng.*, vol. 55, pp. 2557–64, 2008.

[108] T. Müller, M. Lauk, M. Reinhard, A. Hetzel, C. H. Lücking, and J. Timmer, "Estimation of delay times in biological systems," *Ann. Biomed. Eng.*, vol. 31, pp. 1423–39, 2003.

[109] S. Saksena, N. D. Skadsberg, H. B. Rao, and A. Filipecki, "Biatrial and three-dimensional mapping of spontaneous atrial arrhythmias in patients with refractory atrial fibrillation," *J. Cardiovasc. Electrophysiol.*, vol. 16, pp. 494–504, 2005.

# Part II

# Included Papers

# *Paper I*

# Spatial Characteristics of Atrial Fibrillation Electrocardiograms

**Abstract**

The present study investigates spatial properties of atrial fibrillation (AF) by analyzing VCG loops synthesized from 12-lead ECGs. Following atrial signal extraction, the spatial properties are characterized through analysis of successive, fixed-length signal segments and expressed in loop orientation, i.e., azimuth and elevation, as well as in loop morphology, i.e., planarity and planar geometry. It is hypothesized that more organized AF, expressed by a lower AF frequency, is associated with decreased variability in loop morphology. AF frequency is determined using spectral analysis.

26 patients with chronic AF were analyzed using 60-s ECG recordings. Loop orientation was similar when determined from either entire 60-s segments or 1-s segments. For 1-s segments, the correlation between AF frequency and the parameters planarity and planar geometry were 0.608 ($p < 0.001$) and 0.543 ($p < 0.005$), respectively. It is concluded that the quantification of AF organization based on AF frequency and spatial characteristics from the ECG is possible. The results suggested a relatively weak coupling between loop morphology and AF frequency when determined from the surface ECG.


U. Richter, M. Stridh, A. Bollmann, D. Husser and L. Sörnmo,
"Spatial Characteristics of Atrial Fibrillation Electrocardiograms",
in *Journal of Electrocardiology*, vol. 41, pp. 165–172, 2008.

# 1 Introduction

The earlier perception of atrial fibrillation (AF) as a disease characterized by random activation patterns has changed drastically during the last two decades thanks to the analysis of invasive electrophysiological data. One common theory explaining the mechanisms behind AF is the one in which multiple reentrant wavelets circulate within the atria [1]. Using spatial information, Gerstenfeld et al. were among the first to present evidence that atrial activation during AF in humans is not entirely random [2]. Since then, several methods for analyzing the activation patterns of AF, and quantifying its organization, have been developed [3–5]. Recent research on invasive data focuses on frequency mapping, where the dominant atrial cycle length (DACL) is determined from various parts within the atria and coronary sinus using special catheters [6–8].

Methods analyzing AF from the surface ECG are less common, although it is easily acquired in clinical routine. Since it reflects both atrial and ventricular activity, it is necessary to extract the atrial activity before analysis can be performed. Several methods have been presented for that purpose [9–12], including spatiotemporal QRST cancellation [13]. Following atrial signal extraction, spectral analysis is typically performed to determine the AF frequency from the location of the dominant peak of the power spectrum [14, 15], see also [16,17]. The AF frequency may be used to identify suitable candidates for pharmacological cardioversion, and has been found particularly sensitive and specific for prediction of AF termination following intravenous ibutilide (100 % for $\leq$ 6.0 Hz or, equivalently, 360 fibrillations per minute, fpm) [15] or oral flecainide [18]. Moreover, a low AF frequency was found to be predictive for spontaneous AF termination [19].

One of the very few ECG-based approaches to spatial analysis of atrial activity was recently presented by Ng et al. in which the preferred directions of activation of AF [20], as well as of atrial flutter [21], were determined. Their method employs the synthesized vectorcardiogram (VCG) to calculate the so-called plane of best fit, i.e., the projection of the atrial loop on a plane. These two studies required the availability of "pure" f waves, i.e., only f waves in-between QRST complexes were analyzed, and, consequently, precluded continuous analysis of spatial characteristics over time. Pure f waves were observed with the help of pacing in patients undergoing ablation of the AV junction [20]. While spatial analysis may be based on successive, individual f waves, implying that the onset and end of each individual f wave are to be delineated, such an approach is difficult to implement when analyzing clinical ECGs due to the occasional presence of low amplitude f waves and noise.

The present study investigates spatial AF properties by analyzing VCG loops synthesized from the 12-lead ECG. During intervals with ventricular ac-

tivity, the atrial signal is extracted using spatiotemporal QRST cancellation, thus making continuous f wave analysis possible. Spatial properties are characterized through joint analysis of several f wave loops being contained in successive fixed-length signal segments; accordingly, wave delineation is not required. The spatial properties are not only expressed in terms of loop orientation (i.e., angles of azimuth and elevation), but also in morphologic terms such as planarity and planar geometry of the loops and related temporal variability.

Several parameters have been suggested to characterize the degree of AF organization from electrogram analysis [3–8], but only very few parameters for noninvasive, ECG-based characterization of which the above-mentioned AF frequency is the most studied. Since this parameter is related to atrial refractoriness, it may be considered to reflect AF organization [22]. In the present study, the significance of spatial (loop morphology) parameters is studied in relation to AF frequency, hypothesizing that more organized AF, being expressed by a lower frequency, is associated with decreased variability in loop morphology. Figure 1 offers a schematic illustration of the present approach.

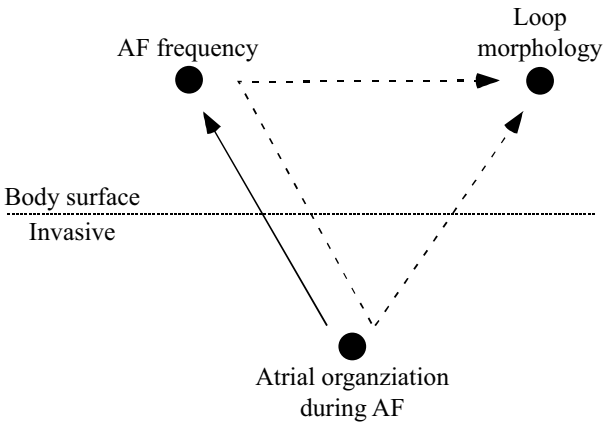


**Figure 1:** The relation between atrial organization and loop morphology is studied indirectly through AF frequency (dashed lines), as the latter quantity can be estimated from the ECG. The solid line indicates the well-established relation between atrial organization and AF frequency.

# 2 Methods

## Preprocessing

The orthogonal leads X, Y, and Z are synthesized from the 12-lead ECG using the inverse Dower transformation; see, e.g., [23]. Atrial activity is extracted through spatiotemporal QRST cancellation in which the beat averages of the three leads are combined to better cancel the ventricular activity [13]. As a result, variations in the electrical axis of the heart are accounted for in the cancellation process. Before spatial analysis, the atrial signal is decimated from 1000 to 50 Hz since the information of interest is confined to frequencies below 25 Hz.

The spatial properties are characterized by parameters calculated from the entire recording, resulting in "global" values. Spatial variability parameters are calculated from successive fixed-length 1-s segments and expressed in terms of mean and standard deviation.

AF frequency is obtained from the location of the dominant peak in the power spectrum of lead V1.

## Spatial Analysis

### Orientation

The plane of best fit is defined as the two-dimensional projection of the loop that produces the minimum mean-square error with respect to the original loop. This plane is determined from eigenanalysis of the covariance matrix that results from the $3 \times N$ data matrix with the samples of the three synthesized leads; $N$ denotes the number of samples of the segment. In the next step, eigendecomposition of the covariance matrix is performed, resulting in the three eigenvectors $\mathbf{v}_1$, $\mathbf{v}_2$, and $\mathbf{v}_3$ associated with the eigenvalues $\lambda_1 \geq \lambda_2 \geq \lambda_3$. The eigenvector $\mathbf{v}_1$ defines the principal axis, i.e., the axis with the largest correlation among the data. The second eigenvector $\mathbf{v}_2$ spans the plane of best fit together with the principal axis. The third eigenvector $\mathbf{v}_3 = [v_{3x}, v_{3y}, v_{3z}]^T$ is the perpendicular axis and defines the azimuth and elevation angles of the plane of best fit (see Fig. 2):

$$\phi_{AZ} = \arctan\left(\frac{v_{3z}}{v_{3x}}\right), \tag{1}$$

$$\phi_{EL} = \left|\arctan\left(\frac{v_{3y}}{\sqrt{v_{3x}^2 + v_{3z}^2}}\right)\right|, \tag{2}$$

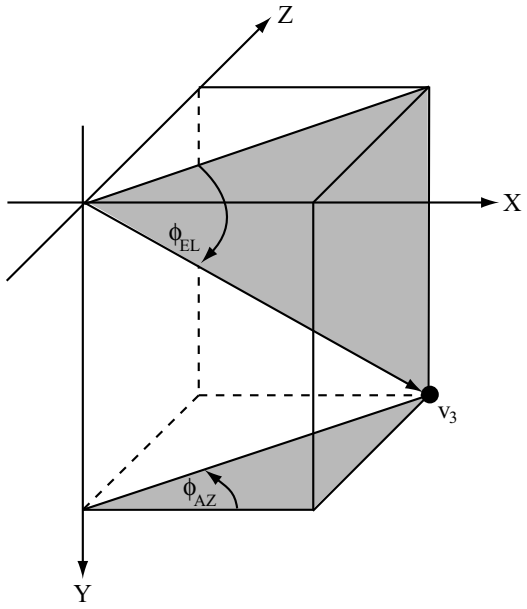


**Figure 2:** The definition of azimuth $\phi_{AZ}$ and elevation $\phi_{EL}$.

where $-90° < \phi_{AZ} < 90°$ and $0 < \phi_{EL} < 90°$. It should be noted that $-30° < \phi_{AZ} < 30°$ corresponds to the sagittal plane, and that $60° < \phi_{AZ} < 90°$ and $-90° < \phi_{AZ} < -60°$ correspond to the frontal plane. The positive and negative angles in between correspond to the right and left oblique view, respectively.

### Planarity and Planar Geometry

Planarity is defined as

$$\psi_{PL} = 1 - \frac{\lambda_3}{\lambda_1 + \lambda_2 + \lambda_3}, \tag{3}$$

and is close to 1 when $\lambda_3$ is much smaller than $\lambda_1$ and $\lambda_2$, i.e., when the loop is essentially planar. Planar geometry is defined as

$$\psi_{PG} = \frac{\lambda_2}{\lambda_1} \qquad \lambda_1 \geq \lambda_2, \tag{4}$$

and is close to 1 when the loop is essentially circular.

Figure 3 illustrates the data contained in a 1-s segment. The loops are mostly in the frontal and left sagittal plane, whereas very little in the transverse plane; and, consequently, the azimuth angle of the plane of best fit is in between 0° and −90° ($\phi_{AZ} = -23.3°$). The elevation angle $\phi_{EL}$ is 16.7°. The loops are quite planar ($\psi_{PL} = 0.95$), and have an elliptic appearance ($\psi_{PG} = 0.35$).

### Statistical Analysis

The correlation between the means as well as the standard deviations (SD) and the AF frequency are calculated, resulting in the correlation value $r$ (Pearson correlation coefficient) and related $p$-value. A p-value $< 0.05$ was considered statistically significant.

## 3 Database

The database contains 26 12-lead ECG recordings from patients with chronic AF. All recordings were acquired with equipment by Siemens-Elema AB, Sweden, using a sampling rate of 1 kHz and an amplitude resolution of 0.6 $\mu$V. The ECGs were recorded during 5 minutes of which 60 s free of ectopic beats were selected for analysis.

## 4 Results

The results are presented below for global analysis of the entire 60-s recordings and for variability analysis using 1-s segments.

The AF frequency was estimated with the above described method for each 60-s recording. For the database, the AF frequencies ranged from 3.9 to 7.7 Hz (6.4±1.0 Hz).

### Global Analysis

Figure 4 displays loop orientation in terms of global azimuth and elevation for the 26 patients. The azimuth angles are concentrated to the sagittal view: $\phi_{AZ}$ ranges between −29.5° and +3.5°. The elevation angles range between +16.1° and +60.7° and thus spread over half the possible interval. Neither global azimuth $\phi_{AZ}$ nor global elevation $\phi_{EL}$ are correlated with AF frequency as reflected by the $r$-values close to zero in Table 1. Global planarity $\psi_{PL}$ and global planar geometry $\psi_{PG}$ are displayed versus AF frequency in Figs. 5(a) and (b), respectively. It can be observed that the nature of the data is relatively planar since $\psi_{PL}$ is between 0.79 and 0.97. The correlation of $\psi_{PL}$ to the AF

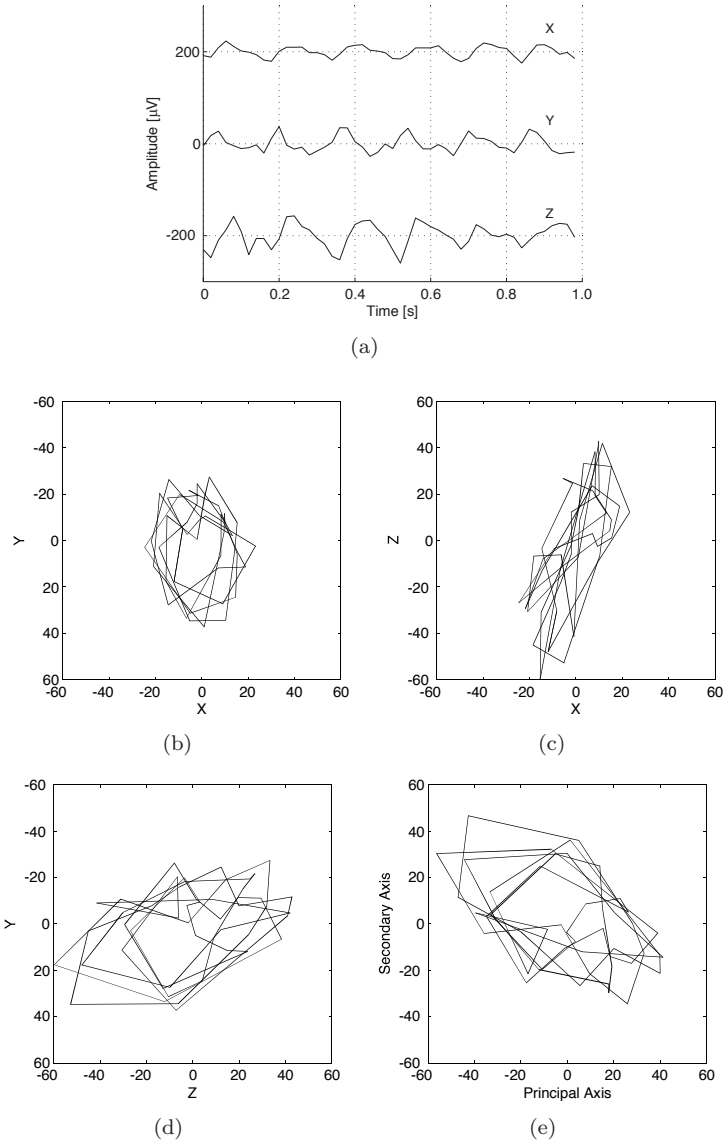


**Figure 3:** Example of a 1-s segment, containing approximately six f waves. (a) The orthogonal leads X, Y, and Z after QRST cancellation. (b) Frontal plane. (c) Transverse plane. (d) Sagittal plane. (e) Plane of best fit.

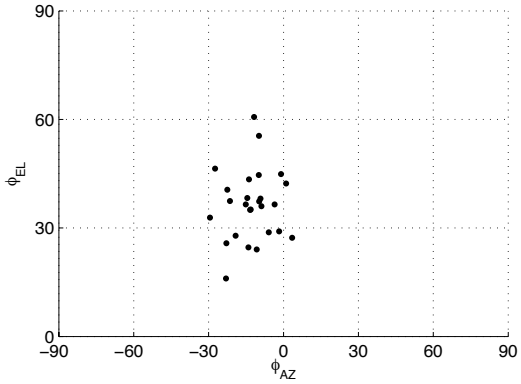


**Figure 4:** Plot over global azimuth and elevation of each 60 s recording of the database.

**Table 1:** Means and standard deviations of the global parameters, and their correlation $r$ to AF frequency with the respective $p$-value.

| | mean | ± | SD | $r$ | $p$ |
|---|---|---|---|---|---|
| $\phi_{AZ}$ | $-12.6°$ | ± | $8.6°$ | 0.021 | 0.92 |
| $\phi_{EL}$ | $36.4°$ | ± | $9.8°$ | 0.239 | 0.24 |
| $\psi_{PL}$ | 0.90 | ± | 0.04 | −0.466 | 0.016 |
| $\psi_{PG}$ | 0.60 | ± | 0.18 | 0.518 | 0.0068 |

frequency is $r = -0.466$ ($p < 0.05$) which indicates a weak trend of $\psi_{PL}$ to decrease with AF frequency. The parameter $\psi_{PG}$ spreads out over nearly the entire interval, ranging between 0.22 and 0.88. Its positive correlation value of $r = 0.518$ ($p < 0.05$) to AF frequency suggests that the data becomes slightly more circular as AF frequency increases.

## Variability analysis using 1-s segments

The mean azimuth and elevation angles obtained in 1-s segments only differ from the global values with 1.4° and 0.8°, respectively, and planarity and planar geometry with 0.02 and 0.14, respectively, see Tables 1 and 2. Thus, the results are similar to those of the global parameters, see Table 2, i.e., no correlation between AF frequency and azimuth or elevation, whereas AF frequency exhibits negative correlation with $\psi_{PL}$ ($r = -0.510$, $p < 0.005$) and positive with $\psi_{PG}$ ($r = 0.520$, $p < 0.05$).

The standard deviations of $\phi_{AZ}$, $\phi_{EL}$, $\psi_{PL}$, and $\psi_{PG}$ are displayed versus

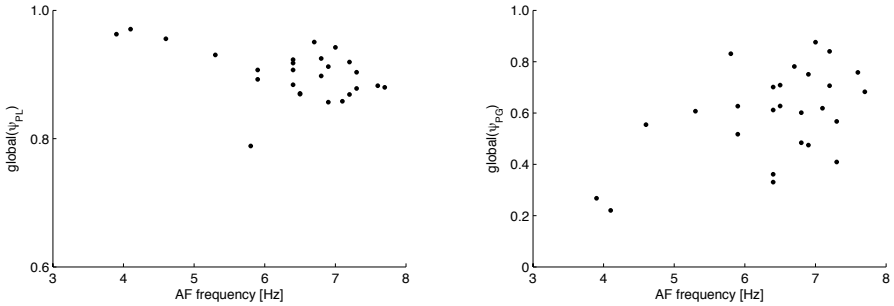


(a) (b)

**Figure 5:** Global (a) planarity and (b) planar geometry displayed as a function of AF frequency.

**Table 2:** Means and standard deviations of the parameters for the 1-s variability analysis, and their correlation $r$ to AF frequency with the respective $p$-value.

| | | mean | ± | SD | $r$ | $p$ |
|---|---|---|---|---|---|---|
| mean | $\phi_{AZ}$ | $-11.2°$ | ± | $8.0°$ | $-0.024$ | 0.91 |
| | $\phi_{EL}$ | $35.6°$ | ± | $8.7°$ | 0.342 | 0.09 |
| | $\psi_{PL}$ | 0.92 | ± | 0.03 | $-0.510$ | 0.0024 |
| | $\psi_{PG}$ | 0.46 | ± | 0.09 | 0.520 | 0.0065 |
| SD | $\phi_{AZ}$ | $17.7°$ | ± | $8.6°$ | 0.300 | 0.14 |
| | $\phi_{EL}$ | $10.3°$ | ± | $4.2°$ | 0.383 | 0.053 |
| | $\psi_{PL}$ | 0.03 | ± | 0.01 | 0.608 | 0.00099 |
| | $\psi_{PG}$ | 0.16 | ± | 0.03 | 0.543 | 0.0042 |

AF frequency in Fig. 6. The standard deviation exhibits a weak trend to increase with AF frequency for $\psi_{PL}$ ($r = 0.608, p < 0.005$) and $\psi_{PG}$ ($r = 0.543$, $p < 0.005$), suggesting increased variability in waveform morphology. The variability in orientation of the data did not change with AF frequency, see Table 2.

# 5 Discussion

We have introduced the parameters planarity and planar geometry for characterization of AF loops, previously used to analyze, e.g., the morphology of T wave loops [24]. To our knowledge, it is the first time such spatial parame-

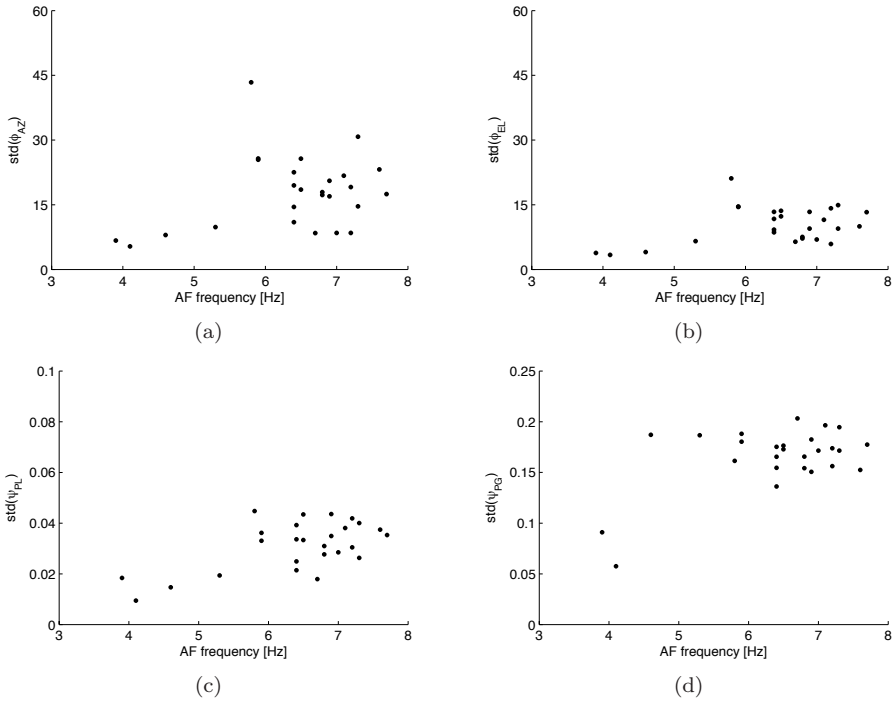


**Figure 6:** Standard deviation of (a) azimuth, (b) elevation, (c) planarity, and (d) planar geometry displayed as a function of AF frequency. The fixed-length segment was 1 s.

ters are applied to atrial activity and compared to AF frequency. In contrast to azimuth and elevation, which deal with spatial orientation of AF, these two parameters characterize the spatial extent of AF.

The calculation of the plane of best fit has previously been performed on pure atrial flutter and atrial fibrillation signals, recorded under special conditions [20, 21]. Measuring the organization of AF non-invasively was viewed as a means "to study the dynamics of AF in humans over long periods, assuming atrial activity can be extracted from the signal". The present paper advances this aspect by combining our spatiotemporal method for QRST cancellation with the calculation of the plane of best fit, offering the possibility to use the method on ECGs recorded in clinical routine.

**Orientation**

The distributions of global azimuth and elevation, obtained by applying the method to the entire recordings, were very concentrated: the angles were located exclusively in the sagittal view. As a side effect of the 1-s variability analysis, the parameter means could be compared with their corresponding global parameter values. The difference between mean azimuth and elevation and their respective global values was negligible, i.e., the calculation of the angles over 60 s is sufficient as it represents the overall spatial orientation of the data; no additional information was added by analyzing shorter segments. The analysis of the correlation between AF frequency and global and mean angles, aiming to reveal trends of the parameters for lower and higher AF frequencies, showed that there is no significant difference in orientation between the recordings. This result seems reasonable, as organized and unorganized AF are not known to persist on clearly distinguishable locations within the atria. The 1-s variability analysis for azimuth and elevation showed that the standard deviation of the angles over time was relatively low, i.e., the spatial orientation of the data was relatively stable in the sagittal view.

Our results correspond to the findings in [20], where the plane of best fit was calculated for pure f waves. It was shown that 15 of 22 analyzed ECGs were highly organized, i.e., more than 30% of the azimuth values were situated in one 30-degree region (e.g., 0°–30°, 30°–60°), which corresponds to a low standard deviation that we investigated in our variability analysis. In addition, 12 of those 15 ECGs were found to be organized close to the sagittal plane. Furthermore, studies based on invasive data for evaluation of spatial patterns during AF over time found them to be highly stable [25, 26], which again corresponds to the low standard deviation found in this study. An area of high synchronization was found in the lateral and anterolateral right atrium during paroxysmal and idiopathic AF in [26, 27]. This finding supports our observation of the general orientation of the data in the sagittal view.

A comparison of the present results with those of Ng et al. [20] should take the differences in azimuth and elevation definition into account. First, Ng et al. defined the azimuth angle from the positive Z-axis to the positive X-axis, whereas the present definition is the opposite, i.e., from the positive X-axis to the positive Z-axis. Furthermore, azimuth was defined from $-180$ to $+180$ degrees in order to specify whether the view is anterior or posterior [20]. However, such a definition results in that every plane has two possible perpendicular directions (anterior and posterior). In [20] it was decided to choose "the direction in which the projection in that plane would have a primarily counterclockwise loop". Since a distinction between clockwise and counterclockwise has little clinical implications for AF and is exceedingly difficult to determine automat-

ically, such information was not part of our analysis. Finally, the calculation of elevation did not originally include an absolute value, i.e., the angle could take positive and negative values. The sign of the result does not, however, permit a conclusion whether the view is superior or inferior, which is a mathematical limitation of the calculation. In our analysis, this limitation became obvious through elevation angles which, during the course of a recording, toggled between superior and inferior view for no obvious physiological reason, underlining that a reliable distinction between superior and inferior view is not possible. For this reason, and the fact that classification into superior and inferior view is rarely considered in AF analysis, the distinction between clockwise and counterclockwise was omitted.

**Planarity and Planar Geometry**

The global parameters show that the loops are generally two-dimensional, i.e., planarity is close to one for all recordings. Thanks to the variability analysis, the parameter means could be compared to their respective global parameter values. The difference was found to be negligible. Hence, AF frequency exhibits a negative correlation for global as well as mean planarity. This can be interpreted such that when AF is organized so that f waves are similar, which is often the case for low AF frequencies, the loops are essentially contained in a plane. When AF is unorganized and associated with higher AF frequencies, the loop becomes less planar.

The global values of planar geometry are very scattered, although exhibiting a positive correlation with AF frequency. Similar to planarity, the difference between global and mean planar geometry is negligible for 1-s segments. A positive correlation remains for the mean values of planar geometry when calculated for 1-s segments. The data has thus elliptic character at low AF frequencies, whereas the data becomes more circular, i.e., the planar geometry increases at higher AF frequencies which mostly represent unorganized AF.

The standard deviations of both planarity and planar geometry exhibited a clearly positive correlation with AF frequency, implying that the wave morphology is more stable for lower AF frequencies.

In an early stage of this study, segment length related to the dominant atrial cycle length (DACL), i.e., the inverse of the AF frequency, was studied. This was done in analogy to [20], and a segment length of 1.25·DACL was chosen in order to ensure that each segment contained one complete f wave. The results were largely similar to those of the 1-s segment analysis, with the exception that there was no correlation of planarity and planar geometry to AF frequency. This may be explained by the observation that the spatial ex-

tent of about an f wave is generally two-dimensional and with elliptic character.

An important issue is to what extent spatial AF properties can be determined from the surface ECG, ultimately indicating whether a single wavelet or multiple wavelets are circulating in the atria. The scope of present study is more modest and is restricted to studying whether or not there is a relation between the spatial surface ECG properties and AF frequency. The issue of spatial organization of AF in noninvasive recordings has previously been addressed in, e.g., [28].

**Limitations**

The inverse Dower transformation has been used previously when analyzing atrial activity [20]. Originally, this transformation was developed for analyzing QRS- and T-loops. A study that visually compared QRS loops from the Frank VCG and three different synthesized VCGs showed that the inverse Dower transformation was the best synthesis method [29]. Another study which compared eight different methods came to the same conclusion [30]. Similar investigations related to the ability of the inverse Dower transformation to preserve the atrial activity of the ECG have not been done yet. Such a study is desirable if synthesized VCGs are to be employed for AF analysis.

Since the present database only contained 26 standard 12-lead ECG recordings with a length of 60 s each, it is necessary to perform further studies with larger databases representing the range of AF frequencies more evenly. Furthermore, it would be desirable to include simultaneously recorded invasive data to better understand the relation between atrial organization and f wave morphology, see Fig. 1.

# 6 Conclusions

Loop orientation expressed in terms of azimuth and elevation can be determined from either global analysis (60 s) or the mean of segment-based analysis, both types of analysis leading to similar results. Global analysis and the mean of segment-based analysis showed increased planarity and decreased planar geometry for lower AF frequencies, possibly related to higher similarity of successive loops in more organized AF. Thus, quantification of AF organization from the ECG based on AF frequency and spatial characteristics, as expressed by planarity and planar geometry, is possible.

## References

[1] G. Moe, "On the multiple wavelet hypothesis of atrial fibrillation," *Arch. Int. Pharmacodyn. Ther.*, vol. 140, pp. 183–188, 1962.

[2] E. Gerstenfeld, A. Sahakian, and S. Swiryn, "Evidence for transient linking of atrial excitation during atrial fibrillation in humans," *Circulation*, vol. 86, pp. 375–382, 1992.

[3] H. J. Sih, D. P. Zipes, E. J. Berbari, and J. E. Olgin, "A high-temporal resolution algorithm for quantifying organization during atrial fibrillation," *IEEE Trans. Biomed. Eng.*, vol. 46, pp. 440–450, 1999.

[4] D. Botteron and J. Smith, "A technique for measurement of the extent of spatial organization of atrial activation during atrial fibrillation in the intact human heart," *IEEE Trans. Biomed. Eng.*, vol. 42, pp. 579–586, 1995.

[5] M. Holm, R. Johansson, S. B. Olsson, J. Brandt, and C. Lührs, "A new method for analysis of atrial activation during chronic atrial fibrillation in man," *IEEE Trans. Biomed. Eng.*, vol. 43, pp. 198–210, 1996.

[6] S. Lazar, S. Dixit, D. Callans, D. Lin, F. Marchlinski, and E. Gerstenfeld, "Effect of pulmonary vein isolation on the left-to-right atrial dominant frequency gradient in human atrial fibrillation," *Heart Rhythm*, vol. 3, pp. 889–895, 2006.

[7] M. Haïssaguerre, M. Hocini, P. Sanders, Y. Takahashi, M. Rotter, F. Sacher, T. Rostock, L.-F. Hsu, A. Jonsson, M. O'Neill, P. Bordachar, S. Reuter, R. Roudaut, J. Clémenty, and P. Jaïs, "Localized sources maintaining atrial fibrillation organized by prior ablation," *Circulation*, vol. 112, pp. 616–625, 2006.

[8] P. Sanders, O. Berenfeld, M. Hocini, P. Jaïs, R. Vaidyanathan, L.-F. Hsu, S. Garrigue, Y. Takahashi, M. Rotter, F. Sacher, C. Scavée, R. Ploutz-Snyder, J. Jalife, and M. Haïssaguerre, "Spectral analysis identifies sites of high-frequency activity maintaining atrial fibrillation in humans," *Circulation*, vol. 112, pp. 789–797, 2005.

[9] D. Raine, P. Langley, A. Murray, A. Dunuwille, and J. Bourke, "Surface atrial frequency analysis in patients with atrial fibrillation: a tool for evaluating the effects of intervention," *J. Cardiovasc. Electrophysiol.*, vol. 15, pp. 1021–26, 2004.

[10] J. J. Rieta, F. Castells, C. Sanchez, V. Zarzoso, and J. Millet, "Atrial activity extraction for atrial fibrillation analysis using blind source separation," *IEEE Trans. Biomed. Eng.*, vol. 51, pp. 1176–86, 2004.

[11] P. Langley, J. J. Rieta, M. Stridh, J. Millet, L. Sörnmo, and A. Murray, "Comparison of atrial signal extraction algorithms in 12-lead ECGs with atrial fibrillation," *IEEE Trans. Biomed. Eng.*, vol. 53, pp. 343–346, 2006.

[12] M. Lemay, J.-M. Vesin, A. van Oosterom, V. Jacquemet, and L. Kappenberger, "Cancellation of ventricular activity in the ECG: evaluation of novel and existing methods," *IEEE Trans. Biomed. Eng.*, vol. 54, pp. 542–46, 2007.

[13] M. Stridh and L. Sörnmo, "Spatiotemporal QRST cancellation techniques for analysis of atrial fibrillation," *IEEE Trans. Biomed. Eng.*, vol. 48, pp. 105–111, 2001.

[14] M. Holm, S. Pehrson, M. Ingemansson, L. Sörnmo, R. Johansson, L. Sandhall, M. Sunemark, B. Smideberg, C. Olsson, and S. B. Olsson, "Non-invasive assessment of the atrial cycle length during atrial fibrillation in man: introducing, validating and illustrating a new ECG method," *Cardiovasc. Res.*, vol. 38, pp. 69–81, 1998.

[15] A. Bollmann, N. Kanuru, K. McTeague, P. Walter, D. B. DeLurgio, and J. Langberg, "Frequency analysis of human atrial fibrillation using the surface electrocardiogram and its response to ibutilide," *Am. J. Cardiol.*, vol. 81, pp. 1439–45, 1998.

[16] T. Everett, R. Moorman, L. Kok, J. Akar, and D. Haines, "Assessment of global atrial fibrillation organization to optimize timing of atrial defibrillation," *Circulation*, vol. 103, pp. 2857–61, 2001.

[17] A. Fujiki, M. Sakabe, K. Nishida, M. Sugao, T. Tsuneda, J. Iwamoto, K. Mizumaki, and H. Inoue, "Drug-induced changes in fibrillation cycle length and organization index can predict chemical cardioversion of long-lasting atrial fibrillation with bepridil alone or in combination with aprindine," *Circ. J.*, vol. 68, pp. 1139–45, 2004.

[18] A. Bollmann, K. Binias, I. Toepffer, J. Molling, C. Geller, and H. Klein, "Importance of left atrial diameter and atrial fibrillatory frequency for conversion of persistent atrial fibrillation with oral flecainide," *Am. J. Cardiol.*, vol. 90, pp. 1011–14, 2002.

[19] F. Nilsson, M. Stridh, A. Bollmann, and L. Sörnmo, "Predicting spontaneous termination of atrial fibrillation using the surface ECG," *Med. Eng. & Physics*, vol. 28, pp. 802–806, 2006.

[20] J. Ng, A. Sahakian, W. Fisher, and S. Swiryn, "Surface ECG vector characteristics of organized and disorganized atrial activity during atrial fibrillation," *J. Electrocardiol.*, vol. 37, pp. 91–97, 2004.

[21] J. Ng, A. Sahakian, W. Fisher, and S. Swiryn, "Atrial flutter vector loops derived from the surface ECG: does the plane of the loop correspond anatomically to the macroreentrant circuit?," *J. Electrocardiol.*, vol. 36, pp. 181–186, 2003.

[22] A. Bollmann and F. Lombardi, "Electrocardiology in atrial fibrillation," *IEEE Eng. Med. Biol. Mag.*, vol. 25, pp. 15–23, 2006.

[23] P. W. Macfarlane, L. Edenbrandt, and O. Pahlm, *12-Lead Vectorcardiography.* Butterworth-Heinemann, 1995.

[24] F. Badilini, P. M. Blanche, J. Fayn, M. Forlini, P. Rubel, and P. Coumel, "Relationship between 12-lead ECG QT dispersion and 3D-ECG repolarization loop," in *Proc. Computers in Cardiology*, pp. 785–788, IEEE Press, 1995.

[25] A. Michelucci, P. Bartolini, G. Calcagnini, F. Censi, A. Colella, S. Morelli, L. Padeletti, P. Pieragnoli, and V. Barbaro, "Mapping the organization of atrial fibrillation with basket catheters. Part II: Regional patterns in chronic patients," *Pacing Clin. Electrophysiol.*, vol. 24, pp. 1089–96, 2001.

[26] F. Ravelli, L. Faes, L. Sandrini, F. Gaita, R. Antolini, M. Scaglione, and G. Nollo, "Wave similarity mapping shows the spatiotemporal distribution of fibrillatory wave complexity in the human right atrium during paroxysmal and chronic atrial fibrillation," *J. Cardiovasc. Electrophysiol.*, vol. 16, pp. 1071–76, 2005.

[27] M. Masè, L. Faes, R. Antolini, M. Scaglione, and F. Ravelli, "Quantification of synchronization during atrial fibrillation by shannon entropy: validation in patients and computer model of atrial arrhythmias," *Physiol. Meas.*, vol. 26, pp. 911–923, 2005.

[28] S. Petrutiu, J. Ng, G. M. Nijm, H. Al-Angari, S. Swiryn, and A. V. Sahakian, "Atrial fibrillation and waveform characterization," *IEEE Eng. Med. Biol. Mag.*, vol. 25, pp. 23–30, 2006.

[29] L. Edenbrandt and O. Pahlm, "Vectorcardiogram synthesized from a 12-lead ECG: superiority of the inverse Dower matrix," *J. Electrocardiol.*, vol. 21, pp. 361–367, 1988.

[30] P. Rubel, I. Benhadid, and J. Fayn, "Quantitative assessment of eight different methods for synthesizing Frank VCGs from simultaneously recorded standard ECG leads," *J. Electrocardiol.*, vol. 24 (Suppl.), pp. 197–202, 1991.

# *Paper II*

# Right Atrial Organization and Wavefront Analysis in Atrial Fibrillation

**Abstract**

The purpose of this study was to develop techniques to quantify the propagation pattern of the electrical activation during atrial fibrillation (AF) along a one-dimensional catheter. Taking intra-atrial signal organization aspects into account, the atrial activations are detected and combined into wavefronts. Parameters describing wavefront consistency and activation order along the catheter are defined, and the relationship of wavefront consistency to body surface parameters, namely AF frequency and exponential decay, is investigated.

The database consisted of 26 10-s recordings from patients during drug-refractory AF, in which 5 adjacent bipolar electrograms from a catheter in the right atrium were recorded. The 12-lead ECG was recorded simultaneously.

The degree of wavefront consistency provided insights into the temporal variability of the activation order, an aspect which was not reflected by the body surface parameters. However, AF frequency was able to distinguish between recordings with different degrees of intra-atrial signal organization ($p = 0.008$).

---


U. Richter, A. Bollmann, D. Husser and M. Stridh,
"Right Atrial Organization and Wavefront Analysis in Atrial Fibrillation",
in *Medical & Biological Engineering & Computing*, vol. 47, pp. 1237–1246, 2009.

# 1 Introduction

Atrial fibrillation is the most common arrhythmia in clinical practice and a costly public health problem. The exact mechanisms leading to the induction and perpetuation of AF are, however, still the subject of extensive research. For a long time, Moe's multiple wavelet hypothesis [1,2] has been the dominating theory explaining AF mechanisms. According to this theory, wavelets are propagating along varying routes throughout both atria, randomly activating the atrial tissue and leading to the complex electrical patterns observed during AF. More recent studies support another theory about "drivers" in the atria that trigger and sustain AF [3,4]. Whether these drivers are one or several foci firing at a short cycle length [5], or one or several reentrant circuits with short cycle length [6], remains uncertain. Often, such drivers have been observed to originate in the left atrium close to the pulmonary veins, but other origins have also been observed [7]. The role of the left atrium as a trigger of AF is supported by studies revealing left-to-right atrial frequency gradients, where a high frequency is considered to be closer to the source of the arrhythmia [8,9].

A number of approaches, either based on invasive or on body surface signals, have been presented for quantifying the organization of atrial activity during AF. A common approach based on invasive signals is to quantify the synchronization between pairs of adjacent electrograms. For this purpose, linear methods, e.g., evaluation of the cross-correlation [10] or the mean-square error in the linear prediction between two electrograms [11], have been applied. Non-linear methods, e.g., using the cross-conditional entropy [12] or the correlation dimension and correlation entropy [13], have also been considered.

Other invasive studies evaluate organization and synchronization using detected activations instead of the signals themselves. By coupling the closest detected activations from pairs of adjacent electrograms, a delay sequence can be calculated. In order to evaluate the degree of synchronization, the size of the delays [14] and the distribution of the delays [15] have been employed. The latter study is based on the observation that when two atrial sites are repeatedly passed by a stable wavelet, the activations in both sites should be well synchronized and the delay distribution should be narrow. In case the two sites are passed by an unstable wavelet or more than one wavelet, the sites should be less synchronized and thus the delay distribution should be wider and more complex. The degree of synchronization showed significant differences for the three common AF types defined in Wells' classification [15,16]. A non-linear approach for detecting linear as well as non-linear coupling between two atrial sites based on their detected activations was presented in [17].

Atrial fibrillation is also studied using the surface ECG, where in most approaches it is necessary to first extract the atrial activity [18,19]. It has been

shown that the atrial fibrillatory frequency can be determined non-invasively, i.e., based on the extracted atrial activity, where the highest correlation has been shown between the AF frequencies in surface lead $V_1$ and the right atrial electrograms [20]. A sequential method for robust estimation of the AF frequency based on time-frequency analysis was presented in [21]. Additionally, this work implemented a parameter characterizing the general shape of the fibrillation waves and included quality evaluation of analyzed signal segments. The ability of the AF frequency to, e.g., characterize effects of antiarrhythmic drugs [22, 23] as well as to predict spontaneous termination of AF [24, 25] has been documented.

The purpose of the present study is to develop techniques for quantifying the electrical activation pattern during AF along a one-dimensional catheter as well as to investigate the potential relationship of the extracted parameters to established organization measures from body surface signals. The proposed method for wavefront analysis, which is described in detail in Section 2.1, is based on the detected activations in five adjacent bipolar electrograms. Close activations in different electrograms are combined into wavefronts, which are analyzed with respect to their consistency over time, resulting in the parameter wavefront consistency. Furthermore, a propagation profile, which reflects the predominant activation order along the catheter, is calculated from the wavefronts. In contrast to previous approaches that rely on analyzing the coupled activations from one pair of electrograms at a time, our approach includes activations from more than two electrograms, thus providing insight into the propagation behavior along a larger part of the catheter. Measures of intra-atrial signal organization which are based on time-frequency analysis are employed to assure the reliability of the analysis. In detail, the distinctness of a harmonic spectrum and the fibrillatory frequency dispersion between the electrograms are considered. The novel parameter wavefront consistency is related to parameters calculated using body surface signals, the last-mentioned being described in Section 2.2. For comparative purposes, cross-correlation analysis between entire electrograms is also implemented, see Section 2.3.

# 2 Methods

## 2.1 Wavefront analysis

An overview of the proposed wavefront analysis is given in the block diagram in Fig. 1. Initially, analysis of the intra-atrial signal organization and detection of atrial activations are performed independently for each of the $N$ recorded electrograms. Based on the outcome of the intra-atrial signal organization

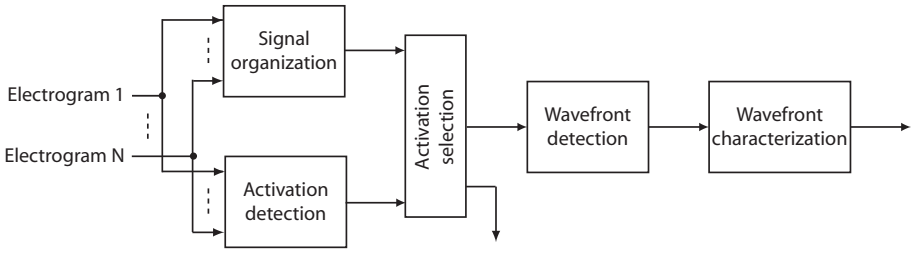


**Figure 1:** Block diagram of the method for wavefront analysis. The detected activations are selected for further analysis based on the outcome of the signal organization block.

analysis, the detected activations are selected for wavefront detection. The final step characterizes the detected wavefronts.

### Intra-atrial signal organization

A decreasing intra-atrial signal organization is indicated by electrograms in which it is difficult to distinguish between discrete activations. In addition, a high dispersion of the atrial fibrillatory frequency between the electrograms may be an indicator of that the recording sites are influenced by different wavelets. In order to evaluate the degree of intra-atrial signal organization, a logarithmic time-frequency distribution is employed, resulting in one spectrum per second, see Section 2.2. The position of the dominant spectral peak in the 3 to 9 Hz range, as well as the ratio between the power of this peak including its harmonics and the total spectral power, denoted by $\rho$, are calculated [26]. Furthermore, the standard deviation of the dominant frequencies between the electrograms, denoted by $\sigma_f$, is calculated for each second.

### Activation detection

For activation detection, the atrial signals are preprocessed using a standard procedure including bandpass filtering (40–250 Hz, order 40, Kaiser window), rectification, and lowpass filtering (FIR, 0–20 Hz, order 40, Kaiser window) [10]. Threshold detection is used to determine the positions of the activations. The threshold starts at the time point of the previously detected activation and is adapted to the amplitudes of preceding detections using exponential averaging. For activation intervals that are longer than 1.5 times the median distance between all detected activations, the threshold detection is repeated with a

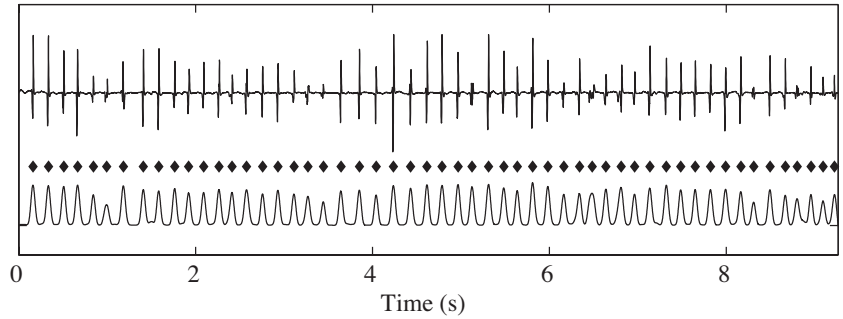


**Figure 2:** An example of activation detection with the original and preprocessed electrogram (top and bottom, respectively). The detected activations are marked with dots.

slightly lower threshold [27]. Additionally, a blanking period of 50 ms is introduced after each detected activation in order to prevent multiple detections. An example of the performance of the activation detection analysis is shown in Fig. 2. In the following, the $j$th detected activation in the $i$th electrogram will be denoted by $t_{i,j}$.

### Activation selection

The detected activations are selected for further analysis based on the outcome of the intra-atrial signal organization analysis, which resulted in one spectrum per second for each electrogram. In order for the activations during 1 s in an electrogram to be selected, the standard deviation $\sigma_f$ is required to be below 0.5 Hz, and the power ratio $\rho$ must exceed 0.3. The latter requirement can be interpreted as a verification of that the power spectrum has a distinct peak at the dominating frequency as well as a distinct harmonic pattern. If less than 3 consecutive seconds of a recording have fulfilled these criteria in all electrograms, the entire recording is regarded to have a too low intra-atrial signal organization for wavefront analysis.

### Wavefront detection

The wavefront detection is based on coupling of the activations of two adjacent electrograms at a time. The algorithm is initialized with a matrix $\mathbf{W}_1$ which has one row for each electrogram and contains the $M_1$ activation times of the

first electrogram in the first row:

$$\mathbf{W}_1 = \begin{bmatrix} t_{1,1} & t_{1,2} & \cdots & t_{1,M_1} \\ 0 & 0 & \cdots & 0 \\ \vdots & \vdots & & \vdots \\ 0 & 0 & \cdots & 0 \end{bmatrix}. \tag{1}$$

The $M_2$ activations of the second electrogram are then successively coupled to the activations in the first electrogram according to the following general rule: The $j$th activation of the $i$th electrogram is added at column $k$ that yields

$$k = \arg\min_l(|t_{i,j} - t_{i-1,l}| \ \leq \ \alpha), \qquad i \ > \ 1, \tag{2}$$

i.e., $t_{i,j}$ is coupled to the closest activation $t_{i-1,l}$ within the range $t_{i,j} \pm \alpha$. This approach is based on the assumption that two activations from two close recordings sites, that are closely spaced in time, are likely to belong to the same activation wavefront [14]. The parameter $\alpha$ is for each recording chosen individually as

$$\alpha = 0.25\frac{1}{f_{RA}}, \tag{3}$$

where $f_{RA}$ is the average fibrillatory frequency in the right atrium, see Section 2.2. This choice is based on the observation that the temporal distance between two successive activations in one electrogram can be estimated as the inverse of $f_{RA}$, while the temporal distance between two activations in adjacent electrograms that belong to the same activation wavefront should be considerably shorter.

In case there is an activation in the first bipolar electrogram, e.g., $t_{1,2}$, which does not satisfy Eq. (2) for any of the $t_{2,j}$, the corresponding place in the second row of the matrix remains zero. In the opposite case when no $t_{1,k}$ can be found for, e.g., $t_{2,M_2-1}$, a new column is inserted into the matrix,

$$\mathbf{W}_2 = \begin{bmatrix} t_{1,1} & t_{1,2} & t_{1,3} & t_{1,4} & \cdots & 0 & t_{1,M_1} \\ t_{2,1} & 0 & t_{2,2} & t_{2,3} & \cdots & t_{2,M_2-1} & t_{2,M_2} \\ 0 & 0 & 0 & 0 & \cdots & 0 & 0 \\ \vdots & \vdots & \vdots & \vdots & & \vdots & \vdots \\ 0 & 0 & 0 & 0 & \cdots & 0 & 0 \end{bmatrix}. \tag{4}$$

The activations of the remaining electrograms are processed in a similar manner, resulting in the matrix $\mathbf{W}_N$. In the present study, a wavefront is defined as complete if it contains one activation from each bipolar electrogram, i.e.,

column $j$ in matrix $\mathbf{W}_N$ is regarded as a complete wavefront when it contains non-zero values only. A separate matrix $\mathbf{W}$ is defined as

$$\mathbf{W} = [\mathbf{w}_1 \quad \mathbf{w}_2 \quad \dots \quad \mathbf{w}_M], \tag{5}$$

where each column $\mathbf{w}_j$ contains the activations of one of the $M$ complete wavefronts. In this matrix, each column has been centered around zero by subtracting the corresponding mean.

**Wavefront characterization**

The wavefront characterization is based on statistics calculated from the matrix $\mathbf{W}$. In order to assure reliable statistics, a minimum number of complete wavefronts, $M_{min}$, is required. This number is set to half the number of the expected wavefronts, i.e.,

$$M_{min} = 0.5\ T \cdot f_{RA}, \tag{6}$$

where $T$ is the length of the recording in seconds. For recordings in which $M$ exceeds this value, the quartiles of each row $i$ of the matrix $\mathbf{W}$ are computed. The first quartile of row $i$ is denoted $Q_{1,i}$ and includes the lowest 25% of the data. The second quartile of row $i$ is denoted $Q_{2,i}$ and divides the data set in half, i.e., the median. Similarly, the third quartile of row $i$ is denoted $Q_{3,i}$ and includes the highest 25% of the data. The difference between the upper and lower quartile is called interquartile range, $\bar{Q}_i = Q_{3,i} - Q_{1,i}$.

The mean of all $\bar{Q}_i$ defines the wavefront consistency, denoted by $C_{\bar{Q}}$. In recordings with consistent wavefronts, $C_{\bar{Q}}$ will take small values, while it results in larger values in recordings with inconsistent wavefronts.

Furthermore, the medians $Q_{2,i}$ can together be interpreted as the median wavefront $\bar{\mathbf{w}}$ or the propagation profile. The propagation profile allows analysis of which recording site that in the median has been activated first, and how the electrical activity propagated to the other recording sites. The linearity of the propagation profile, denoted $L$, is defined by the quality of the fit of a line to $\bar{\mathbf{w}}$, and is evaluated by calculating $r^2$ that can take values between 0 and 1.

## 2.2 Time-frequency analysis

In this paper, our previously presented method for characterization of atrial signals [21] is used to analyze both the ECG and the intra-atrial recordings. A brief description of the method follows together with a description of the different preprocessing strategies which are needed for the ECG and intra-atrial recordings, respectively.

### Preprocessing

All ECG signals are preprocessed in order to suppress baseline wander and powerline interference. After beat detection and classification, spatiotemporal QRST cancellation is performed [18]. The residual ECG is again baseline filtered ($< 2.5$ Hz) for additional noise suppression. Finally, the signals are decimated to 50 Hz.

Similar to the ECG signals, all intra-atrial signals are preprocessed by removing baseline wander and powerline interference. Rectification, amplitude compression using a hard limiter, and lowpass filtering (IIR, 0–25 Hz) are then performed. As above, the signals are decimated to 50 Hz.

### Method description

The atrial signal characterization is based on time-frequency analysis using a logarithmic frequency scale. The signal is first divided into overlapping segments (2.56 s long). Short-time logarithmic Fourier analysis with a Hamming window is performed for each segment, producing one spectrum per second.

The frequency estimation is performed by matching each new spectrum to a so-called spectral profile, resulting in optimal frequency shift and amplitude scaling. The spectral profile is initialized as the spectrum of the first few seconds and is then continuously updated with a frequency-aligned version of the present spectrum using exponential averaging. In this way, the entire harmonic pattern is accounted for in the frequency estimation procedure and a representation of the harmonic structure is contained in the spectral profile. The usage of the logarithmic frequency scale is motivated by that it allows the alignment of two harmonic spectra with different fundamentals. The method produces an estimate of the average AF frequency $f_1$ based on the surface ECG lead $V_1$. Furthermore, the exponential decay of the harmonic magnitudes, $\gamma_1$, is extracted from the spectral profile and serves as a coarse measure of waveform morphology.

In contrast to body surface signals, intra-atrial signals have harmonic magnitudes in the same range as that of the fundamental. In order to assure that the fundamental of the spectral profile will be matched to the fundamental of each spectrum, the method is slightly adjusted for intra-atrial signals by applying a linearly decreasing weighting function to each logarithmic spectrum. From the intra-atrial signals, the average fibrillatory frequency in the right atrium, $f_{RA}$, is calculated as the temporal and spatial frequency average of all intra-atrial signals.

## 2.3 Cross-correlation analysis

Cross-correlation analysis is implemented for comparison to the propagation profile $\bar{\mathbf{w}}$ which is calculated by the proposed wavefront characterization method. The cross-correlation function is calculated between one reference electrogram and all other electrograms [10]. The reference is chosen as the middle electrogram in order to keep the spatial distance to the reference short for all electrograms. The time-lag of the absolute peak in each function serves as an estimate of the average delay between the activations of the two electrograms. For the reference electrogram itself, the average delay is set to zero. The analysis thus results in one delay per electrogram, which are saved in the vector $\bar{\mathbf{w}}_{cc}$.

## 2.4 Statistical analysis

The correlation between different parameters is calculated using the Pearson correlation coefficient $r$ and related $p$-value. Furthermore, parameters in different groups of patients are compared using the one-sided Kolmogorov-Smirnov test. A $p$-value $< 0.05$ is considered statistically significant. All parameters are given in mean $\pm$ standard deviation.

## 2.5 Database

The method was evaluated on a database of 26 recordings (24 male, 2 female) from patients with drug-refractory AF who underwent pulmonary vein catheter ablation and presented in AF at the beginning of the procedure. The mean age was 56$\pm$11 years, and AF duration was 2.7$\pm$3.5 months. Underlying heart diseases were systemic hypertension (8 patients), coronary artery disease (2 patients), and idiopathic dilated cardiomyopathy (2 patients), whereas 14 patients had lone AF. Oral anticoagulants were discontinued for 4 days, and all antiarrhythmic drugs except for amiodarone 5 plasma half-lives, before the procedure.

Electrophysiological atrial studies were performed using a dual decapolar catheter (Cordis Webster Deflectable Halo) that was placed in the right atrium. Ten bipolar electrodes (H1/H2, H3/H4, ..., H19/H20, in the following denoted by H1, H3, ..., H19) were possible to measure, where the lower bipolar electrodes at the distal end of the catheter were situated in the low lateral right atrium, and H13 approximately recorded the atrial activity in the high septal right atrium. In each patient, that combination of five adjacent bipolar electrograms that showed the strongest activity was chosen for analysis. These were H5 to H13 in 18 patients, H7 to H15 in 3 patients, H9 to H17 in 4 patients, and

H11 to H19 in one patient. During the ablation procedure, 12-lead ECG and intra-atrial electrograms were recorded and stored using a commercial recording system (Bard EP Lab System Duo, Billerica, USA). All recordings were of 10 seconds duration and sampled with 1 kHz.

# 3 Results

**Examples of wavefront analysis**

The performance of the proposed method is illustrated by three representative examples. The first example shows a recording with highly consistent wavefronts over time and a non-linear propagation profile, see Fig. 3. The electrograms H11 to H19 were chosen for analysis and are plotted together with the complete detected wavefronts in Fig. 3(a). The frequency trends of all electrograms are plotted in Fig. 3(b). The electrograms show frequency trends that slightly increase over the interval, with a small frequency dispersion between the electrograms.

Figure 3(c) summarizes the statistics of the complete wavefronts such that each boxplot belongs to one row of $\mathbf{W}$ and thus to activations of one electrogram. The vertical lines of the boxes are given (from left to right) by the lower quartiles $Q_{1,i}$, the medians $Q_{2,i}$, and the upper quartiles $Q_{3,i}$, i.e., the width of the boxes themselves reflect the interquartile ranges $\bar{Q}_i$. Thus, Fig. 3(c) illustrates all measures that the parameters $C_{\bar{Q}}$ and $L$ are based on, including the propagation profile $\bar{\mathbf{w}}$. In the current example, the wavefronts are highly consistent, as the boxes are narrow, and no outliers exist. Furthermore, the first activation occurs consistently at the recording site of H13. The activation wavefront then propagates in both directions along the catheter. For this recording, $C_{\bar{Q}}$ yields the low value of 10 ms, indicating the consistency of the wavefronts, and $L = 0.19$, indicating a non-linear propagation profile. For comparison, the delay vector $\bar{\mathbf{w}}_{cc}$ calculated using cross-correlation analysis is shown in Fig. 3(d).

Three seconds of the recorded electrograms H7 to H15 of the second example are plotted together with the detected wavefronts from matrix $\mathbf{W}_5$ in Fig. 4. The plots show that the activations of H7 and H9 occur regularly and synchronized, which is also true for the activations of the electrograms H11, H13, and H15. However, whether there is a coupling between these two groups is difficult to determine because of the large delays between the activations in H9 and H11. This is reflected by the wavefront detection, which did result in only a few complete wavefronts, but mostly wavefronts that contain either activations from H7 and H9 or from H11, H13, and H15. The number of complete detected wavefronts $M$ did not exceed $M_{min}$, and therefore wavefront

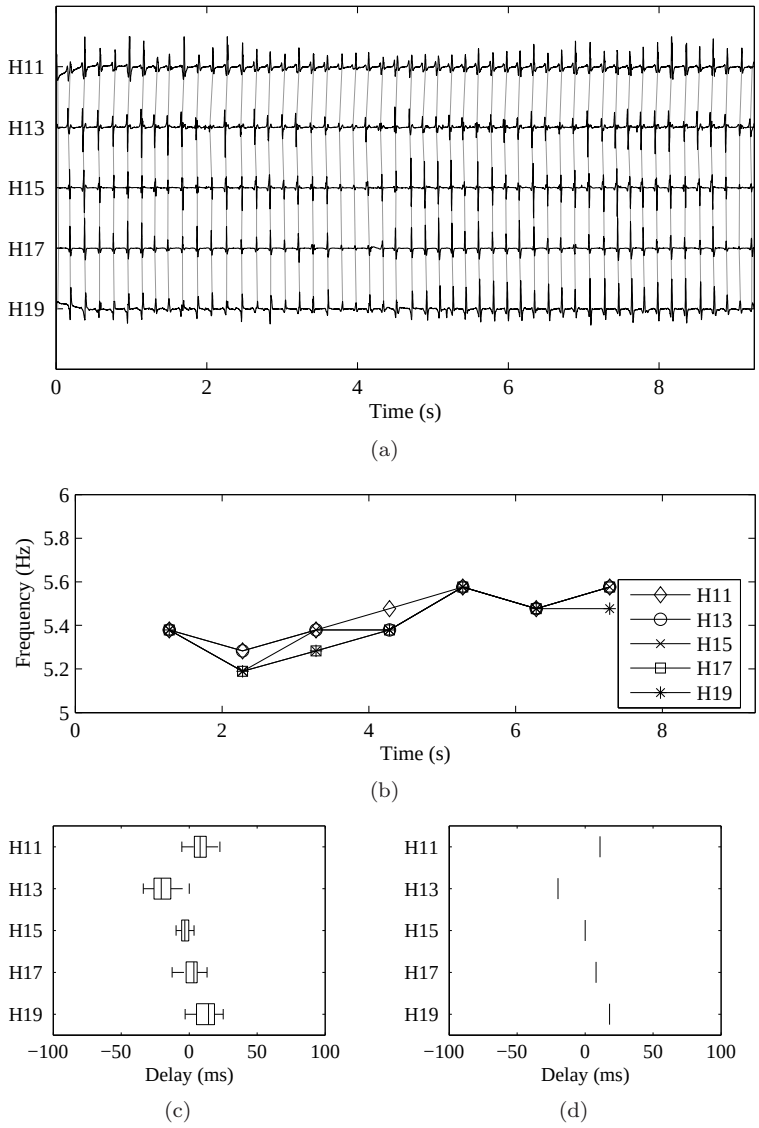


**Figure 3:** Example of a recording with highly consistent wavefronts and a non-linear propagation profile. (a) The original electrograms with the complete wavefronts. (b) Intra-atrial frequency trends. (c) Illustration of the statistics of each row of $\mathbf{W}$. (d) The delay vector $\bar{\mathbf{w}}_{cc}$ calculated using cross-correlation analysis.

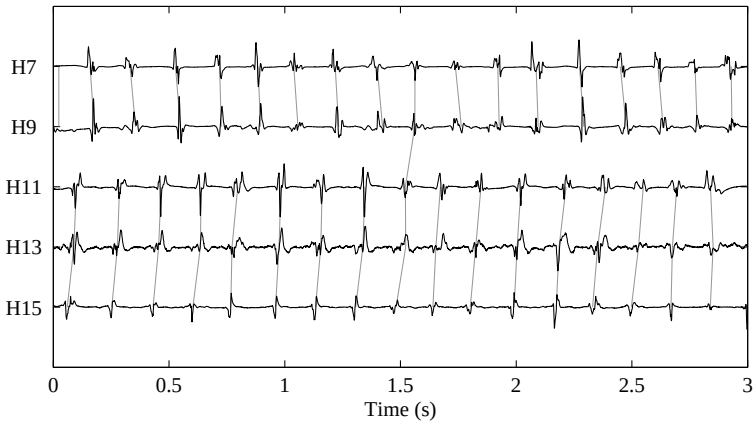


**Figure 4:** Three seconds of the original electrograms with the detected wavefronts in a recording in which electrogram groups H7/H9 and H11/H13/H15 seem not to be coupled.

characterization was not performed.

In the third example, the electrograms H9 to H17 were chosen for analysis, see Fig. 5(a). During the displayed 3 s, the activation order of the wavefronts is shifting, i.e., H17 is in the beginning activated last and at the end first. The wavefront consistency parameter $C_{\bar{Q}}$ which is based on the entire recording yields 18 ms and reflects this inconsistency of the activation order. The boxplots in Fig. 5(b) show that the propagation profile $\bar{\mathbf{w}}$ of the entire recording reflects the case when H17 is activated first and that the case when H17 is activated last occurs less often. The linearity of the propagation profile $L$ is 0.88. As a comparison, Fig. 5(c) shows $\bar{\mathbf{w}}_{cc}$ calculated using cross-correlation analysis.

### Database results

Intra-atrial signal organization divided the database into one group of 9 recordings, which had a too low degree of intra-atrial signal organization for wavefront analysis, and a group of 17 recordings with a sufficient degree of intra-atrial signal organization. In the latter group, 11 recordings consisted of the electrograms H5 to H13, three of H7 to H15, two of H9 to H17, and one of H11 to H19. Wavefront detection was performed for 7.9±1.5 s for these 17 recordings and resulted in 34±13 complete wavefronts per recording. In 2 of these 17 recordings, the number of complete wavefronts $M$ did not exceed $M_{min}$, and thus wavefront characterization was performed in 15 recordings.

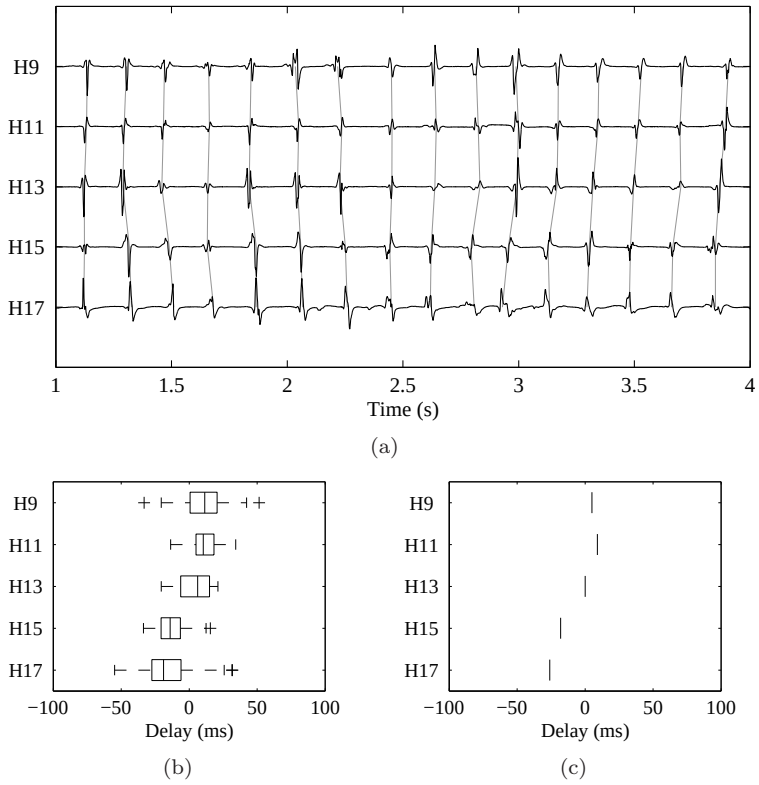


**Figure 5:** (a) Three seconds of the original electrograms with the complete wavefronts, illustrating a change in the activation order. (b) Illustration of the statistics of each row of $\mathbf{W}$ based on the entire recording. (c) The delay vector $\bar{\mathbf{w}}_{cc}$ calculated using cross-correlation analysis.

Figure 6 shows the distribution of the body surface parameters AF frequency $f_1$ (6.1±0.8 Hz) and exponential decay $\gamma_1$ (1.4±0.3) for the entire database. No significant correlation between these two parameters was found. However, the plot shows that when compared to recordings with a sufficient degree of intra-atrial signal organization, the majority of the recordings with a too low degree of intra-atrial signal organization exhibit a higher AF frequency, a higher exponential decay, or both. For AF frequency, a significant difference was found between the two groups of recordings with a too low and a sufficient degree of intra-atrial signal organization ($f_1$ = 6.6±1.0 Hz/5.8±0.5 Hz,

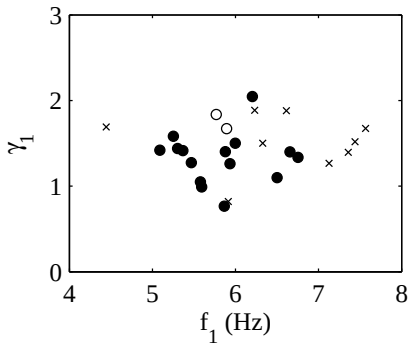


**Figure 6:** Distribution of exponential decay $\gamma_1$ versus AF frequency $f_1$. Recordings with a too low degree of intra-atrial signal organization are marked with a cross. Recordings with a sufficient degree of intra-atrial signal organization are marked with a circle, which is filled if the number of complete wavefronts $M$ did exceed $M_{min}$, and empty otherwise.

$p = 0.008$). The significant difference did also remain in the case when the two recordings in which $M$ did not exceed $M_{min}$ was removed from the group of recordings with a sufficient degree of intra-atrial signal organization ($f_1 = 6.6\pm1.0$ Hz/$5.8\pm0.5$ Hz, $p = 0.014$). For the exponential decay a significant difference between the groups could only be found in the latter case ($\gamma_1 = 1.5\pm0.3/1.4\pm0.3$, $p = 0.082$ and $\gamma_1 = 1.5\pm0.3/1.3\pm0.3$, $p = 0.026$, respectively).

Wavefront characterization resulted in a wavefront consistency $C_{\bar{Q}}$ of $15.1\pm5.6$ ms. Wavefront consistency was not reflected by the body surface parameters, since no significant correlation was found between $C_{\bar{Q}}$ and $f_1$ or $\gamma_1$, see also Fig. 7(a) and (b), respectively.

The linearity of the propagation profile $L$ yielded $0.74\pm0.31$. Furthermore, the Euclidean norm between the propagation profile $\bar{\mathbf{w}}$ and the delay vector $\bar{\mathbf{w}}_{cc}$ calculated using cross-correlation analysis was, after subtracting their respective mean values, found to $7.8\pm5.9$ ms.

# 4 Discussion

During ablation procedures it is of interest to obtain insights into the propagation pattern of the electrical activity in the atrial area that is covered by one or several catheters. In detail, the propagation pattern may be analyzed in terms of the site where the first activation occurs, how the electrical activity

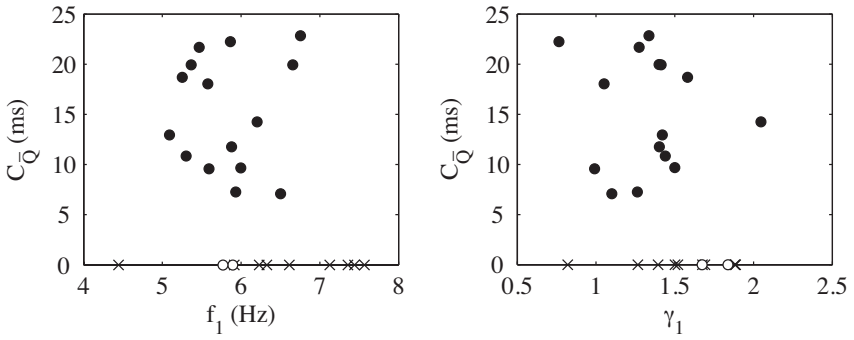


(a) (b)

**Figure 7:** (a) Distribution of $C_{\bar{Q}}$ versus AF frequency $f_1$. (b) Distribution of $C_{\bar{Q}}$ versus the exponential decay $\gamma_1$. Recordings with a too low degree of intra-atrial signal organization are marked with a cross and assigned $C_{\bar{Q}} = 0$. Recordings with a sufficient degree of intra-atrial signal organization are marked with a circle, which is filled if the number of complete wavefronts $M$ did exceed $M_{min}$, and empty otherwise. The latter recordings are also assigned a $C_{\bar{Q}}$ value of 0.

propagates in the recorded area, and how consistent this propagation pattern is, see, e.g., [28]. For this reason, the present approach takes the coupling of the closest activations from two recording sites one step further: After successively applying the coupling of activations to pairs of adjacent electrograms, a natural advancement is to further combine couples of activations that have one activation in common into wavefronts. This approach is, to our knowledge, the first that provides insight into the propagation pattern of the electrical activity along a catheter, including its consistency over time.

In AF, activation detection becomes increasingly difficult with a decreasing degree of organization in the intra-atrial signals. In order to evaluate the degree of organization of the signals, a frequency domain measure has been employed. This measure is similar to the one used in [26], where it was shown to be helpful when determining the appropriate time for successful defibrillation. In order to both determine the optimal defibrillation time and the optimal atrial site for defibrillation, the continuous wavelet transform (CWT) has been proposed [29]. The CWT is applied to each signal, and the degree of organization is determined from a measure related to the number of CWT coefficients needed to represent the signal. This approach, which was introduced to increase defibrillation efficiency, underlines similar to the discussions on ablation guidance

the need for methods that are able to analyze AF signals both over time and space. However, the approach based on the CWT concerns only one atrial signal at a time, and allows thus no conclusions about how the electrical activity propagates within the atria.

In this paper, the wavefront detection problem has been reduced to a problem involving only two recording sites at a time by processing adjacent pairs of electrograms, which accounts for the fact that the coupling between two atrial sites decreases with distance [10]. Previous approaches that involve two recording sites often couple the closest activations in time [14, 15, 30]. In the present approach, the distance between two coupled activations was restricted to a maximum that was individually calculated for each recording and based on the average atrial fibrillatory frequency. For an atrial fibrillatory frequency of, e.g., 6 Hz, this meant that the distance was restricted to about 42 ms. This restriction was introduced in order to prevent the coupling of activations that cannot clearly be assigned to each other, see, e.g., the activations in H9 and H11 in Fig. 4.

The present approach naturally involves the atrial activity from a larger part of the atrial tissue than approaches that are based on recordings from only two atrial sites, thus increasing the likelihood that more than one propagating wavelet is involved. During the analysis of intra-atrial signal organization, a measure of the dispersion of the atrial fibrillatory frequency between the electrograms was used to indicate whether multiple wavelets may be present in the recording area. While the atrial fibrillatory frequency can be similar in all electrograms, multiple wavelets may, however, still be involved. Figure 4(a) suggests that this can manifest itself in groups of electrograms between which a coupling of the activations seldom is found. Consequently, the number of complete detected wavefronts may be much smaller than the expected number that is calculated from the fibrillatory frequency and the length of the recording. In the future when a larger number of electrograms is involved in the analysis, the analysis of "incomplete" wavefronts should also be considered. However, in the present study, recordings with a majority of incomplete wavefronts were disregarded in wavefront characterization.

Wavefront consistency can be interpreted as the strength of coupling or synchronization between the recording sites. For the case when only two recording sites are involved in the analysis, different measures of the degree of synchronization have been proposed [14, 15]. To apply similar synchronization measures to the delays between the activations within the detected wavefronts is, however, not desirable as this would require the choice of a reference electrogram. Besides of that no delay distribution would be available for the reference site, the results would also vary based on which site that is chosen as a reference. In order to avoid problems related to the choice of a reference, the

present approach subtracts the mean from each detected wavefront, such that all wavefronts become centered around zero. This approach results in one delay distribution for each electrogram, each one being a stand-alone statistic interpretable independently from the others. Cross-correlation analysis also suffers from the disadvantage that a reference must be chosen. Furthermore, it is based on complete signal segments, rather than on single detected atrial activations that are coupled to wavefronts as in the present method. Consequently, a parameter such as wavefront consistency that reflects the variation of the wavefronts over time cannot be provided by cross-correlation analysis.

In the present study it was of interest to relate the results of the wavefront analysis to established parameters calculated from body surface signals. The wavefront consistency showed no significant correlation to the body surface parameters. A possible explanation is that both AF frequency and exponential decay are parameters that have been time averaged over the entire signal, thus not reflecting changes in the electrical activation pattern over time as the wavefront consistency does. However, the correlation between wavefront consistency and the standard deviation in AF frequency, reflecting the variation of the AF frequency over time, was neither significant.

The distribution of the parameters AF frequency and exponential decay were also evaluated between the groups of recordings with a too low and a sufficient degree of intra-atrial signal organization. AF frequency was found to be significantly lower in the recordings with a sufficient degree of intra-atrial signal organization compared to recordings with too low degree of intra-atrial organziation, see Fig. 6. This finding agrees with other studies that relate a lower AF frequency to a higher AF organization [31, 32].

The proposed method has been evaluated on a database consisting of recordings from a Halo catheter in the right atrium, where in each patient five adjacent bipolar electrograms were chosen. However, the method is not restricted to this type of catheter or to recordings from the right atrium, but can easily be adapted to other one-dimensional catheters, e.g., from the coronary sinus. Being aware of the underlying anatomy and distance between the recording sites, even electrograms from different catheters could be used as input to the analysis. A limitation of the database is that the five bipolar electrograms extracted from the recording system are not identical in all recordings, but vary between four combinations. It would be desirable to evaluate the method on a database with more homogenous data as well as a larger number of recording sites.

## 5 Conclusions

The present study showed that it is possible to detect wavefronts, reflecting the propagation pattern of the electrical activity during AF along a one-dimensional catheter, when taking intra-atrial signal organization aspects into account. Methods were provided in order to analyze the detected wavefronts regarding their consistency over time as well as the activation order along the catheter. The degree of wavefront consistency provided insights into the temporal variability of the activation order, an aspect which was not reflected by the body surface parameters AF frequency and exponential decay. However, AF frequency was able to distinguish between recordings with different degrees of intra-atrial signal organization.

## References

[1] G. Moe, "On the multiple wavelet hypothesis of atrial fibrillation," *Arch. Int. Pharmacodyn. Ther.*, vol. 140, pp. 183–188, 1962.

[2] M. A. Allessie, W. J. Lammers, F. I. Bonke, and J. M. Hollen, "Experimental evaluation of Moe's multiple wavelet hypothesis of atrial fibrillation," in *Cardiac Electrophysiology and Arrhythmias* (D. Zipes and J. Jaliff, eds.), pp. 265–275, Grune & Stratton, Orlando, Florida, 1985.

[3] M. Haïssaguerre, P. Jaïs, D. Shah, A. Takahashi, M. Hocini, G. Quiniou, S. Garrigue, A. L. Mouroux, P. L. Métayer, and J. Clémenty, "Spontaneous initiation of atrial fibrillation by ectopic beats originating in the pulmonary veins," *N. Engl. J. Med.*, vol. 339, pp. 659–666, 1998.

[4] R. Mandapati, A. Skanes, J. Chen, O. Berenfeld, and J. Jalife, "Stable microreentrant sources as a mechanism of atrial fibrillation in the isolated sheep heart," *Circulation*, vol. 101, pp. 194–199, 2000.

[5] T. Arentz, L. Haegeli, P. Sanders, R. Weber, F. J. Neumann, D. Kalusche, and M. Haïssaguerre, "High-density mapping of spontaneous pulmonary vein activity initiating atrial fibrillation in humans," *J. Cardiovasc. Electrophysiol.*, vol. 18, pp. 31–38, 2007.

[6] F. Atienza, J. Almendral, J. Moreno, R. Vaidyanathan, A. Talkachou, J. Kalifa, A. Arenal, J. P. Villacastín, E. G. Torrecilla, A. Sánchez, R. Ploutz-Snyder, J. Jalife, and O. Berenfeld, "Activation of inward rectifier potassium channels accelerates atrial fibrillation in humans: evidence for a reentrant mechanism," *Circulation*, vol. 114, pp. 2434–42, 2006.

[7] H. Oral, "Mechanisms of atrial fibrillation: lessons from studies in patients," *Prog. Cardiovasc. Dis.*, vol. 48, pp. 29–40, 2005.

[8] M. Mansour, R. Mandapati, O. Berenfeld, J. Chen, F. Samie, and J. Jalife, "Left-to-right gradient of atrial frequencies during acute atrial fibrillation in the isolated sheep heart," *Circulation*, vol. 103, pp. 2631–36, 2001.

[9] S. Lazar, S. Dixit, F. Marchlinski, D. Callans, and E. Gerstenfeld, "Presence of left-to-right atrial frequency gradient in paroxysmal but not persistent atrial fibrillation in humans," *Circulation*, vol. 110, pp. 3181–86, 2004.

[10] D. Botteron and J. Smith, "A technique for measurement of the extent of spatial organization of atrial activation during atrial fibrillation in the intact human heart," *IEEE Trans. Biomed. Eng.*, vol. 42, pp. 579–586, 1995.

[11] H. J. Sih, D. P. Zipes, E. J. Berbari, and J. E. Olgin, "A high-temporal resolution algorithm for quantifying organization during atrial fibrillation," *IEEE Trans. Biomed. Eng.*, vol. 46, pp. 440–450, 1999.

[12] L. T. Mainardi, V. D. Corino, L. Lombardi, C. Tondo, M. Mantica, F. Lombardi, and S. Cerutti, "Linear and nonlinear coupling between atrial signals. Three methods for the analysis of the relationships among atrial electrical activities in different sites.," *IEEE Eng. Med. Biol. Mag.*, vol. 25, pp. 63–70, 2006.

[13] F. Censi, V. Barbaro, P. Bartolini, G. Calcagnini, A. Michelucci, and S. Cerutti, "Non-linear coupling of atrial activation processes during atrial fibrillation in humans," *Biol. Cybern.*, vol. 85, pp. 195–201, 2001.

[14] V. Barbaro, P. Bartolini, G. Calcagnini, F. Censi, and A. Michelucci, "Measure of synchronisation of right atrial depolarisation wavefronts during atrial fibrillation," *Med. Biol. Eng. Comp.*, vol. 40, pp. 56–62, 2002.

[15] M. Masè, L. Faes, R. Antolini, M. Scaglione, and F. Ravelli, "Quantification of synchronization during atrial fibrillation by shannon entropy: validation in patients and computer model of atrial arrhythmias," *Physiol. Meas.*, vol. 26, pp. 911–923, 2005.

[16] J. L. Wells, R. B. Karp, N. T. Kouchoukos, W. A. H. Maclean, T. N. James, and A. L. Waldo, "Characterization of atrial fibrillation in man: studies following open-heart surgery," *PACE*, vol. 1, pp. 426–438, 1978.

[17] F. Censi, V. Barbaro, P. Bartolini, G. Calcagnini, A. Michelucci, G. F. Gensini, and S. Cerutti, "Recurrent patterns of atrial depolarization during atrial fibrillation assessed by recurrence plot quantification," *Ann. Biomed. Eng.*, vol. 28, pp. 61–70, 2000.

[18] M. Stridh and L. Sörnmo, "Spatiotemporal QRST cancellation techniques for analysis of atrial fibrillation," *IEEE Trans. Biomed. Eng.*, vol. 48, pp. 105–111, 2001.

[19] P. Langley, J. J. Rieta, M. Stridh, J. Millet, L. Sörnmo, and A. Murray, "Comparison of atrial signal extraction algorithms in 12-lead ECGs with atrial fibrillation," *IEEE Trans. Biomed. Eng.*, vol. 53, pp. 343–346, 2006.

[20] M. Holm, S. Pehrson, M. Ingemansson, L. Sörnmo, R. Johansson, L. Sandhall, M. Sunemark, B. Smideberg, C. Olsson, and S. B. Olsson, "Noninvasive assessment of the atrial cycle length during atrial fibrillation in man: introducing, validating and illustrating a new ECG method," *Cardiovasc. Res.*, vol. 38, pp. 69–81, 1998.

[21] M. Stridh, L. Sörnmo, C. J. Meurling, and S. B. Olsson, "Sequential characterization of atrial tachyarrhythmias based on ECG time-frequency analysis," *IEEE Trans. Biomed. Eng.*, vol. 51, pp. 100–114, 2004.

[22] A. Bollmann, N. Kanuru, K. McTeague, P. Walter, D. B. DeLurgio, and J. Langberg, "Frequency analysis of human atrial fibrillation using the surface electrocardiogram and its response to ibutilide," *Am. J. Cardiol.*, vol. 81, pp. 1439–45, 1998.

[23] D. Husser, M. Stridh, L. Sörnmo, C. Geller, H. U. Klein, S. B. Olsson, and A. Bollmann, "Time–frequency analysis of the surface electrocardiogram for monitoring antiarrhythmic drug effects in atrial fibrillation," *Am. J. Cardiol.*, vol. 95, pp. 526–28, 2005.

[24] F. Nilsson, M. Stridh, A. Bollmann, and L. Sörnmo, "Predicting spontaneous termination of atrial fibrillation using the surface ECG," *Med. Eng. & Physics*, vol. 28, pp. 802–806, 2006.

[25] S. Petrutiu, A. V. Sahakian, and S. Swiryn, "Abrupt changes in fibrillatory wave characteristics at the termination of paroxysmal atrial fibrillation in humans," *Europace*, vol. 9, pp. 466–470, 2007.

[26] T. Everett, R. Moorman, L. Kok, J. Akar, and D. Haines, "Assessment of global atrial fibrillation organization to optimize timing of atrial defibrillation," *Circulation*, vol. 103, pp. 2857–61, 2001.

[27] L. Sörnmo and P. Laguna, *Bioelectrical Signal Processing in Cardiac and Neurological Applications*. Amsterdam: Elsevier (Academic Press), 2005.

[28] M. Haïssaguerre, M. Hocini, P. Sanders, Y. Takahashi, M. Rotter, F. Sacher, T. Rostock, L.-F. Hsu, A. Jonsson, M. O'Neill, P. Bordachar, S. Reuter, R. Roudaut, J. Clémenty, and P. Jaïs, "Localized sources maintaining atrial fibrillation organized by prior ablation," *Circulation*, vol. 112, pp. 616–625, 2006.

[29] K. W. Lee, T. H. Everett, H. T. Ilhan, I. Linscott, and J. E. Olgin, "Feature extraction of the atrial fibrillation signal using the continuous wavelet transform," in *Proc. 26th Annual Intern. Conf. IEEE EMBS*, pp. 275–278, 2004.

[30] L. Faes and F. Ravelli, "A morphology-based approach to the evaluation of atrial fibrillation organization," *IEEE Eng. Med. Biol. Mag.*, vol. 26, pp. 59–67, 2007.

[31] K. Konings, C. Kirchhof, J. Smeets, H. Wellens, O. Penn, and M. A. Allessie, "High–density mapping of electrically induced atrial fibrillation in humans," *Circulation*, vol. 89, pp. 1665–80, 1994.

[32] A. Bollmann and F. Lombardi, "Electrocardiology in atrial fibrillation," *IEEE Eng. Med. Biol. Mag.*, vol. 25, pp. 15–23, 2006.

# *Paper III*

# A Novel Approach to Propagation Pattern Analysis in Intracardiac Atrial Fibrillation Signals

**Abstract**

The purpose of this study is to investigate propagation patterns in intracardiac signals recorded during atrial fibrillation (AF) using an approach based on partial directed coherence (PDC), which evaluates directional coupling between multiple signals in the frequency domain. The PDC is evaluated at the dominant frequency of AF signals and tested for significance using a surrogate data procedure specifically designed to assess causality. For significantly coupled sites, the approach allows also to estimate the delay in propagation. The method's potential is illustrated with two simulation scenarios based on a detailed ionic model of the human atrial myocyte as well as with real data recordings, selected to present typical propagation mechanisms and recording situations in atrial tachyarrhythmias. In both simulation scenarios the significant PDCs correctly reflect the direction of coupling and thus the propagation between all recording sites. In the real data recordings, clear propagation patterns are identified which agree with previous clinical observations. Thus, the results illustrate the ability of the novel approach to identify propagation patterns from intracardiac signals during AF, which can provide important information about the underlying AF mechanisms, potentially improving the planning and outcome of arrhythmia ablation.

---


U. Richter, L. Faes, A. Cristoforetti, M. Masè, F. Ravelli, M. Stridh and L. Sörnmo, "A Novel Approach to Propagation Pattern Analysis in Intracardiac Atrial Fibrillation Signals",
in *Annals of Biomedical Engineering*, 2010 (in press).

# 1 Introduction

The mechanisms leading to the induction and perpetuation of atrial fibrillation (AF), which is the most common arrhythmia in clinical practice, are still the subject of extensive research. The complex electrical pattern observed during AF has been explained with multiple wavelets that propagate along varying routes throughout the atria [1]. More recently, available data has also supported a 'focal' mechanism, according to which drivers or foci, mainly located in the pulmonary veins, trigger and sustain the propagation of the electrical activity in the atria [2–4]. These observations have led to increased interest in methods that analyze the atrial activity at multiple intracardiac sites, e.g., for the purpose of guiding the ablation catheter to the atrial sites at which the arrhythmia originates or which represent arrhythmia substrates. One approach to such guidance is to identify and ablate atrial sites with complex fractionated atrial electrograms [5]. Another approach is based on the identification of dominant frequency (DF) sites [6]. Despite a large number of follow-up studies, recent publications show that such approaches are still controversial [7, 8], and therefore further studies are needed to better understand the mechanisms of AF.

With the advancement of catheter technology, catheters that cover major parts of the atria and allow for simultaneous recording of a large number of electrograms have become available. This advancement makes it possible to perform spatiotemporal analysis of the mechanisms during AF, e.g., in order to characterize the propagation patterns of the electrical activity. The challenge of such analysis is to determine the interrelationship among all signals. In contrast, most approaches involve either individual signals or pairs of signals to quantify the electrical activity in terms of "organization". In the time domain, the proposed organization measures are often related to signal morphology or activation times [9, 10]. The approach of coupling activation times in adjacent pairs of signals [10] has recently been extended to more than two signals such that activation wavefronts can be detected [11]. While this may identify certain propagation patterns, a disadvantage of the method is its dependence on activation detection which becomes increasingly difficult with decreasing AF organization. Also, coupling of activations cannot be established in certain cases. These issues may be solved using frequency domain methods not requiring activation detection, such as the coherence function, which has been used to quantify AF organization based on pairs of electrograms [12]. While the coherence function can differentiate between non-fibrillatory rhythms, such as sinus rhythm and atrial flutter, and fibrillatory rhythms, i.e., AF, two major disadvantages have become apparent. Firstly, the coherence function cannot identify the direction of coupling between the signals, i.e., the direction in which the

electrical activity propagates. Secondly, the coherence function is only defined for pairs of signals. Thus, when more than two simultaneously recorded signals are to be analyzed, the coherence function is either calculated for all possible combinations of pairs of signals, or one particular signal has to be chosen as a reference on which the results strongly depend. A method that overcomes these disadvantages is therefore highly desirable.

Even though frequency domain methods quantifying the directional coupling among multiple signals have not been tested in AF studies, they have been developed in other fields, especially for the analysis of brain signals [13–15]. The methods are based on the fit of a multivariate autoregressive (MVAR) model to multichannel recordings, characterizing causal coupling between multiple signals. The spectral representation of the MVAR process can be employed to derive functions reflecting the causal coupling in the frequency domain, an example being the partial directed coherence (PDC) function which is obtained from decomposing the partial coherence [14, 15].

In the present study, we propose the PDC for the analysis of the propagation of the electrical activity within the atria during AF. In order to make the method suitable for intracardiac signals, a preprocessing procedure is performed before MVAR model fitting. The proposed approach for propagation pattern analysis offers several advantages compared to existing methods: Firstly, it quantifies the directional coupling and identifies the underlying propagation pattern between the recording sites by employing a multivariate approach that simultaneously evaluates all signals. Secondly, the method can handle an increasing number of recorded signals and does not require any knowledge on the relative positioning of the recording sites. These aspects are of special interest during electrophysiological studies performed, e.g., in connection to ablation procedures, where it is desirable to map larger parts of the atria in order to identify from which direction the electrical activity originates. Yet another advantage of the method is that the time delays between different recording sites can be estimated. Finally, the frequency domain implementation avoids certain difficulties that come with atrial activation detection.

The potential of the method will be illustrated with two simulation scenarios, modeling various propagation mechanisms in play during atrial tachyarrhythmia such as atrial flutter and AF, and real data recordings of atrial flutter and AF, acquired with either one- or two-dimensional catheters.

# 2 Methods

## 2.1 Preprocessing

The preprocessing consists of bandpass filtering (finite impulse response (FIR), 40–250 Hz, order 40, Kaiser window), rectification, and lowpass filtering (FIR, 0–20 Hz, order 40, Kaiser window) [16]. After the filtering, the sampling rate is decimated to 100 Hz, and the mean is subtracted from each electrogram.

In the time domain, the preprocessing results in signals with an amplitude proportional to the high-frequency components (40–250 Hz), which correspond to the rapid changes in amplitude characteristics of the activations. In the frequency domain, the preprocessing results in spectra with a pronounced fundamental frequency [17]. Figure 1 illustrates how the preprocessing emphasizes the rhythm in the signals as opposed to signal morphology by displaying five simultaneously recorded bipolar electrograms from the right atrium (RA) during AF both before and after preprocessing.

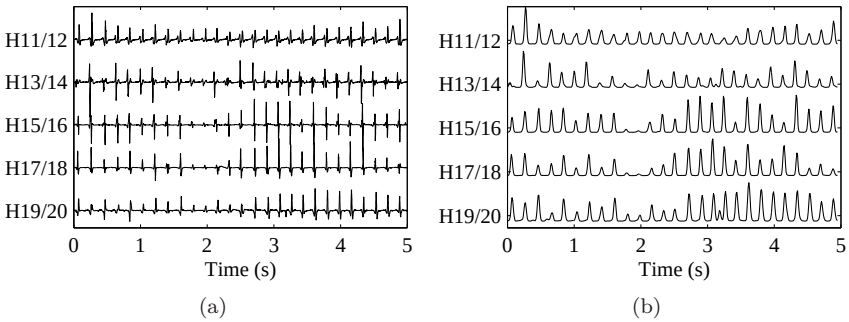


**Figure 1:** Preprocessing of five simultaneously recorded bipolar electrograms from the RA during AF. The amplitude scale is in arbitrary units. (a) Original electrograms. (b) Preprocessed electrograms.

## 2.2 Multivariate Autoregressive Modeling

Each set of $N$ simultaneous observations $\mathbf{x}(n) = [x_1(n) \cdots x_N(n)]^T$, obtained from different sites in the atria, is assumed to be represented by an MVAR model of order $m$

$$\mathbf{x}(n) = \sum_{k=1}^{m} \mathbf{A}_k \mathbf{x}(n-k) + \mathbf{w}(n), \tag{1}$$

where each $\mathbf{A}_k$ is an $N \times N$ matrix comprising the AR coefficients $a_{ij}(k)$, $i, j = 1, \ldots, N$, and $\mathbf{w}(n) = [w_1(n) \cdots w_N(n)]^T$ is a multivariate white noise process characterized by the diagonal covariance matrix $\mathbf{\Sigma}_w$, in which each diagonal element $\sigma_{jj}^2$ defines the variance of $w_j(n)$.

The PDC from $x_j(n)$ to $x_i(n)$ can be derived from factorization of the partial coherence function [14, 15], and is given by

$$\pi_{ij}(f) = \frac{\frac{1}{\sigma_{ii}} \bar{A}_{ij}(f)}{\sqrt{\sum_{k=1}^{N} \frac{1}{\sigma_{kk}^2} |\bar{A}_{kj}(f)|^2}}, \tag{2}$$

where $\bar{A}_{ij}(f)$ is an element of the matrix $\bar{\mathbf{A}}(f)$, which is based on the Fourier transform (FT) of the MVAR process in Eq. (1),

$$\bar{\mathbf{A}}(f) = \mathbf{I}_{N \times N} - \sum_{k=1}^{m} \mathbf{A}_k e^{-\jmath 2\pi f k}, \tag{3}$$

where $\mathbf{I}$ is the unity matrix. The definition in Eq. (2) is that of the generalized PDC [15], being especially useful in the case of widely different variances $\sigma_{jj}^2$. The denominator of the PDC serves as a normalization with respect to the source, i.e., $x_j(n)$, such that

$$\sum_{i=1}^{N} |\pi_{ij}(f)|^2 = 1 \tag{4}$$

and

$$0 \leq |\pi_{ij}(f)|^2 \leq 1. \tag{5}$$

Given this normalization, the value of the magnitude-squared PDC $|\pi_{ij}(f)|^2$ from $j$ to $i$ represents the strength of the direct coupling from $x_j(n)$ to $x_i(n)$ at frequency $f$, viewed in relation to the direct coupling strength of $x_j(n)$ to all other signals $x_k(n)$, $k \neq i$, at that frequency. For reasons of convenience, the magnitude-squared PDC $|\pi_{ij}(f)|^2$ is referred to as PDC in the following.

During AF, the PDC is of special interest in an interval centered around the DF of the source $x_j(n)$, here assumed to represent the mean atrial fibrillatory cycle length at the corresponding recording site. Thus, the integrated PDC is defined by [18]

$$\Pi_{ij}^2 = \frac{1}{2\Delta f} \int_{f_0 - \Delta f}^{f_0 + \Delta f} |\pi_{ij}(f)|^2 df, \tag{6}$$

where $f_0$ is the DF, corresponding to the highest peak in the 3–12 Hz range of the auto-spectrum of $x_j(n)$, denoted $S_{jj}(f)$, and $\Delta f$ is a parameter determining

the width of the integration interval. The integral is normalized such that, similar to the PDC, it ranges from 0 to 1, and thus represents the average coupling from $x_j(n)$ to $x_i(n)$ in the frequency range of interest. In case no obvious DF can be identified in signal $x_j(n)$, the corresponding $\Pi_{ij}^2$ is set to zero for all $i$. The auto-spectra $S_{jj}(f)$ are the diagonal elements in the power spectral density matrix of the MVAR process, defined as

$$\mathbf{S}(f) = \bar{\mathbf{A}}^{-1}(f)\mathbf{\Sigma}_w(\bar{\mathbf{A}}^{-1}(f))^H. \tag{7}$$

The time delay from $x_j(n)$ to $x_i(n)$, denoted $\Delta_{ij}$, can be estimated from the phase spectrum $\phi_{ij}(f)$ of the corresponding cross-spectral density [19],

$$S_{ij}(f) = |S_{ij}(f)|e^{j\phi_{ij}(f)}, \tag{8}$$

which is obtained from Eq. (7). The delay $\Delta_{ij}$ is equal to that value of $\delta$ which maximizes the integral, i.e.,

$$\Delta_{ij} = \arg\max_{\delta} \int_{f_0-\Delta f}^{f_0+\Delta f} \frac{C_{ij}(f)}{1 - C_{ij}(f)} \cos\left[\phi_{ij}(f) - 2\pi f\delta\right] df, \tag{9}$$

where $C_{ij}(f)$ is the magnitude-squared coherence spectrum defined as

$$C_{ij}(f) = \frac{|S_{ij}(f)|^2}{S_{ii}(f)S_{jj}(f)}. \tag{10}$$

The estimator in Eq. (9) evaluates the weighted goodness-of-fit of a line with slope $\delta$ to the phase spectrum over the frequency range of interest. The delay estimation is only computed when the corresponding integrated PDC is significant, see Sec. 2.4.

## 2.3 Model Identification and Selection

The AR coefficient matrices $\mathbf{A}_k$ are estimated using the least-squares (LS) method, and the optimal model order $m$ is determined by the Bayesian information criterion (BIC) [20]. The best model order was searched for in the range 1 to 15. The model order is chosen as that value of $m$ for which the minimum is reached, or, in case the BIC does not reach a minimum, an additional model selection criterion is defined where that value of $m$ is chosen for which the successive difference in BIC is smaller than 5% of the largest successive difference.

### 2.4 Surrogate Data Testing

The significance of the PDC $|\pi_{ij}(f)|^2$ is assessed separately for each coupling by means of a statistical approach based on surrogate data testing [21]. The method of surrogate data relies on computing the index of interest, i.e., the PDC $|\pi_{ij}(f)|^2$, both on the original time series $\mathbf{x}(n)$ and on a set of surrogate time series $\mathbf{y}^{(l)}(n) = [y_1^{(l)}(n) \cdots y_N^{(l)}(n)]^T$, $l = 1, \ldots, M$. The latter time series lacks by construction the investigated property, i.e., there is no direct causal coupling from $y_j^{(l)}(n)$ to $y_i^{(l)}(n)$. A statistical test is then applied to compare the values of the index of interest for the original series and for the set of surrogate series. The index is assumed to be significant if the original value lies above a certain percentile of the distribution of values obtained from the surrogates.

In detail, it is assumed that an MVAR model has been fitted to $\mathbf{x}(n)$, resulting in estimates of $\mathbf{A}_k, k = 1, \ldots, m$, and $\mathbf{\Sigma}_w$. To test the significance of the PDC, e.g., from $x_j(n)$ to $x_i(n)$, the $M$ surrogates $\mathbf{y}^{(l)}(n)$ are computed by repeatedly applying the following procedure (the surrogate index $l$ is omitted hereafter for simplicity). First, a new set of signals $\check{\mathbf{x}}(n)$ is computed using $N$ independent noise realizations ($\sim \mathcal{N}(\mathbf{0}, \mathbf{\Sigma}_w)$) as input to the MVAR model defined by $\check{\mathbf{A}}_k = \mathbf{A}_k$, with $\check{a}_{ij}(k) = 0$, $k = 1, \ldots, m$, implying that there is no direct coupling from $\check{x}_j(n)$ to $\check{x}_i(n)$. After calculating the FT of $\mathbf{x}(n)$ and $\check{\mathbf{x}}(n)$, i.e., $X_i(f) = |X_i(f)|e^{\jmath \angle X_i(f)}$ and $\check{X}_i(f) = |\check{X}_i(f)|e^{\jmath \angle \check{X}_i(f)}$, respectively, $i = 1, \ldots, N$, the FT of $\mathbf{y}(n)$ is defined as $Y_i(f) = |X_i(f)|e^{\jmath \angle \check{X}_i(f)}$, such that the absolute values of the FT of $\mathbf{y}(n)$ are identical to those of $\mathbf{x}(n)$ at each frequency, while the phase is altered such that there is no direct coupling from $y_j(n)$ to $y_i(n)$ at any frequency. Finally, the surrogate series $\mathbf{y}(n)$ is obtained by computing the inverse FT of $Y_i(f), i = 1, \ldots, N$.

The significance threshold $|\tilde{\pi}_{ij}(f)|^2$ is then, at each frequency, defined as the 95th percentile of the PDCs calculated from the $M$ surrogates, i.e., $|\pi_{ij}(f)|^2$ of the original signals is considered to be significant ($p < 0.05$), if it exceeds $|\tilde{\pi}_{ij}(f)|^2$. Similarly, the integrated PDC is calculated for each surrogate series, and the 95th percentile defines the significance threshold $\tilde{\Pi}_{ij}^2$: a significant direct coupling is said to exist from $x_j(n)$ towards $x_i(n)$ if $\Pi_{ij}^2 > \tilde{\Pi}_{ij}^2$.

## 3 Database

The database comprises simulated electrograms from two different simulation scenarios as well as electrograms from patients with atrial flutter and AF recorded with either one- or two-dimensional catheters.

### 3.1 Simulation Model

Computer simulations were performed employing the Courtemanche–Ramirez–Nattel (CRN) ionic model [22] in a monodomain formulation. The model, which has been specifically developed for the human atrial action potential, computes the cell transmembrane potential $V$ by the reaction-diffusion equation

$$\frac{\partial V}{\partial t} = \nabla \cdot \mathbf{D} \nabla V - \frac{I_{ion}}{C_m} + \frac{I_{st}}{C_m}, \tag{11}$$

where $I_{ion}$ is the total ionic current, $I_{st}$ is an external stimulus current, $C_m$ is the membrane capacitance, and $\mathbf{D}$ is the diffusion tensor. The total ionic current $I_{ion}$ consists of 12 separate contributions, which represent the ionic and pump currents and include reticular calcium handling. A detailed description of the currents and their representation can be found in [22].

The ionic model was implemented on a simplified anatomy, represented by a monolayer sphere with a diameter of 6 cm. The sphere was discretized into a triangular mesh comprising approximately 125.000 nodes, which resulted in a spatial resolution of about 300 $\mu$m. The diffusion tensor $\mathbf{D}$ was considered uniform and isotropic. The partial differential equations of the CRN model were solved by employing the forward non-standard Rush-Larsen integration scheme [23] for the reaction part, while a finite volume method for an irregular mesh [24], integrated with a standard forward Euler scheme, was used for the diffusion part. The integration time step was fixed to 0.1 ms, which was sufficiently small to guarantee the stability of both integration schemes.

Simulated bipolar electrograms corresponding to different simulation patterns were obtained by applying the current source approximation [25]. Specifically, the extracellular potential at spatial position $\mathbf{y}$ was computed according to

$$\varphi(\mathbf{y}) = \sum_{k=1}^{N_k} \frac{I_m^k}{||\mathbf{y}_k - \mathbf{y}||} \Omega_k, \tag{12}$$

where the sum is extended to all the $N_k$ nodes of the mesh, $I_m^k$ is the transmembrane current per unit area at node $k$, $\mathbf{y}_k$ is the position of node $k$, and $\Omega_k$ is the area corresponding to node $k$. In order to obtain bipolar electrograms, electrode pairs with an intra-electrode distance of 2 mm were placed at a distance of 0.5 mm from the surface of the sphere. Bipolar electrograms were computed as the difference between the extracellular signals recorded at the corresponding electrode pair. For each simulation pattern, 5-s signals were obtained with a sampling rate of 1 kHz and used for further validation of the method.

### 3.2 Simulation of Atrial Tachyarrhythmias

The first scenario is a simulation of atrial flutter, modeled as a reentry around an anatomical obstacle with a diameter of 1.3 cm. The diffusion coefficient was set to 0.3 $cm^2/s$. In order to induce reentrant activity, a single electrical impulse was delivered in proximity to the anatomical obstacle, while a temporary unidirectional conduction block was present. The subsequent removal of the block allowed the establishment of a self-sustained activation of the tissue. As shown in Fig. 2(a), the reentrant wave activated first the tissue at recording site S1, and subsequently passed by recording sites S2 to S5. The corresponding signals, obtained after stabilization of the reentrant activity, are displayed in Fig. 2(b).

The second scenario is a simulation of AF, mimicking multiple wavelet propagation in the presence of a regularly firing ectopic focus. Sustained AF was created starting from a configuration with two functional spiral reentries, which were initiated by a single electrical impulse delivered adjacent to a temporary line of block. Subsequently, the currents of the ionic model $I_{to}$, $I_{Ca,L}$, $I_{Kur}$, and $I_{Kr}$ (see [22] for definitions) were modified according to [25] in order to obtain a restitution curve which caused repeated spiral breakups and the formation of a multiple wavelet pattern. After 10 s of sustained AF, a point source firing with a period of 275 ms became active at the upper pole of the sphere. The diffusion coefficient was 0.2 $cm^2/s$ throughout the entire scenario. As shown in Fig. 2(c), the result is a regular propagation in proximity to the focus (site S1), which progressively deteriorates when entering the area dominated by the multiple wavelet behavior (lower part of the sphere). The simulated signals were obtained after the point source became active and are displayed in Fig. 2(d).

### 3.3 Electrograms from Patients with Atrial Arrhythmias

The first case is a recording from a patient with atypical left atrial flutter. Atrial bipolar electrograms were recorded with a decapolar catheter in the coronary sinus (CS). Five-second electrograms corresponding to the equally spaced bipolar electrodes CS1/2, CS5/6, CS9/10, and CS13/14 from distal to proximal CS were extracted for analysis, see Fig. 3. In the following, the electrograms from CS1/2 to CS13/14 are indexed by $i = 1, \ldots, 4$.

Two other cases comprise AF signals acquired with different mapping modalities, i.e., by a linear or a basket catheter, respectively. In the first patient with persistent AF, electrograms were recorded using a dual decapolar catheter (Cordis Webster Deflectable Halo) placed in the RA, with bipolar electrodes recording the atrial activity from the low lateral (H1/H2) to the septal wall (H19/20). H13/H14 recorded atrial activity in approximately the

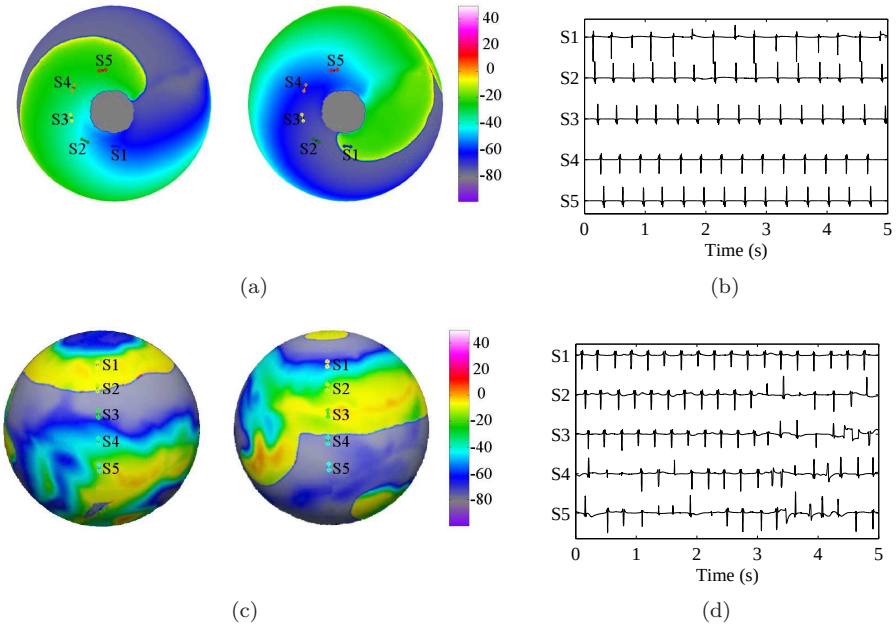


**Figure 2:** Illustration of the simulation scenarios: (a,c) Snapshots of the membrane voltage with the electrode positions indicated (snapshots are 120 ms apart) for the simulation of an anatomical reentry and the simulation of AF, respectively. (b,d) The electrograms corresponding to the simulation of an anatomical reentry and the simulation of AF, respectively. See text for further details.

high septal wall. Five-second electrograms corresponding to the five bipoles H11/12 to H19/20 in the septal wall, in the following indexed by $i = 1, \ldots, 5$, were chosen for further analysis, see Fig. 1(a).

In the second patient with paroxysmal AF, the electrophysiological study was performed with a multielectrode basket catheter (Constellation catheter, EP Technologies, Boston Scientific) in the RA. The basket catheter consisted of eight splines, each carrying eight equally spaced electrodes (4 mm inter-electrode distance). Thirty-two bipolar intracardiac electrograms were acquired by coupling adjacent pairs of electrodes (CardioLab System, 30–500 Hz [Prucka Engineering, Inc.]). In this patient, six electrodes had to be excluded because of poor signal to noise quality. From the recording of the remaining 26 electrodes, 5 s were chosen for analysis. A schematic representation of the recording positions and the original electrograms, illustrating varying degrees of signal

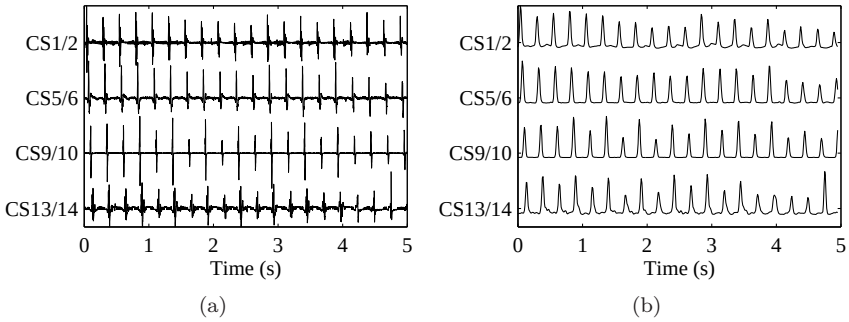


**Figure 3:** Electrograms from a patient with atrial flutter. (a) Original electrograms. (b) Preprocessed electrograms.

organization, are shown in Figs. 4(a) and (b), respectively.

All electrograms were digitized at a sampling rate of 1 kHz.

# 4 Results

The results were obtained for $f_\Delta$ set to 0.5 Hz, cf. Eqs. (6) and (9), and the number of surrogates $\mathbf{y}(n)$ was chosen to $M = 100$.

## 4.1 Simulation Scenarios

### Simulation of a Reentry Around an Anatomical Obstacle

The results from the MVAR analysis ($p = 5$) are presented in Fig. 5. The estimated auto-spectra of the signals are displayed on the diagonal, exhibiting a clear harmonic pattern for all signals. Off-diagonal, the PDCs are shown together with their corresponding significance thresholds. The direct coupling of, e.g., the signal recorded at site S1 towards the other signals is reflected by $|\pi_{i1}(f)|^2$, $i > 1$, displayed in the first column. A significant direct coupling from S1 is only identified towards S2, as only $|\pi_{21}(f)|^2$ exceeds its significance threshold. As a consequence of the stable propagation pattern and the high signal organization, a significant coupling can in fact be observed across the entire frequency range. Of specific interest is $|\pi_{21}(f)|^2$ at those frequencies for which $S_{11}(f)$ has the highest power, i.e., the highlighted frequency range around the DF. The integrated PDC over this frequency range, $\Pi_{21}^2$, yields 0.82. In terms of propagation, these observations lead to the conclusion that

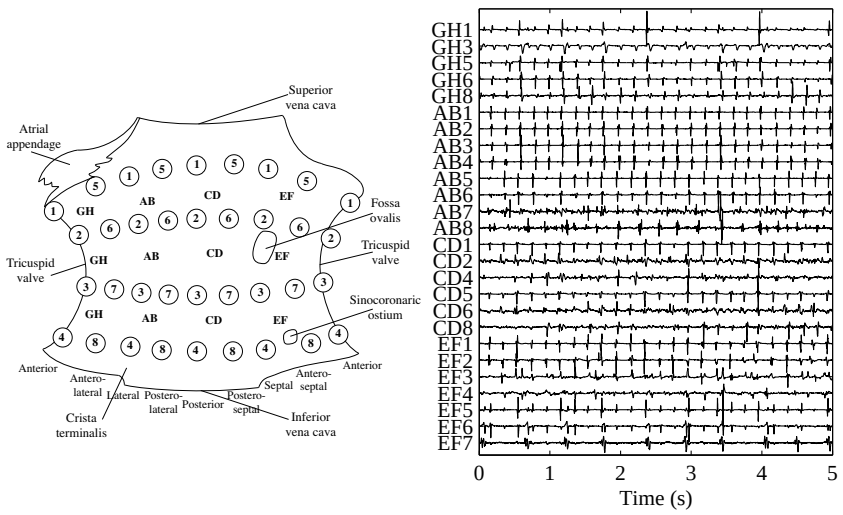


(a) (b)

**Figure 4:** (a) Schematic representation of the open RA with the position of the bipolar recording sites on the intracardiac wall. The eight splines of the basket catheter were positioned on the anterior, lateral, posterior, and septal walls, as well as on intermediate positions. (b) Original electrograms.

there is an activation wavefront propagating from S1 to S2. In case the wavefront propagates further to any other recording site, this should be reflected by $|\pi_{i2}(f)|^2$. In fact, only $|\pi_{32}(f)|^2$ exceeds its significance threshold ($\Pi^2_{32} = 0.61$), indicating that the activation wavefront propagates from S2 to S3. The PDCs $|\pi_{43}(f)|^2$ and $|\pi_{54}(f)|^2$ exceed their significance thresholds for the frequency range of interest, and thus it can be concluded that the activation wavefront propagates from S3 to S4 to S5. The corresponding integrated PDCs $\Pi^2_{43}$ and $\Pi^2_{54}$ equal 0.82 and 0.66, respectively.

The delays $\Delta_{21}$, $\Delta_{32}$, $\Delta_{43}$, and $\Delta_{54}$ are equal to 27 ms, 51 ms, 52 ms, and 50 ms, respectively. For this particular case with well-organized propagation, the delays can also be estimated by detecting the activations in all electrograms and coupling the closest activations from adjacent recording sites [10]. The delays, taken as the time difference within these activation pairs, yield 28±4 ms (mean±std), 51±5 ms, 54±5 ms, and 50±3 ms, and thus $\Delta_{21}$, $\Delta_{32}$, $\Delta_{43}$, and $\Delta_{54}$ are within ±1 standard deviation of these values.

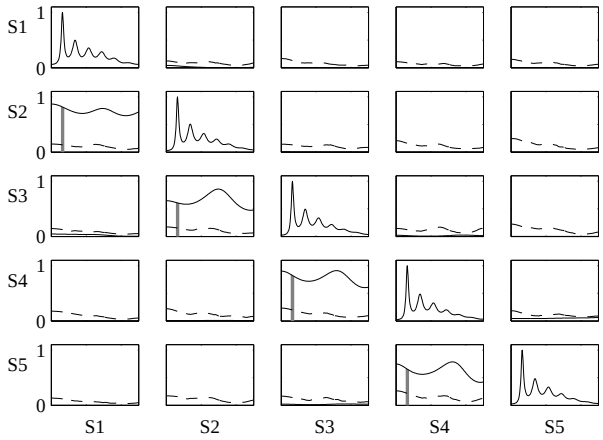


**Figure 5:** MVAR analysis applied to simulated reentry signals. On the diagonal: The auto-spectra of the signals for $f \in [0, 25]$ Hz. Off-diagonal: The PDCs $|\pi_{ij}(f)|^2$ (solid line) and the corresponding significance thresholds $|\tilde{\pi}_{ij}(f)|^2$ (dashed line) for $f \in [0, 25]$ Hz. The area beneath $|\pi_{ij}(f)|^2$, $f \in [f_0 - \Delta f, f_0 + \Delta f]$, has been highlighted when $\Pi^2_{ij}$ is significant.

### Simulation of AF

Figure 6 presents the results of the MVAR analysis ($p = 5$) applied to the simulation of AF. Compared to the previous case, the auto-spectra exhibit a less pronounced but still discernible harmonic pattern. From the PDCs, a significant direct coupling can be observed from S1 $\rightarrow$ S2 $\rightarrow$ S3 $\rightarrow$ S4. Furthermore, no significant direct coupling is present towards recording site S5. It can thus be concluded that there is an activation wavefront which is passing by S1, S2, S3, and S4, but which is not propagating further towards S5. This reflects well the propagation of the activation wavefront starting at the point source as well as the more chaotic propagation on the lower half of the sphere, which results in the absence of significant direct coupling from or towards S5. The decreasing values of $\Pi^2_{21}$, $\Pi^2_{32}$, and $\Pi^2_{43}$, being equal to 0.59, 0.31, and 0.15, respectively, indicate the decreasing relevance of the activation wavefront for the atrial activity at S1 to S4. The delays $\Delta_{21}$, $\Delta_{32}$, and $\Delta_{43}$ are estimated to 51 ms, 48 ms, and 56 ms, respectively.

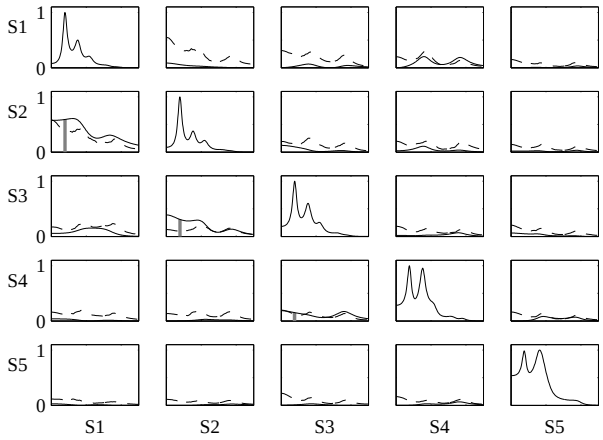


**Figure 6:** MVAR analysis applied to simulated AF signals, see Fig. 5 for details.

## 4.2 Recordings of Patients with Atrial Tachyarrhythmias

### Atrial Flutter Data

The results of the MVAR analysis ($p = 5$) show that the auto-spectra are characterized by harmonic patterns with decreasing power towards higher frequencies, see Fig. 7. The significant integrated PDCs indicate a distal-to-proximal propagation of the electrical activity along the catheter and reflect, because of the anatomic position of the CS, the sequential activation of the left atrium by the reentrant wavefront. In detail, the integrated PDCs corresponding to the direct coupling from CS1/2 towards CS5/6, CS5/6 towards CS9/10, and CS9/10 towards CS13/14 yield 0.82, 0.28, and 0.31, respectively. The corresponding delays $\Delta_{ij}$ yield 29 ms, 31 ms, and 38 ms, respectively, which suggests a propagation along the catheter. Similar to the simulation of reentry, the delays estimated from the detected activation times can be used for validation. These delays yield 26±3 ms, 31±2 ms, and 40±7 ms.

### AF Data: Linear Catheter Recording

The results from the MVAR analysis ($p = 4$) are shown in Fig. 8, where it can be seen that the auto-spectra are characterized by a dominant peak and a decreasing power towards higher frequencies. The significant integrated PDCs indicate an activation wavefront propagating from an inner electrode of the catheter (H13/14) to the remaining electrodes at both sides. Specifically, in

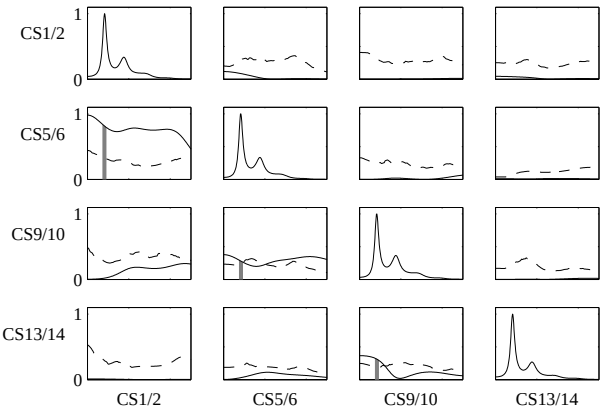


**Figure 7:** MVAR analysis applied to atrial flutter data, see Fig. 5 for details.

the high septal RA a propagation from H13/14 to both H11/12 ($\Pi^2_{12} = 0.29$) and H15/16 ($\Pi^2_{32} = 0.31$) can be identified. From H15/16, the activation wavefront is propagating further towards H17/18 ($\Pi^2_{43} = 0.49$) and H19/H20 ($\Pi^2_{54} = 0.33$). The delay from H13/14 towards H11/12 and H15/16 is estimated to 25 ms and 19 ms, respectively. Furthermore, the delays from H15/16 towards H17/18 and further towards H19/20 are estimated to 5 ms and 10 ms, respectively. The large variation in propagation delay indicates that the wavefront is probably not propagating exactly along the catheter.

### AF Data: Two-Dimensional Catheter Recording

MVAR analysis ($p = 4$) was performed on all 26 available electrograms. In order to simplify the interpretation, the significance thresholds $\tilde{\Pi}^2_{ij}$ are redefined to the 99th percentile, such that significance is given with $p \leq 0.01$. In this way, 4.5% of the theoretically possible directed coupling paths between the recording sites are found to be significant; $\Pi^2_{ij}$ ranges from 0.07 to 0.30 ($0.15 \pm 0.06$). The propagation pattern is illustrated by the directed graph in Fig. 9(a). The analysis evidences an activation wavefront propagating from the high septal region towards the lateral and septal walls in craniocaudal direction. In more detail, the larger values of $\Pi^2_{ij}$ indicate an impulse from the LA entering the RA in the high septal region, nearby CD5 and EF1, from where the propagation divides into two wavefronts. One wavefront propagates along the superior RA towards the high lateral wall (AB1), which is subsequently activated in craniocaudal direction. The second wavefront propagates along

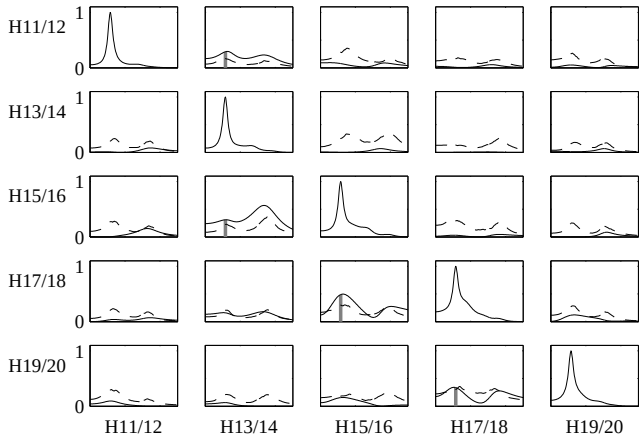


**Figure 8:** MVAR analysis applied to AF data recorded with a linear catheter, see Fig. 5 for details.

the superior RA towards the high anterior wall (GH1), as well as from the mid antero-septal to the anterior wall, where the two wavefronts meet again (GH3). A similar directed graph illustrates the corresponding propagation delays in Fig. 9(b), ranging from 2 ms to 87 ms (24±19 ms).

# 5 Discussion

A novel approach to the analysis of atrial propagation patterns is proposed and evaluated on simulated as well as real data, representing typical propagation mechanisms and recording situations. While the MVAR frequency domain description has been considered in brain signal analysis, see, e.g., [13–15], several modifications have been made here to improve performance for intracardiac signal analysis. While the spectra of the electrograms mainly reflect signal morphology, the preprocessing emphasizes the rhythm, which results in spectra characterized by a pronounced fundamental frequency corresponding to the DF. As a result, not only are lower MVAR model orders needed to describe the signals, but the interpretation of the PDC is simplified. Specifically, the evaluation of the PDCs from intracardiac AF signals can be restricted to the frequency range of interest centered around the DF, as implemented in Eq. (6). In fact, the PDC integrated within this frequency range reflects the strength of coupling between the rhythmic activities at the two considered atrial sites. Significant PDC values outside this range, though being expected when the an-

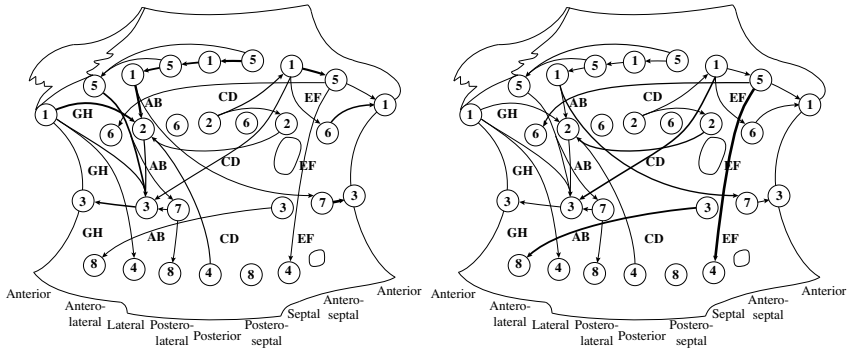


**Figure 9:** MVAR analysis applied to AF data recorded with a two-dimensional catheter. Illustration of the results for 26 simultaneously recorded electrograms from the RA. (a) A directed graph representing the significant integrated PDCs $\Pi_{ij}$ ($p \leq 0.01$). The width of the arrows is related to the size of the corresponding $\Pi_{ij}$. (b) A directed graph in which the width of the arrows is related to the size of the corresponding delay $\Delta_{ij}$.

alyzed signals exhibit harmonic patterns in the frequency domain, are of little physiological interest and can thus be excluded from further analysis. Another advancement in the present paper is the application of a recently proposed surrogate data approach [21] which is especially well-suited for the PDC as it preserves the causal coupling in all directions but the direction under evaluation. Furthermore, the frequency domain representation of the MVAR model is also employed to estimate the delays along directions with significant coupling, facilitating the estimation of propagation delays. The delays are usually not of interest in brain signal analysis, whereas they provide interesting insights on AF propagation patterns through the estimation of atrial conduction times.

The PDC belongs to a class of causality measures which are frequency domain representations of Granger causality [26]. According to this concept, there is Granger causality from signal $x_j(n)$ to signal $x_i(n)$ if knowledge about past values of $x_j(n)$ improves the prediction of $x_i(n)$. MVAR modeling has become the most common tool to identify Granger causality, and from the definition in Eq. (1), it can be seen that Granger causality from $x_j(n)$ to $x_i(n)$ is reflected by certain $a_{ij}(k)$ being different from zero. Measures such as the PDC represent this concept in the frequency domain: Eq. (2) shows that the absence of Granger causality from $x_j(n)$ to $x_i(n)$ results in a PDC which is zero

for all frequencies. The link between causality in the time and frequency domain makes the PDC a powerful tool as direct coupling from $x_j(n)$ to $x_i(n)$ can be evaluated at a specific frequency. In the literature there are also other, widely used frequency domain measures similar to the PDC, such as the Directed Coherence (DC) [27]. In contrast to the PDC, the DC quantifies the presence of both direct and indirect coupling, which results from the fact that DC and PDC are defined as factors in the decomposition of the ordinary coherence and the partial coherence, respectively [14]. This leads to different fields of application for the two measures: while the PDC is especially suitable for tracking the path of the direct information flow, the DC is advantageous when the main interest is to identify the source of the information flow. In the present paper, the analysis of propagation patterns of the electrical activity has been prioritized over source identification.

The present study aims at demonstrating the potential of the method for analysis of atrial arrhythmia mechanisms. For this purpose, two scenarios have been simulated using the CNR model, which has proved to be particularly useful for the simulation of human atrial arrhythmias and the reproduction of realistic electrograms [25]. The results showed that the PDC well reflected the known simulated patterns, thereby validating the use of the evaluated approach in the analysis of atrial electrograms. This is an important result, as MVAR modeling assumes that the signal is stationary over the analyzed time window and that only linear coupling is present, while the propagation during AF can change over time and the coupling is known to be both linear and non-linear, see, e.g., [28]. During the simulation of AF with an ectopic focus, the propagation on the lower part of the sphere was disorganized, thus resulting in signals in which non-linear and non-stationary features are likely to be predominant. However, the results showed that the absence of a stable and coherent rhythm is reflected by a low or non-significant PDC, while the couplings on the upper part of the sphere, where the propagation was more organized, could still be correctly identified.

Regarding the values of the PDC, it is important to consider the normalization in Eq. (4), which states that the sum of the PDCs from one signal to all other signals must be 1 at all frequencies. This normalization implies that the PDC can have large values even at frequencies at which the power of the source signal is low, see, e.g., Fig. 5. However, a large value at a frequency at which the power spectrum is low is actually of little relevance. Thus, when interpreting the PDC, it is important to consider both the significance thresholds and the power spectra. The latter has been taken care of by interpreting the PDC at the DF, which, after the preprocessing, almost always has the largest power. While a pronounced DF is not a prerequisite for finding a significant causal coupling, it reflects the presence of a pronounced rhythm in

the corresponding time signal, and thus a propagation as well as a significant causal coupling leading towards or away from the corresponding recording site becomes more likely. On the other hand, two sites having different rhythms, reflected by different DFs, or a site with a less pronounced rhythm, reflected by a less pronounced DF, are more likely to have low PDCs, indicating the absence of propagation. The behavior of the method in such rare cases as a 2:1 conduction block, during which there is a regular propagation between two sites though the corresponding DFs differ by a factor of two, would be highly interesting to investigate.

In a recent study [29], Elvan et al. found that the DF during AF correlates poorly with AF cycle length, and therefore recommended time domain analysis of the electrogram. While their results would call in question the present approach, being inherently frequency domain in nature, certain aspects of the study by Elvan et al. have been the subject for discussion, including their algorithms used for noise rejection, preprocessing and the determination of dominant frequency [30, 31]. In another recent study, Grzeda et al. [32] found that frequency domain analysis was more robust than time domain analysis in detecting the average local activation rate.

The method was evaluated on both atrial flutter and fibrillation electrograms, recorded with different mapping modalities. The evaluation of the propagation pattern during atrial flutter evidenced the typical sequential activation found during reentrant activity. The propagation patterns evidenced during AF provided more detailed information about the underlying mechanisms of the arrhythmia. In both cases, the site of earliest activation within the recording area was found to be in the high septal RA, suggesting atrial impulses entering the RA from the left atrium through the Bachmans bundle region. This agrees with the role of the LA as a driver of AF as well as with previous findings about RA breakthrough sites [33, 34]. Moreover, RA activation observed in paroxysmal AF, involving the earliest activation of the upper septal region and a subsequent cranio-caudal spreading in both the lateral and septal RA, is in agreement with previous clinical observations [33–35]. Interestingly, this specific RA activation pattern has been associated to the presence of a focal source in the right upper pulmonary veins [35]. These results further emphasize the potential of the method in extracting information about the underlying propagation pattern, which has substantial value during electrophysiological studies, especially when performed in connection to ablation procedures. Nevertheless, additional validation is required before introducing the approach into clinical practice. In future studies, it would thus be of interest to further evaluate the method on a larger database recorded during atrial arrhythmia, which ideally should also comprise recordings from the left atrium. The computational time of the algorithm is compatible with practical utilization in electrophysiol-

ogy; the most time consuming part being the significance test, which may take several minutes. However, optimization and utilization of simpler algorithms, such as phase randomization [21] or theoretical significance levels [36], should be investigated.

In the example of paroxysmal AF recorded with a basket catheter weaker direct couplings over longer distances are also observed, e.g., from AB1 to EF7. From a physiological point of view, such couplings are less likely. Methodologically, they can arise from the fact that LS estimation tends to overfit the MVAR model when the number of unknown MVAR coefficients, $Np$, exceeds the sample size [37]. A possibility to improve the estimation of the MVAR coefficients and the corresponding propagation delays in such a case is to consider estimation methods that encourage sparsity by putting constraints, such as the L1-norm, on the LS estimation [37]. In addition, sparse estimation methods can be motivated by the observation that connectivity during AF may be viewed as *a priori* sparse, as it is well-known that coupling between the recording sites during AF decreases with increasing distance. Currently, we are investigating approaches to sparse MVAR model estimation, as well as the possibility to incorporate information about the distance between the recording sites into the estimation, to improve the method when a larger number of signals is involved.

In the present study, the analysis is performed over 5-s time windows, thus revealing propagation patterns which are stable over a larger number of activation wavefronts. This is in contrast to methods relying on activation detection, which, provided that AF organization is sufficiently high, facilitate the detection and characterization of individual activation wavefronts. In order to improve time resolution and track temporal variations in the propagation pattern, the time window should be shortened, and the MVAR model coefficients estimated adaptively [18]. Furthermore, the analysis could be improved by a modeling approach which is able to capture linear as well as non-linear coupling. Tests performed in the present study to check the assumption that the MVAR model is generated by a multivariate white noise process revealed that, in some cases, minor correlation between the residuals exists. However, multivariate approaches to non-linear Granger causality have never been performed in AF signal analysis. So far, the concept of non-linear Granger causality has only been addressed briefly relative AF, employing a bivariate measure [38]; bivariate signal analysis is a common restriction of most approaches to non-linear causality [39, 40]. Another disadvantage is that non-linear Granger causality has a time domain representation only, thus missing the benefits of a frequency domain representation which can be evaluated for a specific frequency range such as the DF. Nevertheless, a multivariate approach to non-linear causality could allow further exploration of the nature of the mechanisms underlying propagation patterns during atrial arrhythmias.

## 6 Conclusions

In the present paper, a novel approach has been introduced to the characterization of atrial propagation patterns during atrial tachyarrhythmias. The method can identify the underlying propagation mechanisms and serve as a support for the electrophysiologist when locating ablation sites. Moreover, the possibility of quantifying the propagation pattern in terms of direction and strength of the coupling as well as the propagation delay can be applied to efficiently evaluate such patterns in existing databases.

## References

[1] G. Moe, "On the multiple wavelet hypothesis of atrial fibrillation," *Arch. Int. Pharmacodyn. Ther.*, vol. 140, pp. 183–188, 1962.

[2] M. Haïssaguerre, P. Jaïs, D. Shah, A. Takahashi, M. Hocini, G. Quiniou, S. Garrigue, A. L. Mouroux, P. L. Métayer, and J. Clémenty, "Spontaneous initiation of atrial fibrillation by ectopic beats originating in the pulmonary veins," *N. Engl. J. Med.*, vol. 339, pp. 659–666, 1998.

[3] T. Arentz, L. Haegeli, P. Sanders, R. Weber, F. J. Neumann, D. Kalusche, and M. Haïssaguerre, "High-density mapping of spontaneous pulmonary vein activity initiating atrial fibrillation in humans," *J. Cardiovasc. Electrophysiol.*, vol. 18, pp. 31–38, 2007.

[4] F. Atienza, J. Almendral, J. Moreno, R. Vaidyanathan, A. Talkachou, J. Kalifa, A. Arenal, J. P. Villacastín, E. G. Torrecilla, A. Sánchez, R. Ploutz-Snyder, J. Jalife, and O. Berenfeld, "Activation of inward rectifier potassium channels accelerates atrial fibrillation in humans: evidence for a reentrant mechanism," *Circulation*, vol. 114, pp. 2434–42, 2006.

[5] K. Nademanee, J. McKenzie, E. Kosar, M. Schwab, B. Sunsaneewitayakul, T. Vasavakul, C. Khunnawat, and T. Ngarmukos, "A new approach for catheter ablation of atrial fibrillation: mapping of the electrophysiologic substrate," *J. Am. Coll. Cardiol.*, vol. 43, pp. 2044–53, 2004.

[6] P. Sanders, O. Berenfeld, M. Hocini, P. Jaïs, R. Vaidyanathan, L.-F. Hsu, S. Garrigue, Y. Takahashi, M. Rotter, F. Sacher, C. Scavée, R. Ploutz-Snyder, J. Jalife, and M. Haïssaguerre, "Spectral analysis identifies sites of high-frequency activity maintaining atrial fibrillation in humans," *Circulation*, vol. 112, pp. 789–797, 2005.

[7] H. Oral, A. Chugh, E. Good, A. Wimmer, S. Dey, N. Gadeela, *et al.*, "Radiofrequency catheter ablation of chronic atrial fibrillation guided by complex electrograms," *Circulation*, vol. 115, pp. 2606–12, 2007.

[8] I. Deisenhofer, H. Estner, T. Reents, S. Fichtner, A. Bauer, J. Wu, C. Kolb, B. Zrenner, C. Schmitt, and G. Hessling, "Does electrogram guided substrate ablation add to the success of pulmonary vein isolation in patients with paroxysmal atrial fibrillation? A prospective, randomized study," *J. Cardiovasc. Electrophysiol.*, vol. 20, pp. 514–521, 2009.

[9] F. Ravelli, L. Faes, L. Sandrini, F. Gaita, R. Antolini, M. Scaglione, and G. Nollo, "Wave similarity mapping shows the spatiotemporal distribution of fibrillatory wave complexity in the human right atrium during paroxysmal and chronic atrial fibrillation," *J. Cardiovasc. Electrophysiol.*, vol. 16, pp. 1071–76, 2005.

[10] V. Barbaro, P. Bartolini, G. Calcagnini, F. Censi, and A. Michelucci, "Measure of synchronisation of right atrial depolarisation wavefronts during atrial fibrillation," *Med. Biol. Eng. Comp.*, vol. 40, pp. 56–62, 2002.

[11] U. Richter, A. Bollmann, D. Husser, and M. Stridh, "Right atrial organization and wavefront analysis in atrial fibrillation," *Med. Biol. Eng. Comp.*, vol. 47, pp. 1237–46, 2009.

[12] H. J. Sih, A. V. Sahakian, C. E. Arentzen, and S. Swiryn, "A frequency domain analysis of spatial organization of epicardial maps," *IEEE Trans. Biomed. Eng.*, vol. 42, pp. 718–727, 1995.

[13] P. J. Franaszczuk, G. K. Bergey, and M. J. Kaminski, "Analysis of mesial temporal seizure onset and propagation using the directed transfer function method," *Electroencephal. Clin. Neurophysiol.*, vol. 91, pp. 413–427, 1994.

[14] L. A. Baccalá and K. Sameshima, "Partial directed coherence: a new concept in neural structure determination," *Biol. Cybern.*, vol. 84, pp. 463–474, 2001.

[15] L. A. Baccalá, K. Sameshima, and D. Y. Takahashi, "Generalized partial directed coherence," in *Proc. 15th Intern. Conf. on Digital Signal Processing*, pp. 162–166, IEEE Press, 2007.

[16] D. Botteron and J. Smith, "A technique for measurement of the extent of spatial organization of atrial activation during atrial fibrillation in the intact human heart," *IEEE Trans. Biomed. Eng.*, vol. 42, pp. 579–586, 1995.

[17] J. Ng, A. H. Kadish, and J. J. Goldberger, "Effect of electrogram characteristics on the relationship of dominant frequency to atrial activation rate in atrial fibrillation," *Heart Rhythm*, vol. 3, pp. 1295–1305, 2006.

[18] C. Wilke, L. Ding, and B. He, "Estimation of time-varying connectivity patterns through the use of an adaptive directed transfer function," *IEEE Trans. Biomed. Eng.*, vol. 55, pp. 2557–64, 2008.

[19] T. Müller, M. Lauk, M. Reinhard, A. Hetzel, C. H. Lücking, and J. Timmer, "Estimation of delay times in biological systems," *Ann. Biomed. Eng.*, vol. 31, pp. 1423–39, 2003.

[20] G. Schwarz, "Estimating the dimension of a model," *Ann. Stat.*, vol. 6, pp. 461–464, 1978.

[21] L. Faes, A. Porta, and G. Nollo, "Testing frequency domain causality in multivariate time series," *IEEE Trans. Biomed. Eng.*, vol. 57, pp. 1897–1906, 2010.

[22] M. Courtemanche, R. J. Ramirez, and S. Nattel, "Ionic mechanisms underlying human atrial action potential properties: insights from a mathematical model.," *Am. J. Physiol.*, vol. 275, pp. H301–321, 1998.

[23] S. Rush and H. Larsen, "A practical algorithm for solving dynamic membrane equations," *IEEE Trans. Biomed. Eng.*, vol. 25, pp. 389–392, 1978.

[24] S. Zozor, O. Blanc, V. Jacquemet, N. Virag, J.-M. Vesin, E. Pruvot, L. Kappenberger, and C. Henriquez, "A numerical scheme for modeling wavefront propagation on a monolayer of arbitrary geometry," *IEEE Trans. Biomed. Eng.*, vol. 50, pp. 412–420, 2003.

[25] V. Jacquemet, N. Virag, Z. Ihara, L. Dang, O. Blanc, S. Zozor, J.-M. Vesin, L. Kappenberger, and C. Henriquez, "Study of unipolar electrogram morphology in a computer model of atrial fibrillation," *J. Cardiovasc. Electrophysiol.*, vol. 14 (Suppl.), pp. 172–179, 2003.

[26] C. W. J. Granger, "Investigating causal relations by econometric models and cross-spectral methods," *Econometrica*, vol. 37, pp. 424–443, 1969.

[27] L. A. Baccalá, K. Sameshima, G. Ballester, A. C. D. Valle, and C. Timo-Iaria, "Studying the interaction between brain structures via directed coherence and Granger causality," *Appl. Signal Proc.*, vol. 5, pp. 40–48, 1998.

[28] F. Censi, V. Barbaro, P. Bartolini, G. Calcagnini, A. Michelucci, and S. Cerutti, "Non-linear coupling of atrial activation processes during atrial fibrillation in humans," *Biol. Cybern.*, vol. 85, pp. 195–201, 2001.

[29] A. Elvan, A. C. Linnenbank, M. W. van Bemmel, A. R. R. Misier, P. P. H. M. Delnoy, W. P. Beukema, and J. M. T. de Bakker, "Dominant frequency of atrial fibrillation correlates poorly with atrial fibrillation cycle length," *Circ Arrhythm Electrophysiol*, vol. 2, pp. 634–644, 2009.

[30] P. Platonov, M. Stridh, and L. Sörnmo, "Letter by Platonov et al. regarding article, "Dominant frequency of atrial fibrillation correlates poorly with atrial fibrillation cycle length"," *Circ. Arrhythm. Electrophysiol.*, vol. 3, p. e4, 2010.

[31] O. Berenfeld and J. Jalife, "Letter by Berenfeld and Jalife regarding article "Dominant frequency of atrial fibrillation correlates poorly with atrial fibrillation cycle length"," *Circ. Arrhythm. Electrophysiol.*, vol. 3, p. e1, 2010.

[32] K. R. Grzeda, S. F. Noujaim, O. Berenfeld, and J. Jalife, "Complex fractionated atrial electrograms: properties of time-domain versus frequency-domain methods," *Heart Rhythm*, vol. 6, pp. 1475–82, 2009.

[33] B. Zrenner, G. Ndrepepa, M. R. Karch, M. A. Schneider, J. Schreieck, A. Schömig, and C. Schmitt, "Electrophysiologic characteristics of paroxysmal and chronic atrial fibrillation in human right atrium," *J. Am. Coll. Cardiol.*, vol. 38, pp. 1143–49, 2001.

[34] S. Saksena, N. D. Skadsberg, H. B. Rao, and A. Filipecki, "Biatrial and three-dimensional mapping of spontaneous atrial arrhythmias in patients with refractory atrial fibrillation," *J. Cardiovasc. Electrophysiol.*, vol. 16, pp. 494–504, 2005.

[35] D. O'Donnell, S. S. Furniss, and J. P. Bourke, "Dynamic alterations in right atrial activation during atrial fibrillation," *J. Interv. Card. Electrophysiol.*, vol. 8, pp. 37–40, 2003.

[36] B. Schelter, J. Timmer, and M. Eichler, "Assessing the strength of directed influences among neural signals using renormalized partial directed coherence," *J. Neurosci. Meth.*, vol. 179, pp. 121–130, 2009.

[37] P. A. Valdés-Sosa, J. M. Sánchez-Bornot, A. Lage-Castellanos, M. Vega-Hernández, J. Bosch-Bayard, L. Melie-García, and E. Canales-Rodríguez,

"Estimating brain functional connectivity with sparse multivariate autoregression," *Phil. Trans. Roy. Soc. Lond. B Biol. Sci.*, vol. 360, pp. 969–981, 2005.

[38] B. P. T. Hoekstra, C. G. H. Diks, M. A. Allessie, and J. DeGoede, "Nonlinear time series analysis: methods and applications to atrial fibrillation," *Ann. Ist. Super. Sanità*, vol. 37, pp. 325–333, 2001.

[39] W. Freiwald, P. Valdes, J. Bosch, R. Biscay, J. Jimenez, L. Rodriguez, V. Rodriguez, A. Kreiter, and W. Singer, "Testing non-linearity and directedness of interactions between neural groups in the macaque inferotemporal cortex," *J. Neurosci. Meth.*, vol. 94, pp. 105–119, 1999.

[40] M. Chavez, J. Martinerie, and M. Le Van Quyen, "Statistical assessment of nonlinear causality: application to epileptic EEG signals," *J. Neurosci. Meth.*, vol. 124, pp. 113–128, 2003.

# *Paper IV*

# Propagation Pattern Analysis in Intracardiac Atrial Fibrillation Signals Based on Sparse Modeling

**Abstract**

In the present study, sparse modeling is introduced for the estimation of propagation patterns in intracardiac atrial fibrillation (AF) signals. The sparsity can be motivated by the observation that direct couplings over longer distances are likely to be zero during AF. The estimation of the propagation patterns is based on the partial directed coherence (PDC), which evaluates the direct coupling between multiple signals in the frequency domain and is derived from the fit of a multivariate autoregressive (MVAR) model, commonly estimated by the least-squares (LS) method. In order to avoid overfitting of the MVAR model and to incorporate prior information such as sparsity and the distances between the recording sites, the adaptive group least absolute selection and shrinkage operator (LASSO) is introduced, and furthermore, the distance-adaptive group LASSO is proposed. In simulations, adaptive and distance-adaptive group LASSO are found to be superior to LS estimation in terms of detecting the direct couplings and estimating their corresponding strength through the PDC. The method is also evaluated on an AF recording obtained with a two-dimensional catheter, showing that the identification of the propagation pattern can be substantially simplified by the sparsity coming with adaptive and distance-adaptive group LASSO. This further promotes the PDC as a method for analysis of AF propagation patterns, which may contribute to a better understanding of AF mechanisms as well as improved AF treatment.

---


U. Richter, L. Faes, F. Ravelli and L. Sörnmo,
"Propagation Pattern Analysis in Intracardiac Atrial Fibrillation Signals Based on Sparse Modeling",
Manuscript.

# 1 Introduction

In current clinical practice, surgical treatment of atrial fibrillation (AF) is mainly restricted to a standardized ablation procedure at the pulmonary veins. Recent progress indicates however that future ablation treatment of AF will be tailored to the individual patient in order to achieve optimal success rates [1–3]. Therefore, methods are required which can improve the understanding of AF mechanisms and accurately guide the ablation catheter to the atrial sites at which the arrhythmia originates or which represent arrhythmia substrates. Methods for propagation pattern analysis are thus of interest as they have the potential to point out ectopic foci or identify reentrant activities.

Time domain analysis of propagation patterns is usually based on activation detection and the grouping of detected activations into wavefronts [4–6]. An advantage of such methods is their potential to detect and analyze individual wavefronts. However, it is problematic to detect activation times when AF organization is low. In such cases, the high complexity of the propagation patterns makes it difficult to decide which of the activations should be assigned to the same activation wavefront. Frequency domain analysis of AF propagation patterns can, to some extent, overcome these disadvantages. Recently, our group proposed the usage of the partial directed coherence (PDC) function for propagation pattern analysis during AF [7]. The PDC quantifies the causal coupling between multiple signals in the frequency domain, which previously has been successfully employed for the analysis of brain signals [8, 9]. The potential of the PDC when applied to intracardiac AF signals was illustrated with both simulation scenarios and real data recordings, selected to present typical propagation mechanisms and recording situations [7]. In the simulation scenarios, the method could correctly identify the coupling direction and thus the propagation between all recording sites. Furthermore, the identified propagation patterns in the real data recordings were found to agree with previous clinical observations.

The derivation of the PDC is based on the fit of a multivariate autoregressive (MVAR) model to multichannel recordings. In order to estimate the MVAR coefficients, least-squares (LS) estimation is commonly employed. The estimation of the MVAR coefficients can be improved, e.g., with respect to overfitting, by considering methods that put constraints on the LS solution. Further improvements may be achieved by considering constraints which also encourage sparsity, which is in contrast to the assumption of "full" connectivity during LS estimation, i.e., coupling between all recording sites. The usage of sparse estimation methods in the context of AF can be justified by the observation that connectivity during AF may be viewed as *a priori* sparse, as it is well-known that the coupling between the recording sites during AF de-

creases with increasing distance. Thus, those MVAR coefficients which model the coupling between distant recording sites are more likely to be zero.

Constraints based on the least absolute selection and shrinkage operator (LASSO) [10] have been shown to be particularly effective for reducing the complexity of models by shrinking certain coefficients to exactly zero. In the present paper, the adaptive group LASSO [11] is proposed for improving the MVAR modeling of atrial activity during AF. As the name suggests, this LASSO variant allows the construction of groups of the unknown parameters which can be pruned jointly. Thus, MVAR coefficients which model the coupling from one signal to another should be grouped together, leading to a solution which is sparse with respect to both the MVAR coefficients and the causal coupling. In the adaptive group LASSO, a different amount of shrinkage can be applied to different groups of MVAR coefficients, which also opens for the possibility to incorporate information on the distance between the recording sites into the analysis. By achieving better estimates of the MVAR coefficients, errors which may propagate from the estimated MVAR coefficients to the PDC can be prevented.

In the following, the impact of MVAR modeling on the estimation of the PDC when employing LS as well as adaptive and distance-adaptive group LASSO will be evaluated based on simulations, in which the true MVAR model is known, as well as on an AF recording acquired with a two-dimensional catheter.

# 2 Methods

## 2.1 Multivariate Autoregressive Modeling

Each set of $N$ simultaneous observations $\mathbf{x}(n) = \begin{bmatrix} x_1(n) & \cdots & x_N(n) \end{bmatrix}^T$, obtained from different sites in the atria, is assumed to be represented by an MVAR model of order $m$

$$\mathbf{x}(n) = \sum_{k=1}^{m} \mathbf{A}_k \mathbf{x}(n-k) + \mathbf{w}(n), \quad n = 1, \ldots, T, \tag{1}$$

where each $\mathbf{A}_k$ is an $N \times N$ matrix comprising the AR coefficients $a_{ij}(k)$, $i, j = 1, \ldots, N$, and $\mathbf{w}(n) = \begin{bmatrix} w_1(n) & \cdots & w_N(n) \end{bmatrix}^T$ is a multivariate white noise process characterized by the diagonal covariance matrix $\mathbf{\Sigma}_w$, in which each diagonal element $\sigma_{jj}^2$ defines the variance of $w_j(n)$. Furthermore, a measure of the distance between the recording sites is stored in the symmetric $N \times N$ matrix $\mathbf{D} = \begin{bmatrix} \mathbf{d}_1 & \cdots & \mathbf{d}_N \end{bmatrix}$.

For the estimation of MVAR coefficients, it is convenient to rewrite Eq. (1) in matrix form,

$$\mathbf{X} = \mathbf{YB} + \mathbf{W}, \tag{2}$$

where

$$\begin{aligned}
\mathbf{X} &= \begin{bmatrix}\mathbf{x}(1) & \cdots & \mathbf{x}(T)\end{bmatrix}^T = \begin{bmatrix}\mathbf{x}_1 & \cdots & \mathbf{x}_N\end{bmatrix}, \\
\mathbf{W} &= \begin{bmatrix}\mathbf{w}(1) & \cdots & \mathbf{w}(T)\end{bmatrix}^T, \\
\mathbf{B} &= \begin{bmatrix}\mathbf{A}_1 & \cdots & \mathbf{A}_m\end{bmatrix}^T = \begin{bmatrix}\boldsymbol{\beta}_1 & \cdots & \boldsymbol{\beta}_N\end{bmatrix}, \\
\mathbf{y}(n) &= \begin{bmatrix}\mathbf{x}(n) \\ \vdots \\ \mathbf{x}(n-m+1)\end{bmatrix}, \\
\mathbf{Y} &= \begin{bmatrix}\mathbf{y}(1) & \cdots & \mathbf{y}(T)\end{bmatrix}^T.
\end{aligned}$$

Employing this notation, the LS solution for the MVAR coefficients becomes [12]

$$\begin{aligned}
\tilde{\mathbf{B}} &= \arg\min_{\mathbf{B}} ||\mathbf{X} - \mathbf{YB}||^2 &(3)\\
&= (\mathbf{Y}^T\mathbf{Y})^{-1}\mathbf{Y}^T\mathbf{X}, &(4)
\end{aligned}$$

where $||\cdot||$ denotes the $L_2$ norm. The MVAR coefficients contained in column $\boldsymbol{\beta}_i$ of matrix $\mathbf{B}$, responsible for predicting $x_i(n)$, can also be estimated separately,

$$\tilde{\boldsymbol{\beta}}_i = \arg\min_{\boldsymbol{\beta}_i} ||\mathbf{x}_i - \mathbf{Y}\boldsymbol{\beta}_i||^2. \tag{5}$$

In order to achieve a sparse solution, certain constraints can be assigned on Eq. (5) (in the following the index $i$ will be omitted for simplicity unless necessary). The adaptive group LASSO, in which the coefficients in $\boldsymbol{\beta}$ are divided into $L$ non-overlapping groups $\boldsymbol{\beta}_l$ of corresponding sizes $p_l$, $l = 1, \ldots, L$, is defined to [11]

$$\hat{\boldsymbol{\beta}} = \arg\min_{\boldsymbol{\beta}} ||\mathbf{x} - \sum_{l=1}^{L} \mathbf{Y}_l\boldsymbol{\beta}_l||^2 \quad \text{subject to} \quad \sum_{l=1}^{L} \alpha_l||\boldsymbol{\beta}_l|| \leq t, \tag{6}$$

where $\mathbf{Y}_l$ is referred to as the $l$-th group of input variables and consists of those columns of matrix $\mathbf{Y}$ that correspond to the coefficients contained in $\boldsymbol{\beta}_l$, the $\alpha_l$ are positive weighting factors, and $t \geq 0$ is the upper bound of the constraint. When applying the adaptive group LASSO to the estimation of MVAR coefficients with the goal to encourage sparse coupling, all coefficients which model

the coupling from one recording site to another should be grouped together such that they can only be pruned jointly, i.e., $\boldsymbol{\beta}_l = \begin{bmatrix} a_{il}(1) & \cdots & a_{il}(m) \end{bmatrix}^T$, $l = 1, \ldots, L$. With this setting, the number of groups becomes equal to the spatial dimension, i.e., $L = N$, and all groups become equally large, i.e., $p_l = m$ for all $l$.

When the same amount of shrinkage is applied to each group, i.e., $\alpha_l = \alpha$ for all $l$, Eq. (6) simplifies to the ordinary group LASSO [13]. However, it has been shown theoretically that by allowing different amounts of shrinkage for different groups, the true model can be identified consistently [11]. Weighting factors adapting to the data by employing the LS solution have been proposed,

$$\alpha_l = ||\tilde{\boldsymbol{\beta}}_l||^{-\gamma_1}, \tag{7}$$

where $\gamma_1 > 0$.

During AF, it is well-known that the coupling between recording sites decreases with increasing distance. Thus, additional prior knowledge can be included in the estimation procedure by letting the weighting factors also adapt to the distance, i.e.,

$$\alpha_l = \alpha(d_l)||\tilde{\boldsymbol{\beta}}_l||^{-\gamma_1}, \tag{8}$$

where $d_l$ is the $l$-th element of the distance vector $\mathbf{d}_i$. For the choice of $\alpha(d_l) = 1$, Eq. (8) simplifies to Eq. (7) and thus the adaptive group LASSO. For the distance-adaptive group LASSO, the Gaussian kernel function is employed,

$$\alpha(d_l) = \exp\left(\frac{1}{2}\frac{d_l^2}{\gamma_2^2}\right) \tag{9}$$

where $\gamma_2 > 0$.

## 2.2 Model Identification and Selection

In contrast to the LS solution, no closed-form solution can be derived for the adaptive group LASSO. In the present study, the algorithm for least angle regression selection (LARS) has been employed to solve the adaptive group LASSO [13]. Prior to applying the LARS algorithm, each $\mathbf{Y}_l$ must be orthonormalized, and the estimated coefficients must be transformed back to the original scale afterwards. The LARS algorithm starts with all coefficients in all groups being equal to zero, i.e., $\hat{\boldsymbol{\beta}}_l = \mathbf{0}$ for $l = 1, \ldots, L$. The algorithm then finds the group of input variables $\mathbf{Y}_l$ which is most correlated with the residual, where the correlation is evaluated according to

$$\frac{1}{\alpha_l^2}||\mathbf{Y}_l^T\mathbf{r}||^2, \tag{10}$$

with $\mathbf{r}$ being the current residual. This group of input variables is the first group to become "active", however, the corresponding coefficients $\hat{\boldsymbol{\beta}}_l$ are not set directly to their LS solution $\tilde{\boldsymbol{\beta}}_l$. Instead, the LARS algorithm takes only the largest possible step in that direction until some other, yet inactive group $\mathbf{Y}_l$ is equally correlated to the current residual and added to the set of active groups. In that way, the algorithm proceeds stepwise towards to the LS solution, making one of the $L$ groups active in each iteration step. Thus, the solution goes from $\hat{\boldsymbol{\beta}} = \mathbf{0}$ to $\hat{\boldsymbol{\beta}} = \tilde{\boldsymbol{\beta}}$ in maximum $L$ iteration steps.

In order to select the appropriate iteration step, the Bayesian information criterion (BIC) has been employed [11]

$$\mathrm{BIC} = \log\left(\frac{1}{T}||\mathbf{x} - \mathbf{Y}\hat{\boldsymbol{\beta}}||^2\right) + \log T \cdot \frac{\nu}{T}, \tag{11}$$

where $\nu$ is the number of the degrees of freedom, defined as

$$\nu = \sum_{l=1}^{L} u(||\hat{\boldsymbol{\beta}}_l||) + \sum_{l=1}^{L} \frac{\hat{\boldsymbol{\beta}}_l}{\tilde{\boldsymbol{\beta}}_l}(p_l - 1), \tag{12}$$

and $u(\cdot)$ equals one for positive arguments and zero otherwise. The degrees of freedom range from zero to the total number of unknown parameters, $\sum_l p_l$, which corresponds to the trivial solution $\hat{\boldsymbol{\beta}}_l = \mathbf{0}$ and the LS solution $\hat{\boldsymbol{\beta}}_l = \tilde{\boldsymbol{\beta}}_l$ for all $l$, respectively. The optimal iteration step is chosen as that step for which the minimum BIC is reached.

For adaptive group LASSO, the optimal $\gamma_1$ is searched for by grid search and determined by the BIC [14]. For distance-adaptive group LASSO, the optimal $\gamma_1$ from adaptive group LASSO is employed, and the optimal $\gamma_2$ is similarly searched for by grid search and determined by the BIC. Finally, the BIC is also employed to choose the best model order $m$.

## 2.3 Partial Directed Coherence

The PDC from $x_j(n)$ to $x_i(n)$ can be derived from factorization of the partial coherence function [8, 9], and is given by

$$\pi_{ij}(f) = \frac{\frac{1}{\sigma_{ii}}\bar{A}_{ij}(f)}{\sqrt{\sum_{k=1}^{N}\frac{1}{\sigma_{kk}^2}|\bar{A}_{kj}(f)|^2}}, \tag{13}$$

where $\bar{A}_{ij}(f)$ is an element of the matrix $\bar{\mathbf{A}}(f)$, which is based on the Fourier transform of the MVAR process in Eq. (1),

$$\bar{\mathbf{A}}(f) = \mathbf{I}_{N\times N} - \sum_{k=1}^{m}\mathbf{A}_k e^{-\jmath 2\pi f k}, \tag{14}$$

where $\mathbf{I}$ is the unity matrix. The definition in Eq. (13) is that of the generalized PDC [9], being especially useful in the case of widely different variances $\sigma_{jj}^2$. The denominator of the PDC serves as a normalization with respect to the source, i.e., $x_j(n)$, such that

$$\sum_{i=1}^{N} |\pi_{ij}(f)|^2 = 1 \tag{15}$$

and

$$0 \leq |\pi_{ij}(f)|^2 \leq 1. \tag{16}$$

Given this normalization, the value of the magnitude-squared PDC $|\pi_{ij}(f)|^2$ from $j$ to $i$ represents the strength of the direct coupling from $x_j(n)$ to $x_i(n)$ at frequency $f$, viewed in relation to the direct coupling strength of $x_j(n)$ to all other signals $x_k(n)$, $k \neq i$, at that frequency. For reasons of convenience, the magnitude-squared PDC $|\pi_{ij}(f)|^2$ is referred to as PDC in the following.

During AF, the PDC is of special interest in an interval centered around the dominant frequency (DF) of the source $x_j(n)$, here assumed to represent the mean atrial fibrillatory cycle length at the corresponding recording site. Thus, the integrated PDC is defined by [15]

$$\Pi_{ij}^2 = \frac{1}{2\Delta f} \int_{f_0-\Delta f}^{f_0+\Delta f} |\pi_{ij}(f)|^2 df, \tag{17}$$

where $f_0$ is the DF, corresponding to the highest peak in the 3–12 Hz range of the auto-spectrum of $x_j(n)$, denoted $S_{jj}(f)$, and $\Delta f$ is a parameter determining the width of the integration interval. Similar to the PDC, the integral is normalized such that it ranges from zero to one, and thus represents the average coupling from $x_j(n)$ to $x_i(n)$ in the frequency range of interest. In case no obvious DF can be identified in signal $x_j(n)$, the corresponding $\Pi_{ij}^2$ is set to zero for all $i$. The auto-spectra $S_{jj}(f)$ are the diagonal elements in the power spectral density matrix of the MVAR process, defined as

$$\mathbf{S}(f) = \bar{\mathbf{A}}^{-1}(f)\mathbf{\Sigma}_w(\bar{\mathbf{A}}^{-1}(f))^H. \tag{18}$$

## 2.4 Surrogate Data Testing

Surrogate data testing is performed for the integrated PDC $\Pi_{ij}^2$ as previously described in [7]. In general terms, the method of surrogate data testing relies on computing $\Pi_{ij}^2$ both on the original time series $\mathbf{x}(n)$ and on a set of surrogate time series $\mathbf{y}^{(l)}(n) = \begin{bmatrix} y_1^{(l)}(n) & \cdots & y_N^{(l)}(n) \end{bmatrix}^T$, $l = 1, \ldots, M$. Each time series

$\mathbf{y}^{(l)}(n)$ is computed specifically for the causal coupling under investigation, such that there is no direct causal coupling from $y_j^{(l)}(n)$ to $y_i^{(l)}(n)$. A statistical test is then applied to compare the values of the integrated PDC for the original series and for the set of surrogate series. The integrated PDC calculated from the original time series is assumed to be significant if its value lies above the 95th percentile of the distribution of corresponding values obtained from the surrogate data sets.

### 2.5 Statistical analysis

The correlation between different parameters is calculated using the Pearson correlation coefficient $r$ and related $p$-value. A $p$-value $< 0.05$ is considered statistically significant. All parameters are given in mean $\pm$ standard deviation.

## 3 Database

### 3.1 Simulations

In order to evaluate the impact of the different estimation methods for the MVAR coefficients on the PDC, a number of simulations based on the following MVAR simulation model with $N$ observations were carried out. First, a propagation pattern was imposed by defining an $N \times N$ binary connectivity matrix $\mathbf{C}$ such that $C_{ij} = 1$ if propagation from recording site $j$ to $i$ was allowed, and $C_{ij} = 0$ otherwise. The diagonal of $\mathbf{C}$ was set to one. Second, each direct coupling from recording site $j$ to $i$ was assigned a probability [16]

$$P_{ij} = \exp\left(-\frac{d_{ij}^2}{\lambda^2}\right), \tag{19}$$

i.e., the probability of a direct coupling was modeled to decrease with increasing distance $d_{ij}$ between the recording sites, where the decrease is controlled by the choice of $\lambda$. Thus, direct coupling from recording site $j$ to $i$ was present when the following conditions were both fulfilled,

$$C_{ij} = 1 \tag{20}$$

$$\delta_{ij} \geq 1 - P_{ij}, \tag{21}$$

where $\delta_{ij}$ was a uniformly distributed random variable, $\mathcal{U}(0, 1)$. Finally, the MVAR coefficients corresponding to the present direct couplings were determined, using different techniques for MVAR coefficients $a_{ij}(k)$ for which $i = j$ and $i \neq j$, respectively. The MVAR coefficients $a_{ij}(k)$, $i = j$, were determined

such that the resulting MVAR process had a narrowband characteristic similar to the preprocessed AF signals. Assuming an even-valued model order $m$, the poles $p_k^{(i)}$, $k = 1, \ldots, m$, of the univariate processes

$$x_i(n) = \sum_{k=1}^{m} a_{ii}(k) x_i(n-k) + w_i(n) \quad i = 1, \ldots, N \tag{22}$$

were placed in complex conjugated pairs

$$p_{l/2l}^{(i)} = \frac{\tilde{r}_0}{l} e^{\pm \iota l \tilde{\phi}_0} \quad l = 1, \ldots, m/2, \tag{23}$$

where the radius $\tilde{r}_0$ and the angle $\tilde{\phi}_0$ were chosen from $\mathcal{U}(0.5, 0.6)$ and $\mathcal{U}(0.9\phi_0, 1.1\phi_0)$, respectively. For odd-valued model orders, an additional real pole $p_m^{(i)} \sim \mathcal{U}(0.1, 0.3)$ was added. The remaining MVAR coefficients $a_{ij}(k)$, $i \neq j$, were sampled from a normal distribution, $\mathcal{N}(0, 0.5)$. Stability of the resulting MVAR model was ensured by evaluating the eigenvalues of the equivalent MVAR model of order one,

$$\mathbf{A}^{(1)} = \begin{bmatrix} \mathbf{A}_1 & \mathbf{A}_2 & \cdots & \mathbf{A}_{m-1} & \mathbf{A}_m \\ \mathbf{I} & \mathbf{0} & \cdots & \mathbf{0} & \mathbf{0} \\ \mathbf{0} & \mathbf{I} & \cdots & \mathbf{0} & \mathbf{0} \\ \vdots & & \ddots & & \vdots \\ \mathbf{0} & \mathbf{0} & \cdots & \mathbf{I} & \mathbf{0} \end{bmatrix}. \tag{24}$$

i.e., the procedure was repeated until a stable MVAR model was found.

The simulation model was then implemented for the geometry of a sphere, which was chosen in order to avoid boundary conditions. On the sphere, $N = 16$ recording sites were distributed along four lines of longitude, A to D, situated at 0°, 90°, 180°, and 270°, respectively. Four evenly spaced bipolar electrodes were placed at each longitude and denoted A1 to A4, ..., D1 to D4. In the following, these recording sites are indexed by $i = 1, \ldots, 16$. The distances between the recording sites were determined to

$$d_{ij} = \arccos\left( \frac{\mathbf{q}_i \cdot \mathbf{q}_j}{||\mathbf{q}_i||\,||\mathbf{q}_j||} \right) r_s, \tag{25}$$

where $\mathbf{q}_i = \begin{bmatrix} q_{ix} & q_{iy} & q_{iz} \end{bmatrix}^T$ is the position of the $i$-th recording site in Cartesian coordinates, and $r_s$ is the radius of the sphere which was set to 1.

The simulated propagation on the sphere was defined through the connectivity matrix such that it had its origin at recording site A3, see Fig. 1(a). A more unorganized region of propagation was defined at recording sites C1, C2,

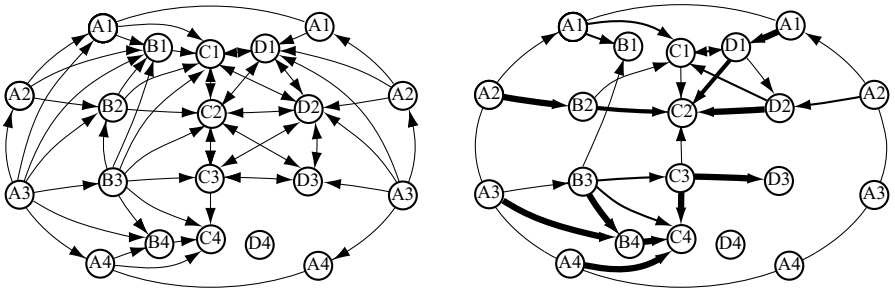


**Figure 1:** Projection of the sphere employed in the simulations together with the positions of the recording sites and a directed graph illustrating (a) the propagation pattern as imposed by the binary connectivity matrix $\mathbf{C}$, and (b) the direct couplings present in the simulations, with the width of each arrow proportional to the size of the corresponding $\Pi_{ij}^2$.

C3, D1, D2, and D3, while D4 was left isolated. Applying the second condition in Eq. (21) for the presence of a direct coupling, together with $\lambda = 1.5$, resulted in that 42 out of the $N^2 = 256$ possible direct couplings were non-zero, see Fig. 1(b). The corresponding MVAR coefficients were then sampled for model order $m = 3$ and $\phi_0 = \pi/4$, for which a stable MVAR model usually was found immediately. Furthermore, employing $\mathbf{\Sigma}_w = \mathbf{I}_{N\times N}$, the non-zero integrated PDCs $\Pi_{ij}^2$, which in the simulations were calculated by integrating $\pi_{ij}(f)$ over the entire frequency range, yielded $0.38 \pm 0.29$.

The performance of the different estimation methods for the MVAR coefficients is evaluated with respect to two aspects, the first being related to the detection of the present direct couplings. For that purpose, the following two hypothesis are defined,

$$\mathcal{H}_0 : a_{ij}(k) = 0 \qquad k = 1, \ldots, m \tag{26}$$

$$\mathcal{H}_1 : a_{ij}(k) \neq 0 \qquad \text{for at least one } k, \tag{27}$$

where $\mathcal{H}_0$ and $\mathcal{H}_1$ correspond to the absence and the presence of direct coupling from recording site $j$ to $i$, respectively. The probability of false alarm is then estimated by

$$P_{FA} = \frac{N_{FP}}{N_{FP} + N_{TN}}, \tag{28}$$

where $N_{FP}$ is the number of false positive (FP) direct couplings, i.e., $\mathcal{H}_1$ is decided though $\mathcal{H}_0$ is true, and $N_{TN}$ is the number of true negative (TN)

direct couplings, i.e., $\mathcal{H}_0$ is decided and true. Similarly, the probability of detection is estimated by

$$P_D = \frac{N_{TP}}{N_{TP} + N_{FN}}, \tag{29}$$

where $N_{TP}$ is the number of true positive (TP) direct couplings, i.e., $\mathcal{H}_1$ is decided and true, and $N_{FN}$ is the number of false negative (FN) direct couplings, i.e., $\mathcal{H}_0$ is decided though $\mathcal{H}_1$ is true.

The second aspect is related to the estimation accuracy of the MVAR coefficients and its impact on derived measures. This aspect is evaluated employing the normalized error function

$$\varepsilon(\mathbf{M}) = \frac{||\mathbf{M} - \hat{\mathbf{M}}||^2}{||\mathbf{M}||^2}, \tag{30}$$

which can be interpreted such that the error associated with the estimated matrix $\hat{\mathbf{M}}$ is determined as a fraction of the norm of the corresponding known matrix $\mathbf{M}$. It is employed for both the MVAR coefficients, i.e., $\mathbf{M} = \mathbf{B}$, and the integrated PDC, i.e., $\mathbf{M} = \mathbf{\Pi}^2$, where

$$\mathbf{\Pi}^2 = \begin{bmatrix} \Pi_{11}^2 & \cdots & \Pi_{1N}^2 \\ \vdots & \ddots & \vdots \\ \Pi_{N1}^2 & \cdots & \Pi_{NN}^2 \end{bmatrix}. \tag{31}$$

For the integrated PDC, the estimation accuracy is also evaluated separately for TP and FP direct couplings through employing the matrices $\mathbf{\Pi}_{TP}^2$ and $\mathbf{\Pi}_{FP}^2$, which consist of those elements of $\mathbf{\Pi}^2$ which correspond to TP and FP direct couplings, respectively, and zeros otherwise.

In case the investigated property is a function of frequency, i.e., $\mathbf{M}(f)$, the mean of $\varepsilon(\mathbf{M}(f))$ over all frequencies $f$ is used instead and denoted by $\varepsilon_f(\mathbf{M})$. This measure is used for frequency representation of the MVAR model, i.e., $\mathbf{M}(f) = \bar{\mathbf{A}}(f)$, as well as the PDC, i.e., $\mathbf{M}(f) = \boldsymbol{\pi}^2(f)$, where

$$\boldsymbol{\pi}^2(f) = \begin{bmatrix} |\pi_{11}(f)|^2 & \cdots & |\pi_{1N}(f)|^2 \\ \vdots & \ddots & \vdots \\ |\pi_{N1}(f)|^2 & \cdots & |\pi_{NN}(f)|^2 \end{bmatrix}. \tag{32}$$

## 3.2 AF Recordings

The method is illustrated on a recording from a patient with paroxysmal AF who underwent an electrophysiological study with a multielectrode basket catheter (Constellation catheter, EP Technologies, Boston Scientific) in the

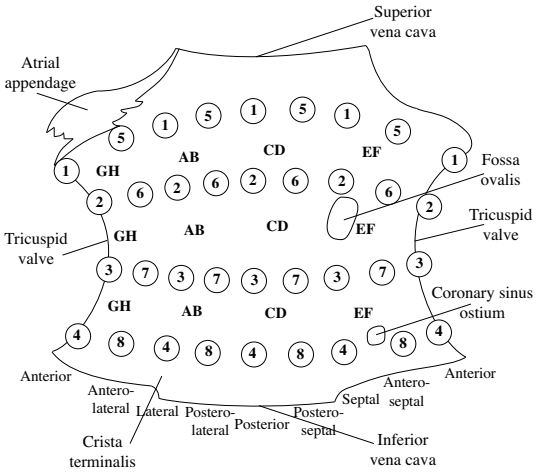


**Figure 2:** Schematic representation of the open RA with the position of the bipolar recording sites on the intracardiac wall. The eight splines of the basket catheter were positioned on the anterior, lateral, posterior, and septal walls, as well as on intermediate positions.

right atrium (RA). The basket catheter had a diameter of 31 mm and consisted of eight splines, A to H, each carrying eight evenly spaced electrodes (4 mm inter-electrode distance). Thirty-two bipolar intracardiac electrograms were acquired by coupling adjacent pairs of electrodes (CardioLab System, 30–500 Hz [Prucka Engineering, Inc.]). In this patient, five electrograms had to be excluded because of poor signal-to-noise ratio. The sampling rate was 1 kHz, and two 5-s segments were chosen for analysis.

A schematic representation of the recording sites is shown in Fig. 2. To approximate the distance between the recording sites, Eq. (25) was employed with $r_s$ set to half the diameter of the basket catheter, i.e., 15.5 mm. It was further assumed that the splines were approximately situated at the longitudes at $0°$, $45°$, $\ldots$, $315°$.

Prior to MVAR analysis, the electrograms were preprocessed with bandpass filtering (finite impulse response (FIR), 40–250 Hz, order 40, Kaiser window), rectification, and lowpass filtering (FIR, 0–20 Hz, order 40, Kaiser window) [17]. After filtering, the sampling rate was decimated to 100 Hz.

# 4 Results

Based on the MVAR simulation model described in Sec. 3.1, $N_{sim} = 20$ simulations were carried out for sample sizes $T = 5mN$, $3mN$, and $2mN$. For the simulations, model order $m = 3$ was employed for estimation, while for the AF recordings, the optimal model order was searched for in the range 1 to 15. The number of surrogate time series for the AF recordings was $M = 100$, and the results were obtained for $f_\Delta$ set to 0.5 Hz, cf. Eq. (17).

## 4.1 Simulations

In LS estimation, none of the MVAR coefficients are estimated to exactly zero, and thus all direct couplings exist. Consequently, both $P_{FA}$ and $P_D$ always yield 1 in LS estimation, see Table 1. In the adaptive group LASSO, $P_{FA}$ increases with decreasing sample size from 0.01±0.01 to 0.12±0.03, while there is a smaller change in $P_D$, i.e., from 1±0 to 0.99±0.01. For the distance-adaptive group LASSO, similar values are obtained for $P_D$ as for the adaptive group LASSO. However, in terms of $P_{FA}$ the distance-adaptive group LASSO yields better results than the adaptive group LASSO especially for smaller sample sizes.

**Table 1:** Simulation performance of LS estimation, adaptive group LASSO, and distance-adaptive group LASSO in terms of $P_{FA}$ and $P_D$.

| | LS | | Adaptive group LASSO | | Distance-adaptive group LASSO | |
|---|---|---|---|---|---|---|
| T | $P_{FA}$ | $P_D$ | $P_{FA}$ | $P_D$ | $P_{FA}$ | $P_D$ |
| $5mN$ | 1±0 | 1±0 | 0.01±0.01 | 1±0 | 0.01±0.01 | 1±0 |
| $3mN$ | 1±0 | 1±0 | 0.04±0.02 | 1±0.01 | 0.04±0.01 | 1±0.01 |
| $2mN$ | 1±0 | 1±0 | 0.12±0.03 | 0.99±0.01 | 0.09±0.02 | 0.99±0.01 |

The normalized error functions for $\mathbf{B}$, $\bar{\mathbf{A}}(f)$, $\boldsymbol{\pi}^2(f)$, and $\boldsymbol{\Pi}^2$ are displayed in Fig. 3(a) to (d). The results are consistent in the sense that adaptive and distance-adaptive group LASSO perform much better in estimating the MVAR model as well as the PDC than does LS estimation for all three sample sizes $T$. While the adaptive and distance-adaptive group LASSO perform rather similar for larger sample sizes, i.e., $T = 5mN$ and $T = 3mN$, knowledge about the distance between the recording sites further improves the estimation for $T = 2mN$. The same trends can be seen in the normalized error functions for $\boldsymbol{\Pi}^2_{FP}$ and $\boldsymbol{\Pi}^2_{TP}$, which are displayed in Fig. 3(e) and (f), respectively.

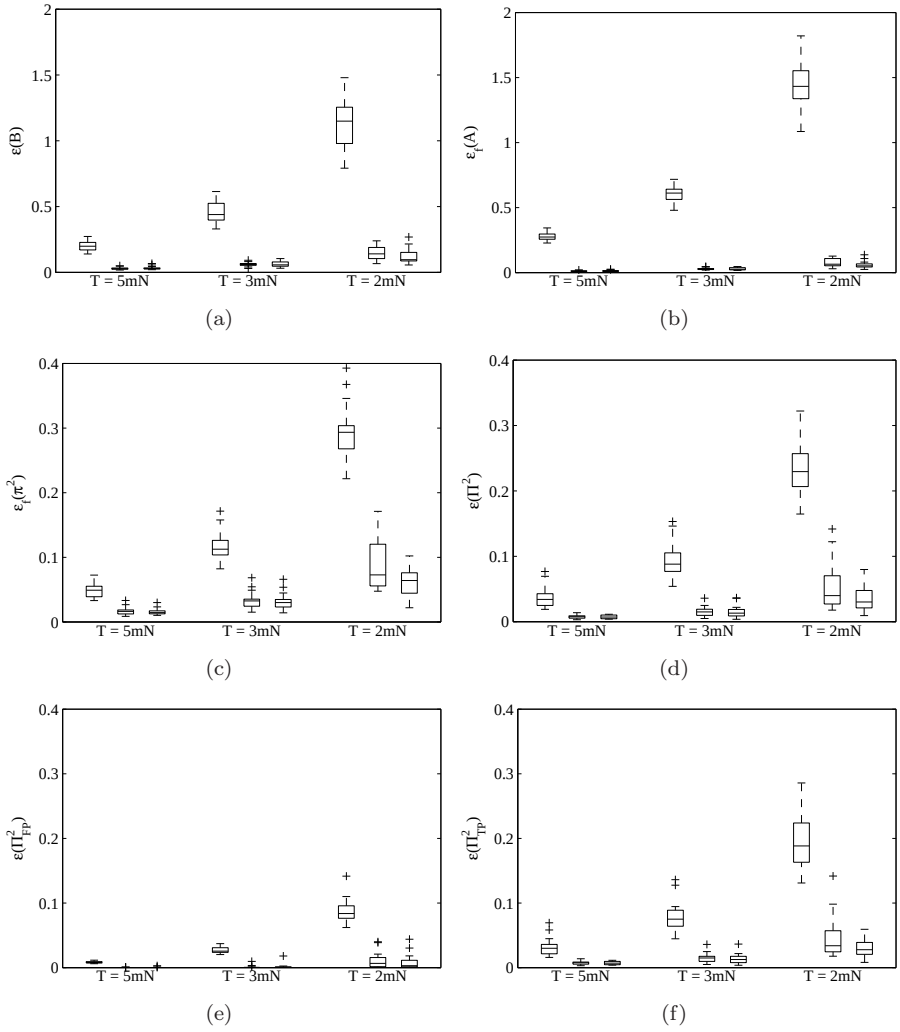


**Figure 3:** The normalized error function for (a) $\mathbf{B}$, (b) $\bar{\mathbf{A}}(f)$, (c) $\boldsymbol{\pi}^2(f)$, (d) $\boldsymbol{\Pi}^2$, (e) $\boldsymbol{\Pi}^2_{FP}$, and (f) $\boldsymbol{\Pi}^2_{TP}$ for different sample sizes $T$. The performance measures are for each $T$ presented in groups with the order LS estimation, adaptive group LASSO, and distance-adaptive group LASSO. The lines of the boxes correspond to (from top to bottom) the upper quartile, the median, and the lower quartile.

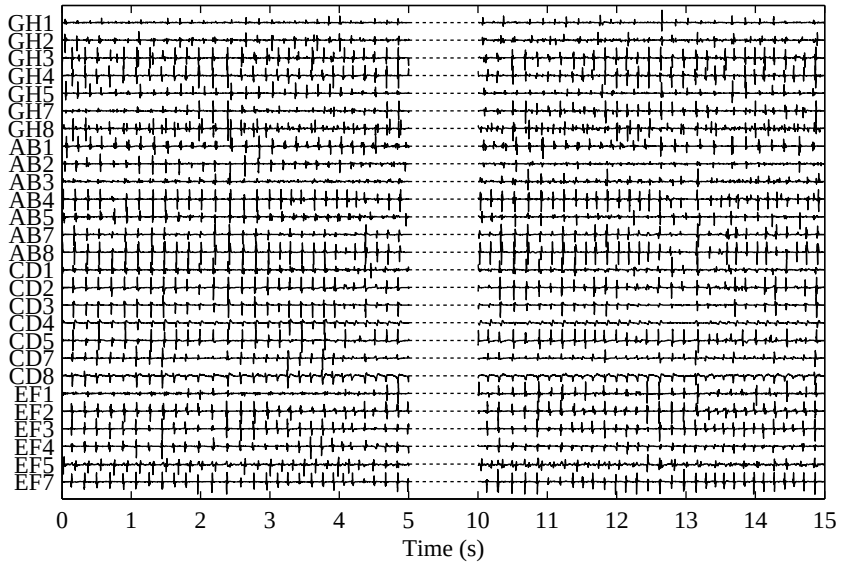


**Figure 4:** The original electrograms of an AF recording during two 5-s segments, which are separated by 5 s.

## 4.2 AF Recordings

MVAR analysis was performed on all 27 available electrograms for two 5-s segments, see Fig. 4. The estimated model order was consistently $m = 4$. For the first time segment, the percentage of possible directed couplings between different recordings sites which are found to be significant decreases slightly from 8.6% in LS estimation to 8% and 7.7% for adaptive and distance-adaptive group LASSO, respectively. The corresponding $\Pi_{ij}^2$ range from 0.05 to 0.41 (0.11±0.06) in LS estimation, from 0.001 to 0.52 (0.12±0.11) in adaptive group LASSO, and from 0.0004 to 0.53 (0.15±0.13) in distance-adaptive group LASSO. Similar results are obtained for the second time segment, where the percentage of possible directed couplings between different recordings sites decreases from 10% to 8.4% and 8.1%, and the corresponding $\Pi_{ij}^2$ range from 0.04 to 0.35 (0.11±0.07), from 0.004 to 0.69 (0.12±0.15), and from 0.001 to 0.71 (0.12±0.17) in LS estimation, adaptive group LASSO, and distance-adaptive group LASSO, respectively.

The propagation patterns obtained from MVAR coefficients estimated with LS estimation as well as adaptive and distance-adaptive LASSO are illustrated for both time segments in the directed graphs in Fig. 5. For the first time

segment, the propagation pattern derived from LS estimation is rather difficult to interpret, see Fig. 5(a). A large number of directed couplings can be seen to originate in the low septal RA at recording site EF3, and a transverse propagation from the septal towards both the anterior and posterior and from there further to the lateral RA is indicated. A clearer manifestation of this propagation pattern is provided by the directed graphs derived with adaptive and distance-adaptive group LASSO, see Figs. 5(c) and (e), respectively. Both directed graphs suggest a propagation originating from the low septal RA close by recording sites EF3 and EF4. From there, the electrical activity propagates caudocranially in the septal RA as well as transversely towards the anterior and posterior RA. In the posterior/postero-lateral wall, craniocaudal propagation is indicated, and finally, the propagation spreads towards the lateral RA from both anterior and postero-lateral regions. For the second time segment, interpretation of the propagation pattern is again difficult for the directed graph derived from LS estimation, see Fig. 5(b). This is in contrast to the sparse directed graphs derived from adaptive and distance-adaptive group LASSO, see Fig. 5(d) and (f), respectively, which evidence a propagation similar to the one during the first time segment. In addition, in the upper RA, a transverse propagation spreading from the posterior wall is indicated.

# 5 Discussion

Successful estimation of the MVAR coefficients is crucial for successful estimation of the PDC, since the calculation of the PDC is entirely derived from the model coefficients. In order to avoid overfitting of the MVAR model and to incorporate prior information such as sparsity of the solution, the adaptive group LASSO is proposed. The adaptive group LASSO improves the estimation of the MVAR coefficients by putting a constraint on the LS solution which is defined as an intermediate between the $L_1$ and $L_2$ norm. While the $L_2$ norm is responsible for avoiding overfitting, which is in similarity to, e.g., ridge regression, the singularities caused by the $L_1$ norm are achieving the sparsity. As a consequence of the sparse solution, the complexity of the estimation problem is reduced by the lower number of parameters to be estimated.

The sparsity of the resulting solution can for the analysis of intracardiac AF recordings be motivated by the observation that direct couplings over longer distances are likely to be zero. This information has been further incorporated in the definition of the weights $\alpha_l$ in the distance-adaptive group LASSO. An understanding of how the $\alpha_l$ affect the solution of the LARS algorithm may be achieved by considering Eq. (10), which defines the correlation between the $l$-th group of input variables and the current residual. As the correlation is

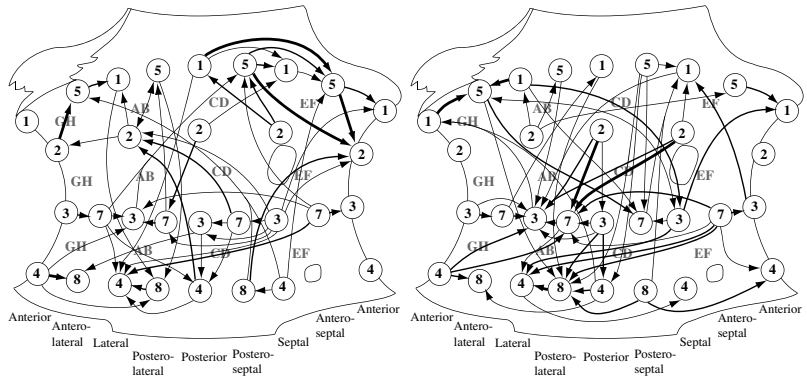
GH
AB
CD
EF
Anterior
Antero-lateral
Lateral
Postero-lateral
Posterior
Postero-septal
Septal
Antero-septal

(a) (b)

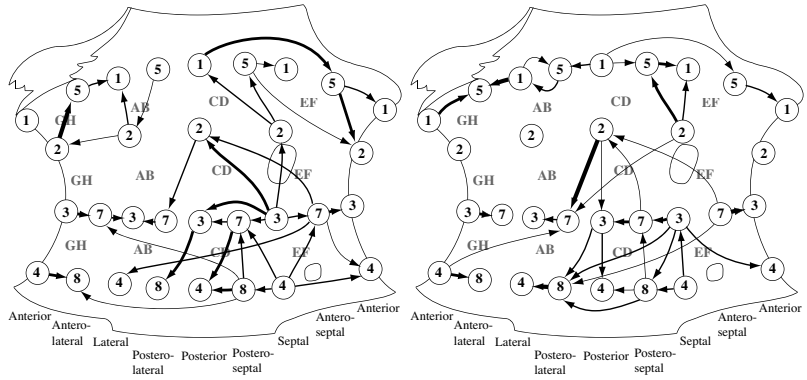
GH
AB
CD
EF
Anterior
Antero-lateral
Lateral
Postero-lateral
Posterior
Postero-septal
Septal
Antero-septal

(c) (d)

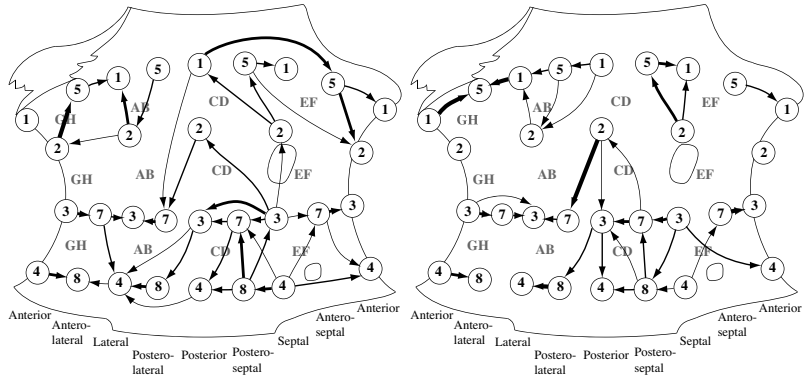
GH
AB
CD
EF
Anterior
Antero-lateral
Lateral
Postero-lateral
Posterior
Postero-septal
Septal
Antero-septal

(e) (f)

weighted with $\alpha_l^{-2}$, the weights can affect the order in which the groups of input variables become active such that groups with a small or large $\alpha_l$ will presumably be added in an earlier or a later iteration step, respectively. Thus, if the coupling can be assumed to decrease with distance, as is the case during AF, $\alpha_l$ should be chosen to increase with distance instead.

The Gaussian kernel function employed in Eq. (9) is one out of many possibilities to calculate the weighting factors from the distance [18]. In that paper, an algorithm for geographically weighted LASSO is presented. The formulation of the problem is such that each input variable, e.g., some demographic statistics, is collected at different locations. Weighted LS or weighted LASSO can then be employed for local linear regression, i.e., the samples of each input variable are weighted according to their location. In the present paper, however, each input variable is collected at different time instants. Local linear regression could thus be employed for calculating the propagation pattern close to a certain time instant, avoiding the need to explicitly restrict the samples of the input variables to some time window. Each input variable is also associated with a certain location, i.e., recording site. Because of the formulation of the problem, the distances between these locations can, however, not easily be incorporated into local linear regression algorithms. Instead, linear regression with constraints depending on the distances, such as the proposed distance-adaptive group LASSO, should be employed.

Previously, other LASSO variants such as the ordinary LASSO and group LASSO have been employed for MVAR estimation, e.g., when analyzing the functional connectivity between different brain areas [16, 19] or within gene networks [20]. In those studies, the main interest was the detection of directed information flow based on tests applied directly to the MVAR coefficients. In the present work, the accuracy of the estimated MVAR coefficients is also of interest, as they are further used in the calculation of the PDC. Employing a number of simulations, for which the true MVAR model was known, the adaptive and distance-adaptive group LASSO were found to lead to major improvements in both detection and estimation accuracy when compared to LS estimation. While these accuracies were rather similar for adaptive and

**Figure 5** ***(preceding page)*****:** Directed graphs illustrating the propagation pattern during two 5-s segments of an AF recording based on (a),(b) LS estimation, (c),(d) adaptive group LASSO, and (e),(f) distance-adaptive group LASSO. In order to simplify the interpretation, the directed graphs are restricted to significant $\Pi_{ij}^2 \geq 0.05$. The width of each arrow is proportional to the size of the corresponding $\Pi_{ij}^2$.

distance-adaptive group LASSO when more samples were analyzed, improvements could be observed with the distance-adaptive group LASSO for smaller sample sizes. This indicates that additional prior information on the underlying topology can, to some extent, compensate for the decrease in performance which otherwise comes with decreasing sample size.

The estimation accuracy for the integrated PDCs was also evaluated separately for FP and TP direct couplings, see Fig. 3(e) and (f), respectively. The purpose with this distinction is to point out the potential, but also the limitations, of significance testing, which may be seen as a possibility to imply sparse coupling subsequent to the computation of the PDC. In detail, significance testing is potentially able to reduce errors in those integrated PDCs which are associated with FP direct couplings, as non-significant integrated PDCs can be put to zero. However, significance testing is not able to positively affect errors associated with TP direct couplings. This is a consequence of that in contrast to the integrated PDC, MVAR coefficients corresponding to non-significant direct couplings cannot directly be put to zero, as this could lead to substantial changes in the characteristics of the MVAR model. As these MVAR coefficients enter the calculation of the PDC through the normalization, they can affect the outcome of the analysis even though they are not directly associated with the direct coupling under evaluation. Thus, the importance to actively encourage sparsity already during the estimation of the MVAR model is further underlined.

The method has been evaluated on two 5-s segments of a recording during paroxysmal AF in the RA. During AF, both the amount and the strength of direct couplings are expected to decrease with increasing distance. However, for LS estimation, a large number of significant direct couplings were present also over longer distances, leading to difficulties in the identification of the propagation pattern from the corresponding directed graphs. The interpretation of the directed graphs, and thus the identification of the propagation pattern, was substantially simplified by the sparsity achieved with adaptive group LASSO. Compared to LS estimation, the directed graphs became sparse mostly with respect to direct couplings over longer distances, which is interesting as the adaptive group LASSO does not make use of the distances between the recording sites. When employing these distances in the distance-adaptive group LASSO, a further increase in sparsity among the direct couplings over long distances could be observed. Thus, similar to the simulations, the largest improvement was achieved by employing a sparse estimation method instead of LS estimation. However, when the distance between the recording sites is known or can be estimated, further improvements in the estimation of the propagation pattern are possible.

During both 5-s segments, a propagation starting in the low septal RA

was evidenced, suggesting atrial impulses entering the RA from the left atrium (LA) at the coronary sinus ostium. This RA breakthrough site as well as the subsequent propagation pattern agrees with clinical observations [21–23]. More specifically, a RA breakthrough close to the coronary sinus ostium, usually superior or posterior to the orifice as also observed in the present example, has been associated to AF originating in the inferior LA or the inferior pulmonary vein [21]. In a previous study, the analysis of a similar example, though based on LS estimation, suggested a propagation pattern with a breakthrough site in the high septal RA, typically associated to the presence of a focal source in the right upper pulmonary veins [7]. These examples highlight the potential of the PDC as a method for extracting information on the propagation patterns during AF, which in the future may contribute to a better understanding of AF mechanisms as well as an improvement of AF treatment, e.g., during ablations.

# 6 Conclusions

In the present paper, the estimation of propagation patterns in intracardiac AF signals in terms of the PDC has been shown to be substantially improved when prior information on sparsity as well as the distances between the recording sites are incorporated in the underlying model. The method may serve as a support for the electrophysiologist especially when a manual evaluation of the recorded signals becomes difficult, e.g., due to the large amount of recorded signals or the signal organization.

# References

[1] K. Nademanee, J. McKenzie, E. Kosar, M. Schwab, B. Sunsaneewitayakul, T. Vasavakul, C. Khunnawat, and T. Ngarmukos, "A new approach for catheter ablation of atrial fibrillation: mapping of the electrophysiologic substrate," *J. Am. Coll. Cardiol.*, vol. 43, pp. 2044–53, 2004.

[2] P. Sanders, O. Berenfeld, M. Hocini, P. Jaïs, R. Vaidyanathan, L.-F. Hsu, S. Garrigue, Y. Takahashi, M. Rotter, F. Sacher, C. Scavée, R. Ploutz-Snyder, J. Jalife, and M. Haïssaguerre, "Spectral analysis identifies sites of high-frequency activity maintaining atrial fibrillation in humans," *Circulation*, vol. 112, pp. 789–797, 2005.

[3] H. Oral, A. Chugh, E. Good, S. Sankaran, S. S. Reich, P. Igic, D. Elmouchi, D. Tschopp, T. Crawford, S. Dey, A. Wimmer, K. Lemola, K. Jongnarangsin, F. Bogun, F. Pelosi, and F. Morady, "A tailored approach to

catheter ablation of paroxysmal atrial fibrillation," *Circulation*, vol. 113, pp. 1824–31, 2006.

[4] U. Richter, A. Bollmann, D. Husser, and M. Stridh, "Right atrial organization and wavefront analysis in atrial fibrillation," *Med. Biol. Eng. Comp.*, vol. 47, pp. 1237–46, 2009.

[5] M. Masè, M. Del Greco, M. Marini, and F. Ravelli, "Velocity field analysis of activation maps in atrial fibrillation a simulation study," in *IFMBE Proc.*, vol. 25, pp. 1014–17, Springer Berlin Heidelberg, 2009.

[6] F. Weber, G. Seemann, and O. Dössel, "Wave direction and conduction velocity analysis from intracardiac electrograms – a single-shot technique," *IEEE Trans. Biomed. Eng.*, vol. 57, pp. 2394–2401, 2010.

[7] U. Richter, L. Faes, A. Cristoforetti, M. Masè, F. Ravelli, M. Stridh, and L. Sörnmo, "A novel approach to propagation pattern analysis in intracardiac atrial fibrillation signals," *Ann. Biomed. Eng.*, 2010 (in press).

[8] L. A. Baccalá and K. Sameshima, "Partial directed coherence: a new concept in neural structure determination," *Biol. Cybern.*, vol. 84, pp. 463–474, 2001.

[9] L. A. Baccalá, K. Sameshima, and D. Y. Takahashi, "Generalized partial directed coherence," in *Proc. 15th Intern. Conf. on Digital Signal Processing*, pp. 162–166, IEEE Press, 2007.

[10] R. Tibshirani, "Regression shrinkage and selection via the lasso," *J. Roy. Statist. Soc. Ser. B*, vol. 58, pp. 267–288, 1996.

[11] H. Wang and C. Leng, "A note on adaptive group lasso," *Comp. Stat. Data Analysis*, vol. 52, pp. 5277–86, 2008.

[12] H. Lütkepohl, *New Introduction to Multiple Time Series Analysis*. Springer-Verlag Berlin Heidelberg, 2005.

[13] M. Yuan and Y. Lin, "Model selection and estimation in regression with grouped variables," *J. Roy. Statist. Soc. Ser. B*, vol. 68, pp. 49–67, 2006.

[14] G. Schwarz, "Estimating the dimension of a model," *Ann. Stat.*, vol. 6, pp. 461–464, 1978.

[15] C. Wilke, L. Ding, and B. He, "Estimation of time-varying connectivity patterns through the use of an adaptive directed transfer function," *IEEE Trans. Biomed. Eng.*, vol. 55, pp. 2557–64, 2008.

[16] P. A. Valdés-Sosa, J. M. Sánchez-Bornot, A. Lage-Castellanos, M. Vega-Hernández, J. Bosch-Bayard, L. Melie-García, and E. Canales-Rodríguez, "Estimating brain functional connectivity with sparse multivariate autoregression," *Phil. Trans. Roy. Soc. Lond. B Biol. Sci.*, vol. 360, pp. 969–981, 2005.

[17] D. Botteron and J. Smith, "A technique for measurement of the extent of spatial organization of atrial activation during atrial fibrillation in the intact human heart," *IEEE Trans. Biomed. Eng.*, vol. 42, pp. 579–586, 1995.

[18] D. C. Wheeler, "Simultaneous coefficient penalization and model selection in geographically weighted regression: the geographically weighted lasso," *Environ. Plann. A*, vol. 41, pp. 722–742, 2009.

[19] S. Haufe, R. Tomioka, G. Nolte, K.-R. Müller, and M. Kawanabe, "Modeling sparse connectivity between underlying brain sources for EEG/MEG," *IEEE Trans. Biomed. Eng.*, vol. 57, pp. 1954–63, 2010.

[20] A. Fujita, J. R. Sato, H. M. Garay-Malpartida, R. Yamaguchi, S. Miyano, M. Sogayar, and C. E. Ferreira, "Modeling gene expression regulatory networks with the sparse vector autoregressive model," *BMC Systems Biology*, vol. 1, doi 10.1186/1752–0509–1–39, 2007.

[21] S. Saksena, N. D. Skadsberg, H. B. Rao, and A. Filipecki, "Biatrial and three-dimensional mapping of spontaneous atrial arrhythmias in patients with refractory atrial fibrillation," *J. Cardiovasc. Electrophysiol.*, vol. 16, pp. 494–504, 2005.

[22] B. Zrenner, G. Ndrepepa, M. R. Karch, M. A. Schneider, J. Schreieck, A. Schömig, and C. Schmitt, "Electrophysiologic characteristics of paroxysmal and chronic atrial fibrillation in human right atrium," *J. Am. Coll. Cardiol.*, vol. 38, pp. 1143–49, 2001.

[23] F. Gaita, L. Calò, R. Riccardi, L. Garberoglio, M. Scaglione, G. Licciardello, L. Coda, P. D. Donna, M. Bocchiardo, D. Caponi, R. Antolini, F. Orzan, and G. Trevi, "Different patterns of atrial activation in idiopathic atrial fibrillation: simultaneous multisite atrial mapping in patients with paroxysmal and chronic atrial fibrillation," *J. Am. Coll. Cardiol.*, vol. 37, pp. 534–541, 2001.